Dynamic Modelling of a Rolling Piston Compressor

including a packed-bed drying system

Sri Kavya Movva

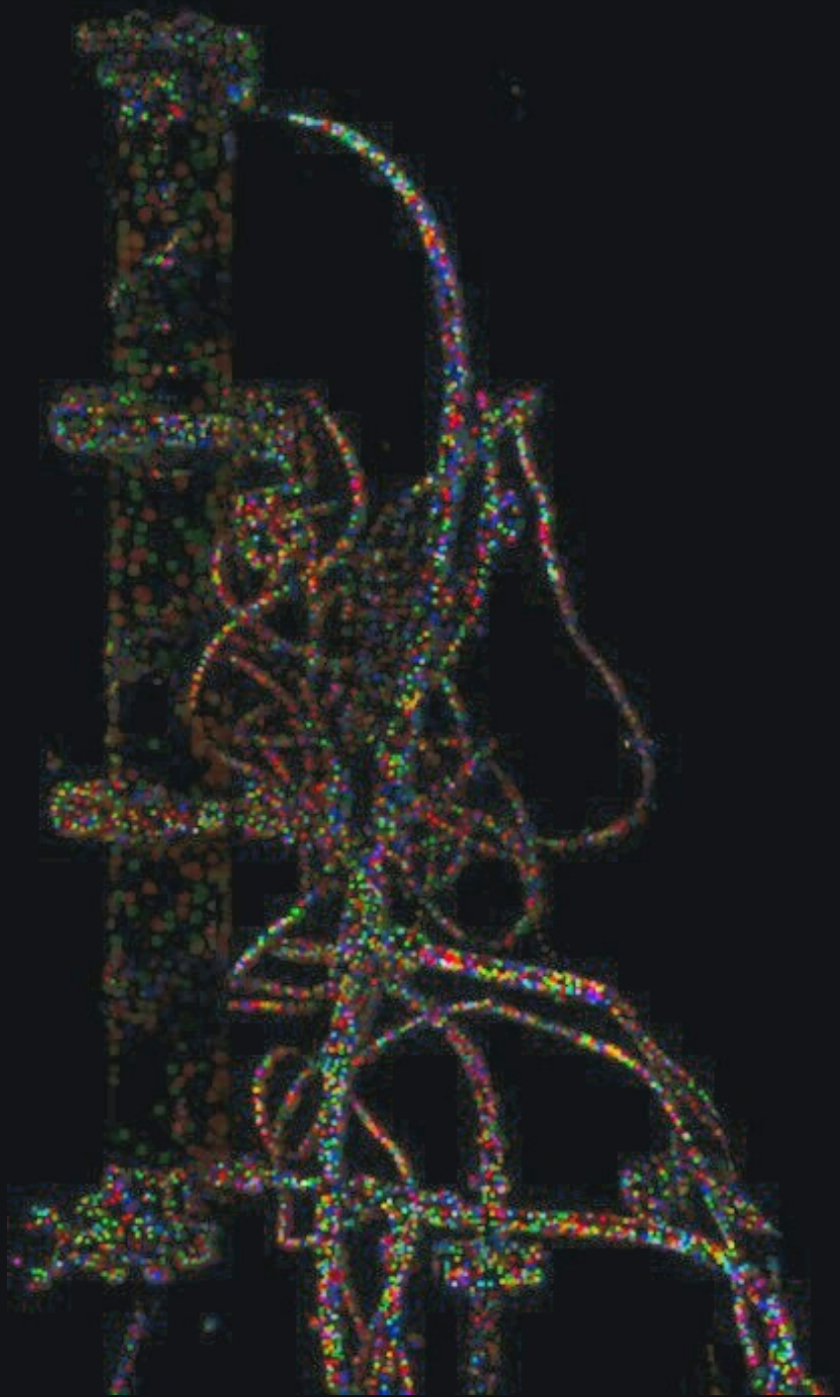

TU Delft

Dynamic modelling of a rolling piston compressor

including a packed-bed drying system

by

Sri Kavya Mowa

To obtain the degree of Master of Science
at the Delft University of Technology,
to be defended publicly on Tuesday July 12, 2022 at 12:00 PM.

Student number: 5100968

Thesis committee:	Prof. dr. ir. W. de Jong	TU Delft, Supervisor and Chairman
	Ir. J. van Kranendonk	ZEF.B.V., Daily Supervisor
	Ir. M. Ramdin	TU Delft
	Prof. dr. ir. E. Goetheer	TU Delft

TU Delft

“We adore chaos because we love to produce order.”

M.C.Escher

Cover Design:‘Generative Art of the Drying System Setup and A Typical Run’ by P.Werblicka, with the help of CHROMATA.

Summary

To produce an alternative fuel like Methanol from scratch, on a miniature scale- the reactants (CO_2 and H_2O) are sourced locally. Zero Emission Fuels B.V. (ZEF) does this by collecting carbon dioxide from air via carbon capture techniques and compressing to a high pressure of 55bars. As a consequence of humidity inside the captured CO_2, condensation is observed which is detrimental to the life of the compressor. To avoid this, a packed-bed drying system is designed as an auxiliary to the rolling piston compressor. This study aims to understand and model these two systems and subsequently integrate them to examine the effects of their dynamic operation. The purpose of this model is to provide a design tool, with the ability to predict the reaction of the system when sized differently, in various environments.

At first, the physics and governing principles of the two subsystems are studied and a layered modelling approach was devised. The systems was modelled individually and then integrated using Simulink- a tool that allows this layering up of the models. To build a dynamic model of such a setup, a characteristic time scale analysis was performed to identify the relevant phenomena inside each subsystem. Significant internal factors to be modelled were variations in relative humidity and temperature caused by the drying system, the changes in thermo-physical properties of the gas due to a change in temperature and the pressure fluctuations caused by the compressor. The external factors to be modelled were the changes in ambient temperature over operation time, caused by a variation in solar irradiation. The main finding was that the compressor's characteristic time scale (300s) was considerably smaller than that of the drying system (4-8hours/day). This meant an almost instantaneous operation of the compressor, rendering it uninteresting in the dynamic model of the integrated system.

A mechanistic dynamic model of the drying system, based on literature, was made with inherent controls to flip it between adsorption and desorption modes. It is responsive to the changes in the ambient, and allows optimisation by changing the duty cycles of energy inputs. The model was then validated using experimental data from two working prototypes at ZEF. Some heat and mass transfer properties were then fitted to conform to these setups. A methodology to obtain these parameters while sizing a new design is discussed. The key performance indicators, which are cycle time and cycle capacity are given by the model and are crucial in deciding the energy consumption of the system.

On the other hand, an empirical model is built to replicate the rolling-piston compressor. The compressor is treated like a grey-box and is described by a polytropic coefficient. A novel approach to create a compressor map for a positive displacement compressor, that is not mass-produced, is chosen. This compressor map is then used to predict the mass flow and output temperature of the system. Since the compressor map is empirical, the model was also validated using data from literature.

Finally, the drying system and the compressor were integrated in the model and experiment by means of a capillary tube. A model was made for this as well to obtain the 'interacting parameters'- which were the mass-flow into the compressor, mass-flow out of the capillary tube and the temperature and pressure of this re-loop flow. The effects of integration and the consequences to other systems upstream and downstream of this setup were scrutinised.

To conclude, a validated model is built to size new iterations of the setup. Multiple cycle models of a packed bed drying system and compressor maps of positive displacement compressors- that are not found commonly in literature, are explored in this study and recommendations to further develop them are given towards the end.

Acknowledgements

As I approach the end of this project which also marks the end of my colourful life as a student at TU Delft, I would like to extend my deepest appreciation to all the people who have made this possible.

Firstly, I would like to thank the team at Zero Emission Fuels for giving me this opportunity and nurturing me through this exciting endeavour. The completion of this thesis would not have been possible without the constant guidance of Jan van Kranendonk- his colossal knowledge of all things within and beyond ZEF's horizon and his work ethic were an inspiration. Thank you for all the numerous debugging sessions and modelling philosophies that remain my main take-home message. The impact of unwavering support by Ulrich Starke and his weekly feedback meetings cannot be overestimated. Many thanks to you for creating a positive working environment and being an incredible mentor. I would also like to thank Mrigank Sinha and Paul Vroegindeweij for always making the time when I had questions. Credits to the entire Fluid Machinery team- especially Chris, Yoran, Jorden and Zarif not only for their contributions to the innovations at ZEF, but also for the endless brainstorming sessions that led to the fruition of this work. It was a pleasure working with you.

The veritable experience of Professor Wiebren de Jong has been invaluable to me during the course of my thesis. Your keen eye and remarkable perspective pushed me to delve further in and clarified the standards of scientific work. Thank you for your patience and crucial feedback during pivotal periods of this project. I am also grateful to my committee for taking out some of their valuable time to evaluate my work.

I am extremely indebted to my family for shaping me as a person and being my pillars of strength. To mom and dad, thank you for your altruistic love and providing me with everything I ever needed. To my sister Sahitya, for being instrumental in my path towards science and for proof-reading my drafts, albeit at ungodly hours.

I cannot leave TU Delft without mentioning all my friends who have been constant bearers of joy in these past years and have kept me sane in this otherwise solitary journey. Particularly- Jason, Nikita, Paula and Marleen for their continuous encouragement and companionship. I will cherish our faculty-hopping thesis days and hope we continue our adventures for the years to come! Special thanks to Vinamrata, Kajal and Koushal for extending their moral support from across the world and for their patience through thick and thin.

Finally, I would like to thank you, my reader, for picking this up. I hope you find my work helpful and wish you a pleasant reading!

-Kavya Movva, July 2022.

Contents

List of Figures

List of Tables

1 Context

In this chapter, the motivation behind this project and what Zero Emission Fuels is discussed. An overview of the entire process and a basis of design are elaborated.

1.1. Methanol Economy

With the ever increasing urgency of the climate crisis, there is an inevitable need to transition to a carbon less world. To aid this transition, there is a hike in the number of new initiatives- especially concerning the fuels that have been consumed on a daily basis for decades. The widely used carbon rich fuels like gasoline and diesel have been the cause of increase in greenhouse gas emissions by a landslide of 78% from 1970-2010 and contribute almost 65% to the entire greenhouse gas emissions in 2010 [10]. This number is only observed to increase in the past decade [11]. To dwindle this trend, a shift towards alternative fuels has emerged. Methanol, being the world's most commonly shipped chemical, with more than 95 billion liters produced each year, has gained popularity for being one of the substitutes [12]. The key advantage of moving towards a methanol economy is that there is an existing infrastructure (combustion engines, power blocks, fuel cells) that can easily be adapted to using methanol. Based on how it is produced, methanol has the highest potential of carbon emission reduction (65-95%) when compared to other alternatives [13]. **This is the main driver behind the startup company Zero Emission Fuels (hereby called ZEF) which produces green or renewable methanol using an ultra-low carbon intensive process.**

1.2. Process Miniaturisation

To manufacture a 'green' chemical, the choice of process plays an important role in determining its footprint. Process intensification focuses on engineering developments that lead to a substantially smaller, cleaner, safer and more energy efficient technology [14]. Current trends in process intensification lean to miniaturisation as one of their central principles [15]. Using miniaturisation also helps drastically reduce costs and time required for development- by getting rid of uncertainties related to the scaling from laboratory to production level[1]. Keeping the urgency of climate action in mind, **ZEF has adopted a down-sized approach to their methanol production process.** On the other hand, designing a modular micro-scale plant gives the flexibility to accommodate most commercial demands by simply numbering up the modules. Moreover, using a modular philosophy gives more control over the entire process, making it inherently safer. ZEF's business model assumes economies of scale, where mass production of the modules would reduce production costs. This is not the most conventional approach in process industries, but is commonly practiced by electronics and automotive sectors. Recapitulating, ZEF designs a solar PV powered modular micro plant that produces methanol. In order to make methanol in the greenest way, ZEF's plant is built to:

- Be powered by solar energy and be deployed in solar power abundant locations- like the Sahara

[1] However, this results in a rise of uncertainties caused by low mass-flow rates, which will be discussed in the following chapters.

- Obtain feedstock (CO_2 and H_2O) using direct air capture technology
- Produce the other ingredient, H_2, from water electrolysis, locally, cutting down on transportation footprint

1.3. Overview of the ZEF plant

The entire ZEF plant, shown in Figure 1.1, is divided into four subsystems on the basis of their functions. They are all powered by a solar panel and are briefly discussed in the following lines.

- **Methanol Synthesis (MS):** Here, the reaction takes place between gaseous CO_2 and H_2, in a 1:3 molar ratio, which gives the desired product methanol and water as a byproduct. The product is later distilled to obtain Methanol at 99.8% purity.
- **Fluid Machinery (FM):** The reaction in MS requires the CO_2 gas input at a high pressure of 55 bars at 366.7g/hour, with a quality 98% (by weight). In order to achieve this pressure, a compression system is required before the feed. To attain the quality of CO_2 and avoid condensation related problems inside the compressor and downstream processes, a drying system is present at the compressor inlet.
- **Direct Air Capture Unit (DAC):** To obtain one of the reactants, carbon dioxide, the direct air capture unit is used to harvest it from air and supply it to the FM system. It comprises two absorber and desorber columns that use TEPA as a solvent. The product feed consists of gas and liquid phase carbon dioxide and water- where the gaseous feed is sent to FM and the liquid feed to AEC.
- **Alkaline Electrolysis Cell (AEC):** To obtain the other reactant, hydrogen, an alkaline electrolysis cell is used to electrolyse liquid water into gaseous hydrogen and oxygen.

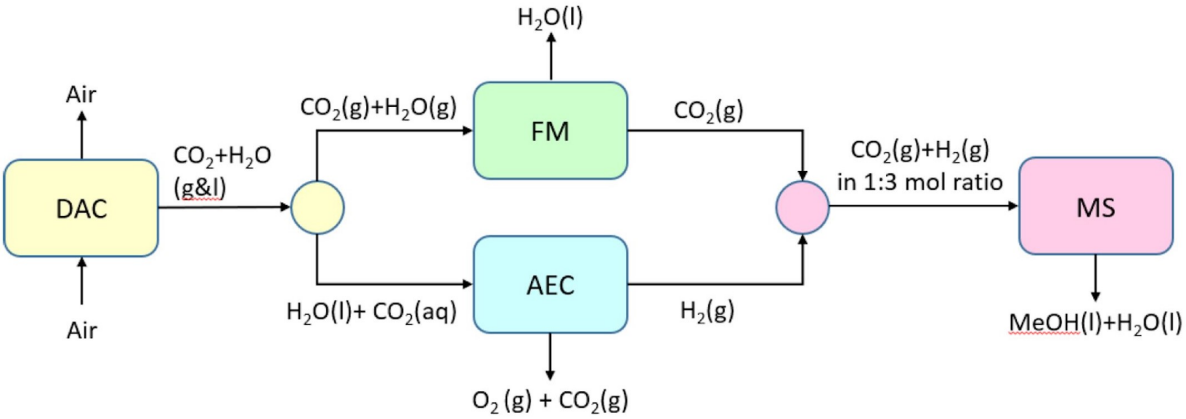

Figure 1.1: Process flow diagram of the ZEF plant reprinted from [1]

During the timeline of this project, ZEF deemed an optimal sizing for the plant to be '10x'- meaning that one module is powered by ten solar panels. For a 10x plant, the required methanol production for a day is 2kg/day. A basis of design can be derived from this output demand, using the stoichiometry of the methanol production reaction and is shown in Table 1.1. It shows that at the end of the FM subsystem, there is a production demand of 2750g/day for CO_2, which dictates a mass flow rate of 343.75 g/hour to the compressor, assuming eight hours of operation in a day.

To get a basic understanding of what happens inside the plant and to size it, taking the chemical properties of the fluids into account, a COCO[2] simulation is shown in Figure1.2. To simulate the plant, a flash tank with a heat-exchanger in front of it was used to mimic the Direct Air Capture unit flash tank, where CO_2 and H_2 are separated. The captured CO_2 then enters a compressor train to reach a pressure of 55 bars for the methanol synthesis reaction downstream. The compressor train comprises three

Table 1.1: Basis of Design of the ZEF plant using stoichiometry

	CO2	+	H2	→	CH3OH	+	H2O
Moles	1		3		1		1
Molar mass	44		2		32		18
Moles per day target (mol/day)	62.5		187.5		62.5		62.5
Mass Target (g/day)	2750		375		2000		1125

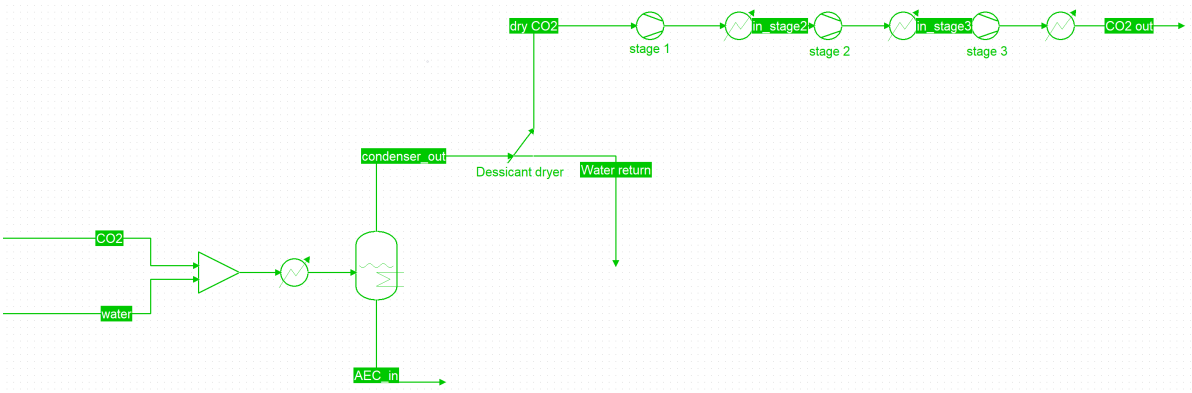

Figure 1.2: The COCO Model

stages of positive displacement compressors and this choice will be explained in Chapter 3. Carbon dioxide (0.75 mole fraction) and water (0.25 mole fraction) enter the AEC flash tank at atmospheric pressure (1bar). The flash tank separates the two compounds and proceeds into the compressor train. The compressor train is specified by a constant pressure ratio. The steam conditions are shown in Table 1.2, where stream 7 and stream 8 are before and after the heat exchanger in front of the AEC flash tank. The mass flow rates correspond to the values derived in Table 1.1.

Table 1.2: Basis of design using COCO Model

Stream	7	8	condensor_out	dry CO2	in_stage2	in_stage3	CO2 out	Unit
Pressure	1	1	1	1	3.91	15.29	59.78	bar
Temperature	40.21	50	50	50	50	50	50	°C
Flow Rate	766.06	766.06	359.67	343.79	343.79	343.79	343.79	g/h
Mole frac (CO2)	0,25	0.25	0.90	1	1	1	1	
Mole frac (H2O)	0.75	0.75	0.10	0	0	0	0	

1.4. Report Structure

In the following chapter, the goal, scope and research questions of this thesis are enlisted. In Chapter 3, the components used in the Fluid Machinery subsystem are analysed using existing literature. Further, the modifications done to adapt commercial components to ZEF requirements are discussed. In Chapter 4, the modelling approach is detailed and the relevant key performance indicators (KPIs) are identified. A characteristic time-scale analysis was then performed to identify the relevant phenomena to model dynamically, with the help of the literature. Following this methodology, the Chapters 5 and 6 discuss the model implementation, experimentation, their respective results and validation. System integration effects and the control strategy employed are also enclosed in these chapters. Towards the end, conclusions are summarised and recommendations for future work are given in Chapter 7.

[2]An open source process plant simulator

2

Scope

In this chapter, the scope and goals of this work will be discussed. Later, the research questions formulated are listed.

The scope of this thesis encompasses the integrated FM system which consists of the desiccant drying columns and compressor (train). Other subsystems that could fluctuate the process parameters of the scope are solar panel inputs, methanol synthesis production demands and the DAC output stream. These subsystems cannot be controlled directly by the FM system and are thus considered external.

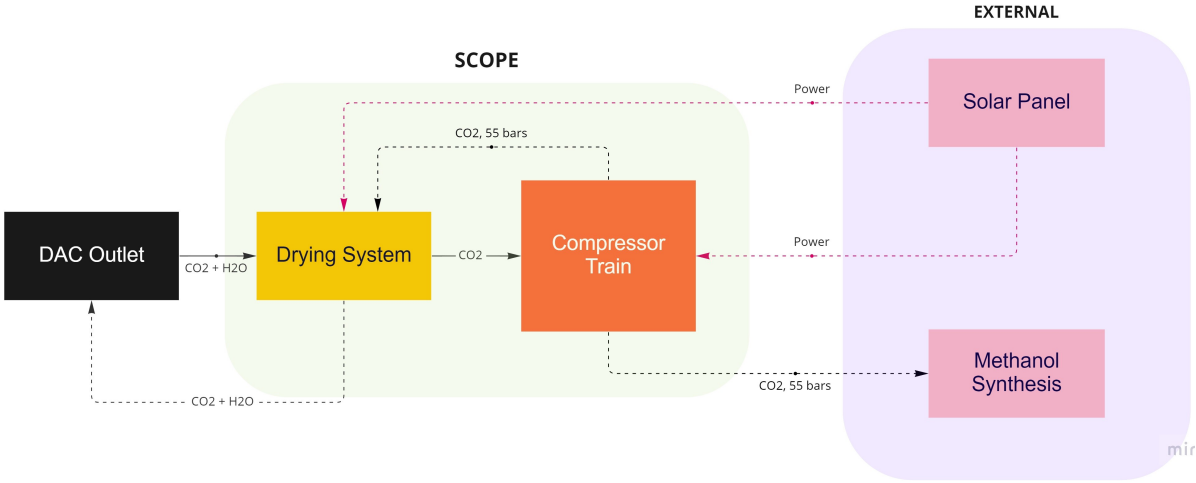

Figure 2.1: Scope of this thesis

2.1. Goal of this thesis

This work aims to provide a design and development tool in the form of a model that predicts the reaction of the aforementioned system in a dynamic environment.

2.2. Research Questions

- What are the process parameters that are relevant for dynamic operation of the compressor train?
- What are the external factors that affect dynamic operation of the system? (Eg: DAC output stream, Power Fluctuations, Ambient Temperature variations)
- What are the bottlenecks of the current compressor train, drying system and DAC buffer flash tank?

- What is the effect of fluctuations in the dynamic parameters (eg: mass flow) on the system performance?
- What are the implications of running a compressor including the drying system?
- Is it feasible to dynamically operate the system (for instance following the profile of the direct air capture system output)? If so, what is the control strategy and optimum operation envelope?

3

State of the art of Fluid Machinery at ZEF

In order to predict its behaviour, it is imperative to first gain a complete understanding of the system. This chapter investigates the fundamentals of each component of the FM system from existing literature inside and outside of ZEF. Moreover, it will discuss the following questions

- What is the goal of the FM system?
- What design choices are made and why?
- How do they work and how can they be modelled mathematically?
- What are their applications, shortcomings and research trends found from literature survey?
- What modifications are needed at ZEF to adapt them?

3.1. Goal of the FM System and its consequences

The goal of the FM system is to process the CO_2 to a 98% (weight)[1] purity and a 55bar pressure while meeting the ZEF production targets.

3.1.1. Compressor Selection due to Low Mass Flow Rates:

As derived from the basis of design in Section 1.3, ZEF's target mass flow rate of 343.75 g/hr (52cc/s) is a very meager amount in comparison to the specifications of compressors traditionally used in industry. This accompanies its own set of problems and design consequences. The sizing and volume of the compressor are drastically reduced, which affects its efficiencies and operation range. When the compressors are downsized, the surface area to volume ratio increases, resulting in higher friction losses (due to more contact of rotating parts). It could also imply higher leakages, hence a lower volumetric efficiency. As shown in Figure 3.1, a type of positive displacement type compressor chosen is the 'rolling piston compressor', for its high efficiency in the range of mass flow rates and rpm that the ZEF system dictates. Research on CO_2 compression by Collings et al. [16] shows that there is no type of compressor (amongst scroll, rolling piston and reciprocating) that offers best performance in all energy, leakages and torque aspects. However, according to a comparison study by Ozu and Itami [17],rolling piston compressors exhibit a higher overall performance due to high volumetric efficiencies despite having mechanical losses. These mechanical losses can be circumvented by having long interval for suction and discharge losses, thus reducing thermodynamic losses to valves. The rolling piston compressor is also a mature technology that is widely used in modern day air conditioning units.
Research at ZEF tackles with rolling piston compressors produced by Aspen LLC [18] and their Chinese reproduction, Purswave Compressors [19] with 1.4cc and 1.9cc displacements. They are currently the world's smallest refrigeration compressors. With a few modifications, they could be adapted to fit into the ZEF system, which will be explained in the coming sections.

[1] As condensation occurs at 50 bars, if the RH=2%.

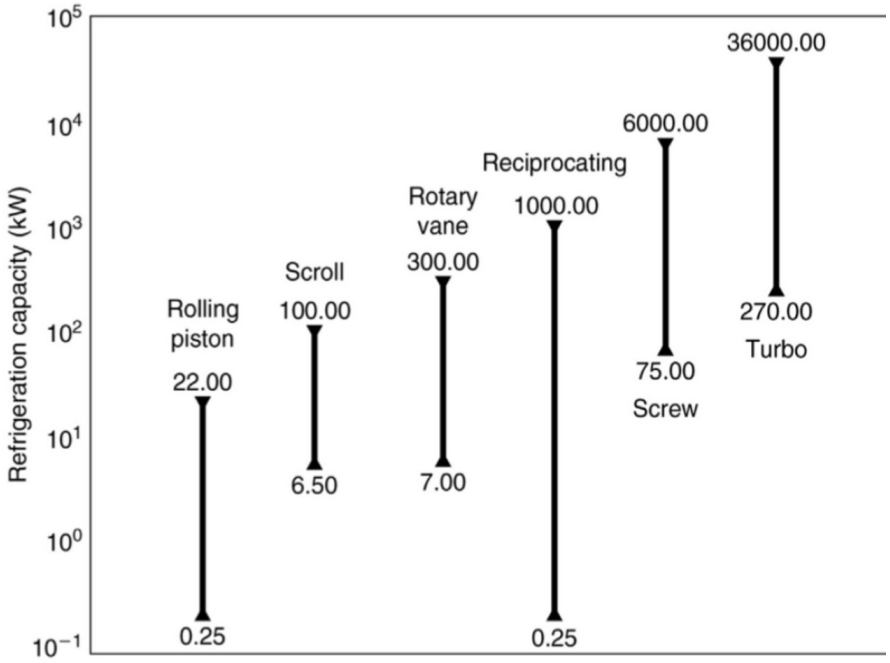

Figure 3.1: Compressor Capacities taken from [2]

3.1.2. Pressure Ratios

Another deciding operating condition is the output of the DAC stream, which flows into FM around 1bar. This implies a pressure ratio of 55, for one compressor in order to give the desired output of 55bars at the end. Assuming reversible adiabatic compression, the maximum temperature that the compressor can reach is determined[2]. the temperature at the outlet increases as an exponent of the pressure ratio, as shown in Equation 3.1. This means that for a high pressure ratio of 55 and heat capacity ratio (γ) of CO_2 being 1.3, the temperature and heat generated inside the compressor increases to 752K.

$$T_{\text{out}} = T_{\text{in}} \left(\frac{p_{\text{in}}}{p_{\text{out}}} \right)^{\frac{\gamma-1}{\gamma}} \tag{3.1}$$

This indicates that high pressure ratios demand very robust compressor components as they lead to severe temperature and mechanical stress problems [20]. In order to reduce the mechanical and thermodynamic losses that are consequences of a high pressure ratio, it was suggested to use a multi-stage compressor train comprising 2 or 3 stages. This selection is a design choice which is a result of work done by the author's predecessors in FM system- Bergstein [8] and de Koning [21], and is considered out of the scope of this thesis.

3.2. Operating Conditions of the compressor system

Assuming a 3 stage compressor train, an intake of CO_2 vapour at 1 bar and a target methanol production of 2kg/day, the operating conditions of a three stage compression system with a constant pressure ratio of 3.92 are:

3.3. Working principle of a rolling piston compressor

To evaluate the performance of the selected compressor type, its working principles and geometry must be understood. The rolling piston compressor, as shown in Figure 3.2, has three primary components- a stationary cylinder, a rolling piston (simply called a 'roller') and a vane that is attached to a spring. The crankshaft has the same center-line as the cylinder and has an eccentric shape. The roller is mounted on the eccentric cam inside the cylinder. The reciprocating vane is held in a slot shaped

[2] In an adiabatic process, all the heat is conserved.

Table 3.1: Operating conditions of the compressor train

Stage	P,in	P,out	V,in	V,out
#	[bar]	[bar]	[cc/s]	[cc/s]
1	1	3.92	52.9	18.3
2	3.92	15.4	18.3	6.4
3	15.4	60.2	6.4	2.2

chamber in the cylinder block. A lubricating oil is present between the vane, roller and cylinder which also acts as a gas-tight seal to prevent leakage losses. The vane and the roller in contact with the inner cylinder wall are positioned such that there are two separate chambers formed- a suction chamber and a compression chamber. As the shaft rotates, the roller orbits within the cylinder, changing the volumes of the chambers. The compression and suction of the fluid medium is a result of these volume changes. A single compressor cycle consists of a suction cycle and a compression cycle in two revolutions (from

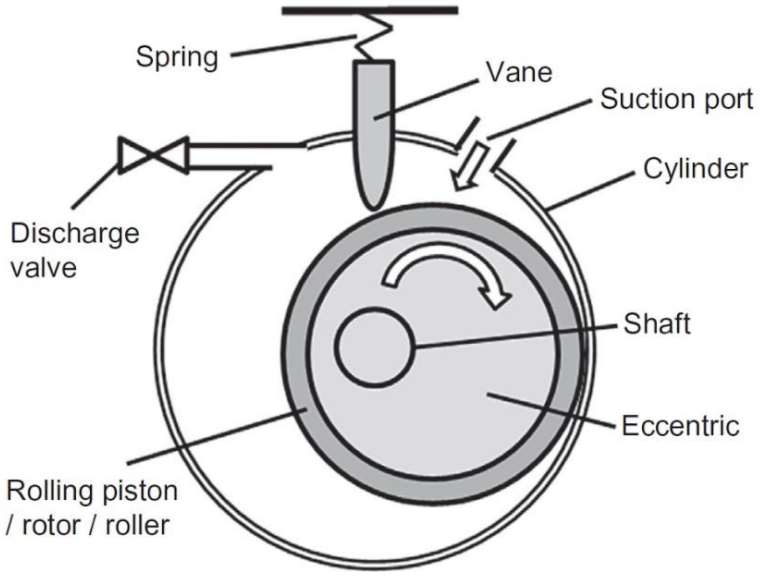

Figure 3.2: Schematic of a rolling piston compressor taken from [3]

0° to 360° and 360° to 720°).
Suction Cycle: The vane is compressed at the start due to lack of pressure difference inside and outside the cylinder. At the start of a revolution, the roller is turned counterclockwise and the vane expands. The suction chamber expands and low pressure fluid enters the chamber. The pressure remains fairly constant during this process. The roller continues to rotate until it reaches the vane again, completing the suction cycle. The maximum amount of fluid is taken inside the chamber, at the end of the suction cycle.
Compression Cycle: When the roller passes the suction port, the compression cycle begins. As it rotates, the volume of the compression chamber changes resulting in a rise of fluid pressure inside. Once the pressure inside the chamber is more than the pressure outside the discharge valve, the discharge pressure is reached. The valve then opens and gas is discharged. The pressure remains constant during the discharge process, except for an overshoot when the valve opens. The valve closes again when the pressure is no more higher than the outside pressure, starting another suction cycle. The cycle is illustrated in Figure 3.3, where position B is the start of the compression cycle and position A is the start of the suction cycle.

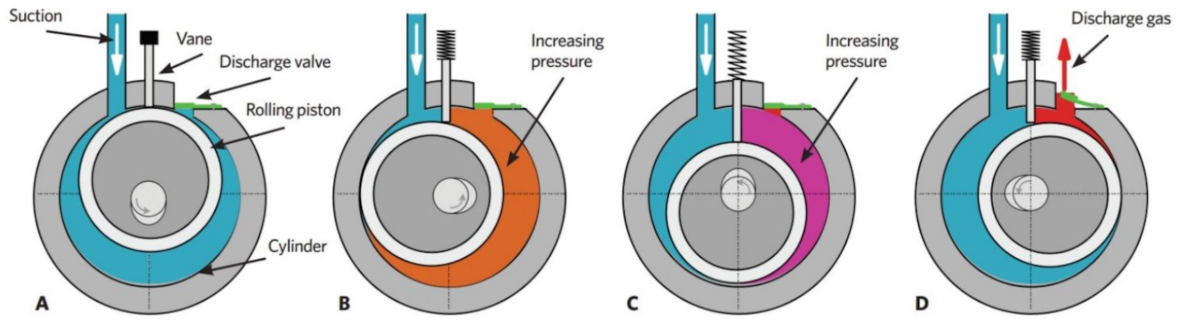

Figure 3.3: Compression cycle of a rolling piston compressor taken from [4]

3.4. Geometrical Relationships

As the chamber volume is a key parameter to be altered, its relationship to other major components needs to be studied. The main operating variables of a rolling piston compressor are:

1. rotor's angular position (θ from the center of the vane)
2. rotational speed (ω) and
3. vane tip contact angle (α)

The major design dimensions are:

1. vane thickness (tv)
2. radius of the cylinder (Rc)
3. radius of the rotor (Rr)
4. Ratio of the radii (Υ= Rr/Rc)
5. Chamber length (lc)
6. eccentric (Re) and
7. vane tip (Rv)

These parameters are illustrated in Figure 3.4. Neglecting the vane thickness, the relationships between the aforementioned parameters as stated by [3] and maximum swept volume and variation of chamber volume with respect to roller angular position are given by equations 3.2 and 3.3, respectively. Equation 3.4 can be included to account for vane geometry.

$$V_{\max} = \pi \left({R_c}^2 - R_r^2 \right) l_c \tag{3.2}$$

$$\begin{aligned} V_{\text{chamber}} = \frac{R_c^2 l_c}{2} \Bigg[\left(1 - \Upsilon^2\right) \theta - \frac{(1-\Upsilon)^2 \sin 2\theta}{2} - \Upsilon^2 \sin^{-1}((\Upsilon - 1)\sin\theta) \\ -\Upsilon(1-\Upsilon)\sin\theta \sqrt{1 - (\Upsilon - 1)^2 \sin^2\theta} \Bigg] \end{aligned} \tag{3.3}$$

$$V_{\text{vane}} = \frac{R_c l_c t_v}{2} \left[1 - (1-\Upsilon)\cos\theta - \sqrt{(1-\Upsilon)^2 \cos^2\theta + 2\Upsilon - 1} \right] \tag{3.4}$$

3.5. Thermodynamics

The governing equations that describe the thermodynamics of the rolling piston compressor are the energy and mass balances and the fluid's thermal properties.

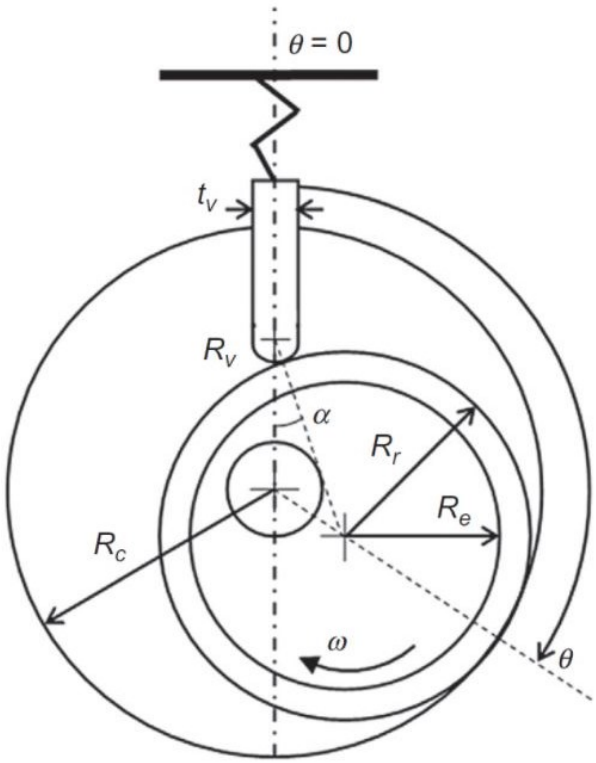

Figure 3.4: Major dimensions of a rolling piston compressor [3]

3.5.1. Energy Conservation

Applying the second law of thermodynamics and neglecting the potential and kinetic energies of the compressor components, we have:

$$m\frac{du}{dt} + u\frac{dm}{dt} = \frac{dQ}{dt} - \frac{dW}{dt} + \sum h_{in}\frac{dm_{in}}{dt} + \sum h_{\text{out}}\frac{dm_{\text{out}}}{dt} \tag{3.5}$$

where work done on the fluid during compression is given by: $(W = pdV)$

$$\frac{dW}{dt} = p\frac{dV}{dt} \tag{3.6}$$

Temperature variations can be observed in the fluid (due to thermodynamic processes) and in the components of the compressor (due to heat generation and friction losses). Therefore, there is heat transfer between:

1. components and the fluid
2. components
3. components and the atmosphere
4. lubricating oil and the components

The heat transfer between the fluid and the components is convective and can be neglected depending on the fluid's properties at high rotational speeds. In order to model the heat transfer in the compressor, the following assumptions can be made:

- Lumped capacitance: where different components of the compressor are considered as separate elements, heat transfer is modelled in each of them and then solved simultaneously.

- An ideal vapour compression cycle, (isentropic compression) is assumed. The deviation from real heat exchange can be calculated using isentropic efficiency. It is given by Equation 3.7 and is the ratio of ideal compression power to the real compression power, where the real power is given by Equation 3.8:

$$\varepsilon_{isen} = \frac{h_{\text{disc, isentropic}} - h_{\text{suct}}}{h_{\text{disc,real}} - h_{\text{suct}}} \tag{3.7}$$

$$P_{refr} = \dot{m}_{refr} \left(h_{\text{disc, real}} - h_{\text{suct}}\right) \tag{3.8}$$

3.5.2. Mass conservation

The change in mass of the fluid in the system is caused by suction and discharge and internal leakages. The flow through the suction and discharge ports can be modelled as a steady, 1-D adiabatic flow, given by Equation 3.10. Assuming that the suction port is always open, the discharge port has a non-return valve and the flow area of the valve opening is known at any point of time, the mass balance can be calculated using:

$$\frac{dm}{dt} = \sum \frac{dm_{in}}{dt} + \sum \frac{dm_{out}}{dt} \tag{3.9}$$

$$\frac{dm_{\text{fluid}}}{dt} = \rho_{2s} C_d A_2 \sqrt{2\,(h_1 - h_{2s})} \tag{3.10}$$

Where ρ is density, s is entropy, A_2 is the flow area and Cd is the coefficient of discharge which includes the non isentropic effects and flow losses.

3.6. Losses

To understand how the energy is dissipated in the system and ensure minimisation of losses during redesign, the losses need to be weighted. The various losses[3] in a rolling piston compressor are:

1. Motor loss: During the transmission of electrical energy to mechanical energy, the motor efficiency contributes to this loss.
2. Mechanical loss: The power transmitted from the motor to the shaft undergoes another loss due to the oil pumping losses, friction losses at bearings etc. The remaining power after this loss is called ‘indicated power’.
3. Discharge passage and suction passage losses: When the fluid enters and leaves the chamber through the suction port and discharge valve, it experiences some resistance from the passage, which results in these losses. Deducting these from the indicated power, the remaining power transmitted is known as the ‘effective power’.
4. Clearance volume loss: This is caused due to re-expansion of high pressure fluid in the clearance volume.
5. Heat loss during suction and compression: During the start of compression, when the pressure and temperature are still relatively low, there could be heat loss from the cylinder walls to the fluid, oil and fluid leakage from the discharge side. These losses are accounted for in compression losses. Similar losses during the suction cycle are accounted for in suction losses. The power remaining after these losses are regarded is called the ‘theoretical power’.

Although leakages are a cause for losses, especially in a compressor that is of ZEF’s scale, they are also important to reduce the frictional losses of rubbing parts. Therefore, a compromise must be made while designing the compressor, to optimise the leakages. Leakages are consequential to the design, as they reduce the mass flow rate, which is already a critical parameter in this system. In practice, it is hard to differentiate and quantify the effects of losses caused by internal leakages and heat transfer losses. However, studying the geometry and working of the compressor, the possible leakage paths and their effects can be determined as follows:

1. Gaps at the sides of the vane- effects are negligible, as they remain in contact during operation.

[3]More details about the calculation of each of these loss paths are given in Appendix **??**

2. Gap between the vane tip and rotor- effects are negligible, as they remain in contact during operation

3. Gap between the vane and cylinder end faces - can be modelled as flow from a convergent divergent nozzle as the flow goes from a high-pressure reservoir (compression chamber) to a low pressure reservoir (suction chamber) through a narrow channel where one of the walls (vane) is moving.

4. Gap between rotor and cylinder end faces - modelled as radially divergent pressure-driven flow from a source. Fluid has to be modelled as a mixture of the refrigerant and oil vapour and is non negligible.

5. Radial clearance gap between rotor and inner cylinder wall- modelled as a flow of pure refrigerant through a convergent-divergent nozzle.

According to research by Wakabayashi et al [22], the motor losses constituted almost half of the total losses followed by the heat transfer and leakage related losses which in combination contributed to 20% of the total losses. However, this research was done on a 550W hermetic compressor, and the effects of leakages and heat transfer losses on the volumetric efficiency of the compressor might be higher for a smaller scale compressor (<120W) that ZEF intends to use. This hypothesis is validated in research by [23] where the volumetric efficiency and isentropic efficiency of rolling piston compressors were studied and found to decrease drastically with their refrigeration capacities. Figure 3.5 shows the variation of efficiencies with the refrigeration capacity and when extrapolated to 550W, the difference in efficiency could be much higher.

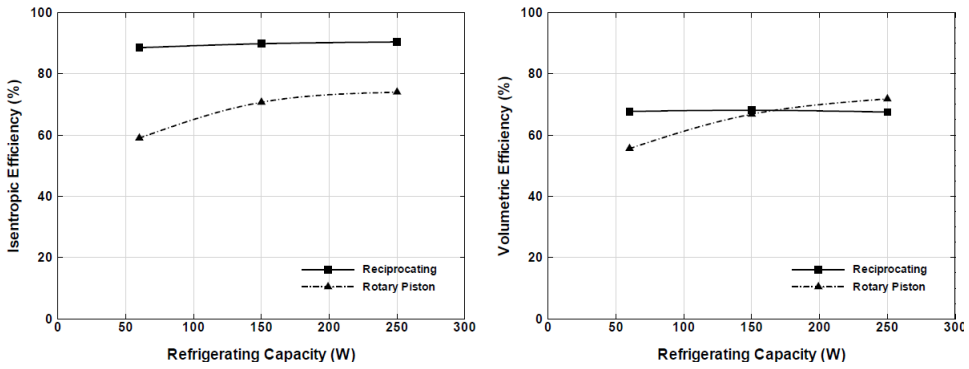

Figure 3.5: Variation in isentropic and volumetric efficiencies with refrigeration capacity

3.7. Modifications

3.7.1. Compressor Volume

As rolling piston compressors are typically used in the refrigeration industry, the dimensions and mass flow rates of an average unit are higher than ZEF requires. The Aspen compressors have a very low displacement volume (1.4-1.9 cc), which meets the constraints of the low mass flow rates. However, as explained in Section 3.1 to attain the pressure ratio, multiple stages of the compressor must be used. This would imply a lower volumetric flow rate at the end of the first stage for a given mass flow rate. Therefore the compressors would still need to be modified for a lower displacement volume. In order to keep the research costs low, the inexpensive counterparts of Aspen, Purswave compressors were disassembled and partly redesigned to be used for higher stages.

Modified compressor components:

While redesigning, the hermetic Purswave compressors were altered to modular compressors to continuously reassemble, repair and reiterate the designs allowing for an increased flexibility in research. The new modular housing, shown in Figure 3.6, is made up of a top lid and a bottom lid, the motor housing (with an O-ring) and the chamber housing.

After the work of Bergstein [8], the determined method of reducing the displacement volume was reducing the size of the excenter of the shaft and increasing the size of the roller by increasing the roller

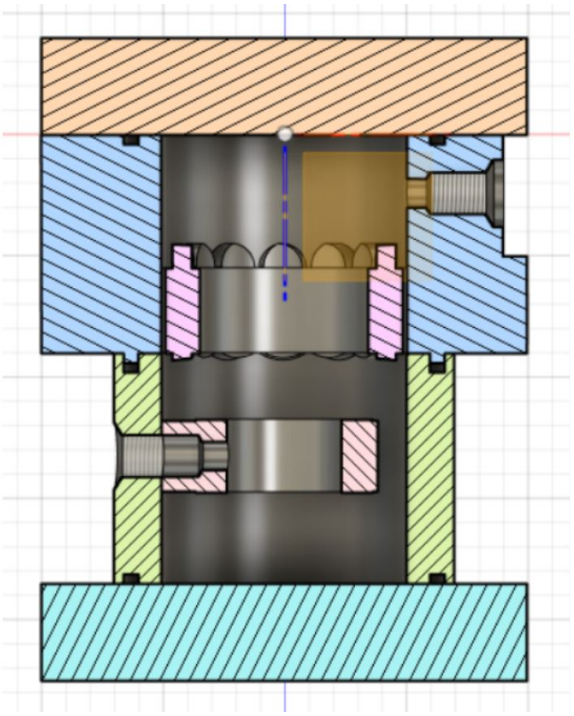

Figure 3.6: Schematic of modular ZEF Compressors. Orange- Top lid, Blue- motor casing, Pink- motor coil, Green- chamber casing, Light Red- Compression chamber, Cyan- Bottom lid.

outer diameter but decreasing the inner diameter. This method was chosen over downsizing the cylinder height in order to control leakages in the newly manufactured housing and for better alignment of components. The motor used in the compressor was taken from the disassembled Purswave compressor. It was concluded that a compressor train of Aspen compressors for the first stage and the modular compressors for higher stages would be used to achieve a pressure of 55 bars at the end.
The latest version of modular compressors (shown in Figure 3.7), whose design is still in progress, contains a single chamber for the motor and compressor, eliminating the requirement for an O-ring in the middle. The motor housing has a larger inner diameter, as the new motor used is taken from the Aspen compressor, due to better performance. Consequently, dimensions of the excenter and roller had to be changed.

3.7.2. Working Fluid Consequences

Another notable difference between mass produced rolling piston compressors and ZEF compressors is the working fluid. In a standard refrigeration compressor, the working fluid is a pure refrigerant. In ZEF's ideal case scenario, the working fluid would also be a pure refrigerant, Carbon dioxide. However, in reality, the output stream of DAC has some amount of water vapour in it. This has dire consequences on the lifetime of the compressor oil and in turn the lifetime of the compressor itself. The prescribed oil for Aspen compressors is Emakarate RL68H[4], a hygroscopic high-viscosity lubricant, intended to be used for pure refrigerants. Due to the presence of water vapour in the working fluid, the highly hygroscopic oil formed a mixture during operation which condensed inside the compressor. This was detrimental for the lifetime of the oil. It would also imply higher operating costs as the option of oil reloop would be impractical after the condensation. Therefore, the oil needs to be replaced with another hydrophobic oil, the principal constraint being the viscosity of the oil. This is because the oil needs to be viscous enough to perform as an appropriate seal between the working surfaces and ensure zero contact. The new choice, a result of Verhagen's work [24], was a hydraulic oil, Pelrus H 32[5], which met the high viscosity and hydroscopic constraints. As it is a hydraulic oil, it is also better suited for higher pressures and is corrosion resistant. However, the need for a dryer refrigerant still prevails.

[4] ISO VG 68 Synthetic polyol ester (POE) lubricant.
[5] ISO 11158 HV solvent-refined oil.

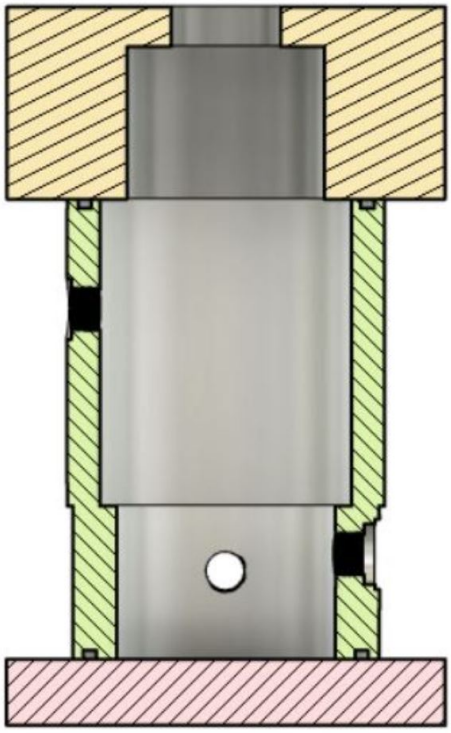

Figure 3.7: Latest version of the modular compressors, reprinted from [5]

3.8. Drying system:

In order to conform to the working fluid properties of the ZEF system without making further mechanical modifications to the compressor, an auxiliary system to dry the incoming fluid was developed by den Haan, a former thesis student at ZEF. The system was made of two desiccant-based packed bed drying columns, which would work in tandem by switching among absorption, regeneration and desorption cycles continuously to give 98% (by weight) CO_2 at the end. The output quality is dictated by the Methanol Synthesis subsystem of ZEF.
The selected desiccant was porous silica gel beads, as they perform consistently at ambient humidities and other desiccants like zeolite are more selective to CO_2. A temperature swing adsorption (TSA) process is chosen to regenerate the desiccant- where the silica gel's ability to retain moisture diminishes with rising temperatures.

3.8.1. Operation:

The following steps are involved in the operation of an integrated drying system concept and are illustrated in Figure 3.8:

1. The DAC output stream (wet gas at 1 bar) passes through the adsorption column.
2. Silica gel bed keeps drying the gas until it is saturated.
3. Dried gas is passed on to the compressor.
4. After the first column is saturated, it is heated to regenerate the silica gel and bring it to desorption temperature.
5. Compressed dry gas is passed on from the compressor to the desorbing column, via a capillary tube.
6. This re-loop of hot, dry gas flushes the water out of the packed bed until the silica gel beads are free of water.
7. During regeneration, the second column acts as an adsorption column.

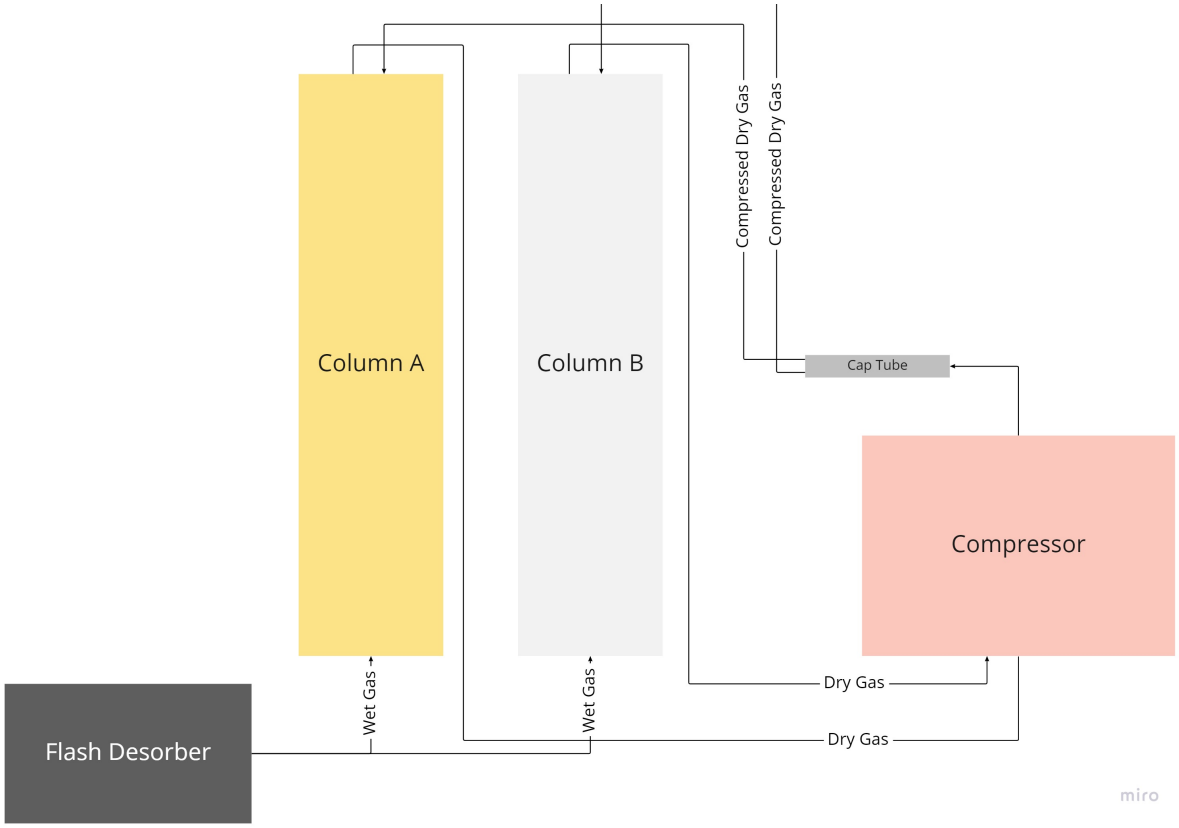

Figure 3.8: Schematic of the Drying System

8. After the first column is regenerated, it switches to adsorption mode and the second column switches to regeneration/ desorption mode.

Taking a deeper look into the columns, it is important to note that the adsorption of water by silica gel beads is an exothermic process and the desorption of the same is an endothermic process. However, the desiccant beads need to be at a higher temperature than ambient to start desorbing water and thus regenerate the column. The result of this is that the dominant energy cost in the drying process would be the regeneration step. This also brings out an important conclusion that the heat generated inside the adsorption column should never lead to attaining desorption-activation temperature. It would be counterproductive as condensation would then start to occur. Moreover, as the wet gas enters the column, the silica gel beads at the first site of contact (at the bottom of the column) dry the gas and pass on dry gas along the length of the column i.e, upwards. For this reason, it can be expected that the beads at the bottom get saturated earlier than the beads above them and so on. During this process of stripping, the temperature at that local site increases until the beads are saturated. Saturated beads do not generate any further heat of adsorption.

3.8.2. Modelling:

To estimate the major energy costs and judge when to start regeneration, one needs to predict the cycle times and the silica gel saturation conditions. A mathematical model that reflects the silica gel properties dynamically with respect to increasing amounts of water vapour as fluid passes through is required. It is a common practice to analyse drying processes using breakthrough analysis that include the thermodynamic and kinetic effects of adsorption. A breakthrough curve is a concentration vs time curve as seen in the bottom half of Figure 3.10. The main parameters that influence this curve are column geometry, operating conditions, mass transport effects and equilibrium isotherms. Breakthrough analysis is widely used because of its ability to represent complex adsorption behaviour by later fitting it to basic data from experiments [25]. The following set of equations that form the model

and are attained from the work of den Haan [1], Nastaj and Ambrozek [26] and Park and Knaebel [6].

$$\Delta p = \frac{150\mu L}{D_p^2}\frac{1-\epsilon^2}{\epsilon^3}v_s + \frac{1.75L\rho}{D_p}\frac{1-\epsilon}{\epsilon^3}v_s\,|v_s| \tag{3.11}$$

$$P_{\text{losses}} = \Delta p * Q_v \tag{3.12}$$

$$X_w^* = X_{0,1}\exp\left[-\left(\frac{A}{E_{0,1}}\right)^2\right] + X_{0,2}\exp\left[-\left(\frac{A}{E_{0,2}}\right)^2\right] \qquad A = R\,\mathrm{T}\ln\left(\frac{p}{p_s}\right) \tag{3.13}$$

$$\frac{\partial X_w}{\partial t} = K_w\,(X_w^* - X_w) \tag{3.14}$$

$$\frac{\partial Y_w}{\partial t} = D_l\frac{\partial^2 Y_w}{\partial z^2} - \frac{J_i}{\epsilon\rho_i}\frac{\partial Y_w}{\partial z} - \frac{\rho_b}{\epsilon\rho_i}\frac{\partial X_w}{\partial t} \tag{3.15}$$

$$\frac{\partial T}{\partial t} = \frac{k_e}{c_\Sigma}\frac{\partial^2 T}{\partial z^2} - \frac{J_i c_{p_g}}{c_\Sigma}\frac{\partial T_w}{\partial z} + \frac{\rho_b \Delta H_w}{c_\Sigma}\frac{\partial X_w}{\partial t} - \frac{4k_w}{Dc_\Sigma}(T - T_\infty) \tag{3.16}$$

Here, in 3.11 and 3.12, Δp: Pressure drop (Pa),
μ: Dynamic Viscosity (Pa s),
L= length of bed,
D_p: particle size (m),
ϵ: void fraction,
v_s: superficial velocity of the fluid (m/s),
ρ: density of the fluid (kg/m^3),
P_{losses}: Power consumption due to pressure drop (W),
Q_v: volumetric flow rate (kg/s).
In 3.13, X^*_w: Equilibrium water content of the solid phase (kg/kg),
$X_{0,1}$: Parameter that depends on micropore capacities of the local site- 0.2753(kg/kg)
$X_{0,2}$: Parameter that depends on micropore capacities of the local site- 0.07302 (kg/kg)
$E_{0,1}$: Characteristic adsorption energy- 3443.4 (J/mol)
$E_{0,2}$: Characteristic adsorption energy- 10931 (J/mol)
P_s: Saturation partial pressure of water vapour (Pa)
In 3.14, 3.15 and 3.16, X_w: Water content of solid phase (kg/kg),
X_w: Water content of the solid phase (kg/kg),
Y_w: Water content of gas phase (kg/kg),
T: Temperature (K),
K_w: Mass transfer coefficient (1/s),
D_l: Gas diffusion coefficient (m^2/s),
J_i: Mass flux density (kg/(m^{2}s)),
ρ_i: density of inert gas,
ρ_b: bulk density of solid phase,
k_e: thermal conductivity of absorbent bed (W/mK),
C_{pg}: specific heat capacity of the gas phase (J/kgK),
C_Σ: Overall volumetric heat capacity (J/m^{3}K)
ΔH_w: Heat of adsorption of water vapour (J/kg),
k_w: overall heat transfer coefficient (W/m^{2}K),
D= diameter of the absorbent bed (m),
T_∞: Ambient temperature (K).

The Ergun Equation 3.11 and 3.12 is used to calculate the pressure drop across the packed bed and the energy associated with this drop, respectively. To model the adsorption process and determine the equilibrium state at a given point, the Dubinin-Radushkevich isotherm Equation 3.13 is used, which includes the effects of temperature and partial pressure of the adsorbed gas on its adsorption potential. Isotherms at different temperatures can be seen in Figure 3.9. It is clear that at very low relative

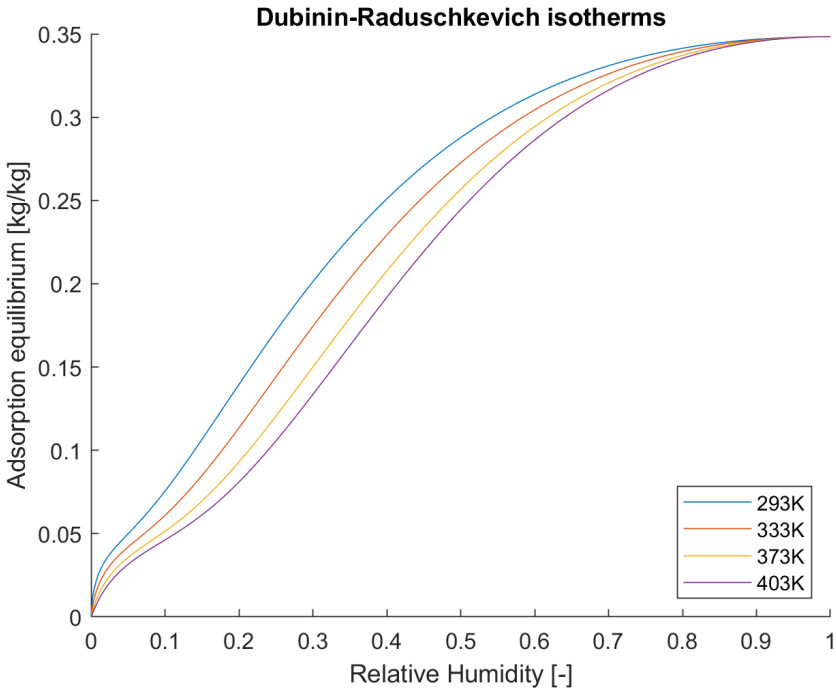

Figure 3.9: Dubinin-Raduschkevich Isotherms at different temperatures

humidities (<2%), the adsorbate-adsorbent concentration follows the simplest linear (Henry) isotherm- which is the case for almost all isotherms. When the first inflection point starts (RH>2%), each type of isotherm deviates from the Henry model owing to the average pore size. The second inflection point (RH=60%) is reached when the partial pressure inside the silica gel nears the saturation pressure. It can be seen that the adsorption concentration already reaches almost 85% of the maximum uptake at this point, and then a very slow increase to the maximum (0.35kg/kg), where condensation occurs. With increase in temperature, the maximum uptake concentration remains constant. However, the second inflection point comes earlier due to the reduced adsorption capacity of silica gel at higher temperatures.
The heat of adsorption ΔH_w in Equation 3.16 is calculated using the Clausius-Clayperon Equation 3.17 while the corresponding pressures are extrapolated continuously using the Tetens Equation 3.18 [27].

$$\Delta H = \frac{-\ln\left(\frac{P2}{P1}\right) R}{(1/T2) - (1/T1)} \tag{3.17}$$

$$P = 0.61078 \exp\left(\frac{17.27T}{T + 237.3}\right),\ T\ in\ [K]. \tag{3.18}$$

Linear Driving Force model is found best to describe the drying kinetics of porous desiccants like silica gel [28]. The increment in concentrations from equilibrium, where the change in water content in sorbent is given by 3.14, change in water content of the gas is given by 3.15 and change in the temperature is given by 3.16. This set of partial differential equations is converted into ordinary differential equations by discretising them spatially and dividing the packed bed into a number of sections. The spatial discretisation is done by central differencing method and is given by the Equations 3.19, 3.20 and 3.21. The dimensionless spatial and temporal coordinates are given by Z and τ respectively. These ordinary differential equations are solved at each time step and the new equilibrium state is found using Equation 3.13 and this process is iterated for the duration of an experiment.

$$\frac{\partial X_w}{\partial \tau} = \frac{\rho_{i0} L}{J_i} K_w \left(X_w^* - X_w\right) \tag{3.19}$$

$$\frac{\partial Y_w}{\partial \tau} = \frac{D_l \rho_{i0}}{J_i L \epsilon} \frac{Y_{n+1} - 2Y_n + Y_{n-1}}{\Delta Z^2} - \frac{\rho_{i0}}{\rho_i} \frac{Y_{n+1} - Y_n}{\Delta Z} - \frac{\rho_b}{\rho_i \epsilon} \frac{\partial X_w}{\partial \tau} \tag{3.20}$$

$$\frac{\partial T_n}{\partial \tau} = \frac{k_e \rho_{i0}}{J_i \rho_b L c_\Sigma} \frac{T_{n+1} - 2T_n + T_{n-1}}{\Delta Z^2} - \frac{\rho_{i0} c_{p_g}}{c_\Sigma} \frac{T_{n+1} - T_n}{\Delta Z} + \frac{\Delta H_w}{c_\Sigma} \frac{\partial X_w}{\partial \tau} - \frac{\rho_{i0} L 4 k_w}{J_i \rho_b D c_\Sigma} (T - T_\infty) \tag{3.21}$$

where,

$$\tau = \frac{J_i t}{\rho_{i0} L}$$
$$Z = \frac{z}{L} \tag{3.22}$$

The boundary conditions for this discretised system of equations are given by the set of equations in 3.23. The initial conditions indicate that the input conditions, which are relative humidity, temperature are predetermined. The initial gas water content, outside the column, is considered constant. Here, ϕ is the relative humidity and Y_s is the water content at saturation pressure.

$$\begin{aligned} Y_{w_{in}}(0,\tau) &= Y_S \phi \quad \text{at } Z = 0 \\ T(0,\tau) &= T_{in} \quad \text{at } Z = 0 \\ \frac{\partial Y_{w_{N+1}}}{\partial Z} &= 0 \quad \text{at } Z = 1 \\ \frac{\partial T_{N+1}}{\partial Z} &= 0 \quad \text{at } Z = 1 \\ Y_w(Z,0) &= Y_{w_0}(Z) \quad \text{at } \tau = 0 \\ X_w(Z,0) &= X_{w_0}(Z) \quad \text{at } \tau = 0 \\ T(Z,0) &= T_0(Z) \quad \text{at } \tau = 0 \end{aligned} \tag{3.23}$$

A Typical Run:

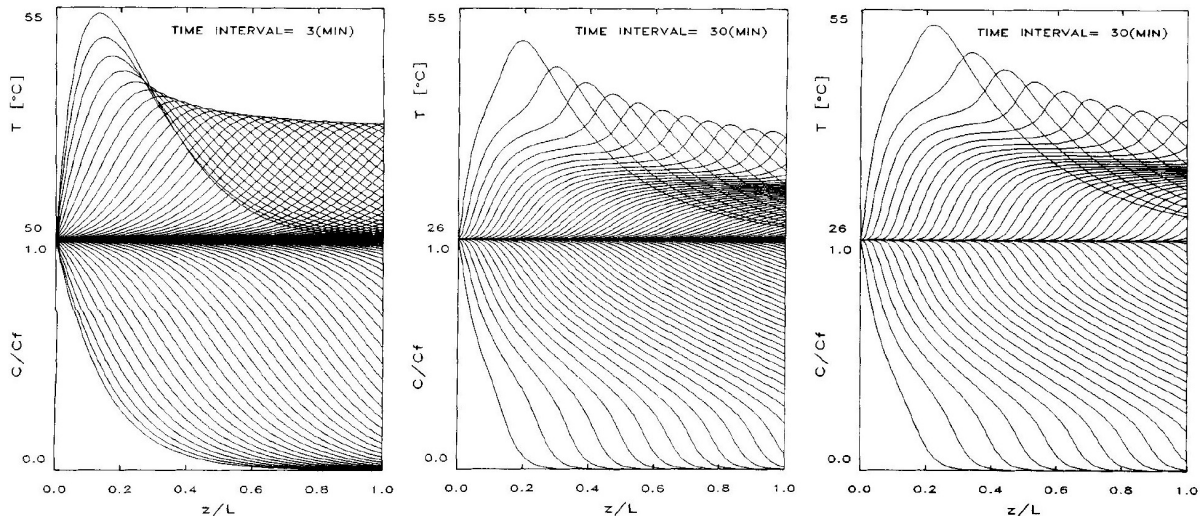

Figure 3.10: A typical run of the model taken from [6]
a- RH=0.058 at 50°C; b- RH= 0.56 at 26°C and c- RH=0.73 at 26°C

Figure 3.10 from [6] shows a typical run of a model that also describes adsorption of water by a silica gel packed bed column. The upper half of the graph shows variation of temperature over the length of the column over time and the lower half shows the same for concentration of water in silica gel. It is interesting to use this data from a breakthrough analysis to compare the effects of varying uptake relative humidities and/or uptake temperatures.
The concentration profiles in Figure 3.10(a) show an exponential decay at the start or inlet and towards the outlet the curve exhibits ‘single shock’ wave. As the intake RH increases, in Figure 3.10(b), the concentration profile exhibits a ‘double shock’ wave, which eventually becomes almost linear towards the outlet. The temperature profile in Figure 3.10(a) rises sharply at the inlet, due to the adsorption energy generated locally. Towards the outlet, the temperature peak flattens out and becomes broader due to saturation (or decrease in energy generated) of the bottom beads. It is also interesting to notice

that the temperature peaks occur when the concentration approaches initial intake concentration - in other words, when the beads are saturated. In Figure 3.10(b), the temperature peaks not only broaden but also decay towards the outlet. This can be explained by possible heat loss to the environment and mostly due to the reduced capacity of silica gel uptake at higher temperatures. The latter has a more pronounced effect in Figure 3.10(b) than Figure 3.10(a) due to the higher RH input. Even further increase in RH (73%) in Figure 3.10(c) shows the same effects as in Figure 3.10(b).

3.8.3. Goals and KPIs

As mentioned earlier in Section 3.8.1, the principal strategy for the operation of this system in tandem with two columns is the assumption that the time taken to heat the silica gel and to desorb water from it would be much shorter than the adsorption time- thus allowing for a continuous operation of downstream processes. Previous work done by [1] on a working prototype proves this hypothesis correct- both experimentally and mathematically. The model previously designed is capable of predicting the behaviour of half a cycle (either adsorption or desorption) at a time, then saving the end state to run for the next half of the cycle (desorption/adsorption). This successfully accomplished the goal of this model which was directed towards designing a functioning prototype that mimics work from known literature. Further, the following KPIs were considered:

- Cyclic capacity (difference in loading between a fully loaded column and a fully regenerated column)
- Energy consumption (cost of heating the hardware, gas, sorbent, desorption energy and losses to the environment)
- Desorption rate (quantity of water desorbed from the column per unit time)

However the measurement of each of these KPIs was limited by knowledge of only one cycle behaviour at a time. More insights into operational strategy of the system could bring in a new perspective to the KPI metrics. For instance, the previous energy cost estimation assumed complete (100%) regeneration of the desorbing column. This pushes the energy input of the heater and hardware to much higher values than the essential ones such as those of sorbent heating, gas heating and desorption energy costs. This is mostly because the energy taken to reach full desorption increases by a lot, after a period of time, with decrease in desorption rate. With a different operational strategy where the usage of only a partially regenerated column is possible- the energy costs would reduce dramatically. It is then crucial to have an understanding of a partially regenerated column that would still allow for a continuous downstream operation, by pushing back the adsorption front enough to operate for yet another cycle. In a similar fashion, the heater costs can also be diminished by studying when the equilibrium isotherm shifts to desorption, rather than having to maintain a constant wall temperature by continuously heating the column.
Another example would be the consideration of desorption rate alone as a KPI instead of comparing it to the adsoprtion rate as well- as the ultimate goal would be to design a system that spends more time adsorbing than regenerating or desorbing, especially considering the latter's energy costs. To gain insights into this, it is essential to have a system-scale model that includes both the columns working simultaneously with the compressor reloop- a model that can also predict the behaviour of multiple cycles over the entire operation time (8 h/day). It would then be possible to see the variation of these KPIs over a relevant time-scale and have a better judgement about the trade-offs to be made in the design choices.
At the end of the previous project, the drying system was shown capable of stripping the CO_2 to 98% purity. However, the columns are yet to be connected to the compressor train and their cycle times need to be matched to that of the compressor. Based on the previous work, it was clear that the desorption cycle time of the column was significantly lower than the absorption cycle time. To predict their behaviour when integrated, the two columns needed to be coupled, saturated and accounted for regeneration. Following the recommendations of the predecessor, the method of heating has been modified to a heater placed in the middle of the drying columns, at the top and bottom ends. This also needs to be modified in the new model.

3.9. Existing work at ZEF

Reprising the important decisions made by ZEF to compress and purify the low pressure (1bar) CO_2 from DAC output stream to a dry, high pressure (55bars) CO_2:

- A rolling piston type compressor is selected and partially redesigned.
- A multiple stage compression system will be used, with the redesigned modular compressors.
- A desiccant-based drying system with two columns is designed to improve the lifetime of the compressor (oil) yielding a purer (98%, by weight) CO_2 stream.

3.10. Objectives of this work

Previous work done at ZEF on the FM system investigated the steady-state analysis of the modular compressors and the drying systems (one cycle) individually. The internal behaviour of each system was studied. However, in order to provide a design tool to ZEF that predicts the behaviour of the entire system over time, the following work is yet to be done:

- Study of multiple drying cycles over the operational time (8hours/day) of both the columns
- Dynamic effects of integration on the drying and compressor systems
- Correction of the compressor model to predict realistic behaviour.
- Compressor model to predict the continuous/dynamic operation accurately.
- Drying system model to account for the regeneration time and changes in the heating method.
- Effects of external systems (DAC output) on the FM system in order to replicate the actual operating conditions and vice versa.

4

Methodology

In order to deliver the goal of this thesis, an approach needs to be devised and followed. This chapter, therefore, discusses

1. Modelling Approach
2. The process parameters and key performance indicators of the subsystems
3. The characteristic time scales of relevant phenomena and their significance
4. Characterisation of the drying system

4.1. Approach

The goal of this thesis is to make a dynamic model of the entire FM system, which is the drying system coupled with the compressor(s). A layered approach, shown in Figure 4.1, is going to be followed where first the steady state models of the subsystems will be assessed and later be combined. The dynamic behaviour of the individual subsystems will then be added as another layer for the relevant phenomena and ultimately be combined to form the whole FM system. Simulink in Matlab is the chosen tool for this model as it allows the model to be built up in blocks that can be layered to increase complexity. Another reason for the choice was the ease of accessibility of the model for future research. For each model (steady state/ dynamic), the approach, taken from [29], will be to define each of the following steps:

1. Purpose: to define why the model needs to be studied- what are the key performance indicators?
2. System Borders + Variables: find the scope of the system and its inputs and outputs
3. Relevant Phenomena: which of the effects of the inputs on the KPIs are significant?
4. Hypotheses/ Assumptions: what are the observations from literature and what can be neglected?
5. Sub models: making blocks of relevant phenomena in each subsystem
6. Conservation laws + relations: to note the governing equations and the boundary conditions
7. Simplifications: which effects can be neglected and/or to make the models run faster, while lying in the numerically stable limits.
8. Simulation: Implement the mathematical model onto a modelling tool
9. Validation, Documentation and Application: validate predicted results against experimental values

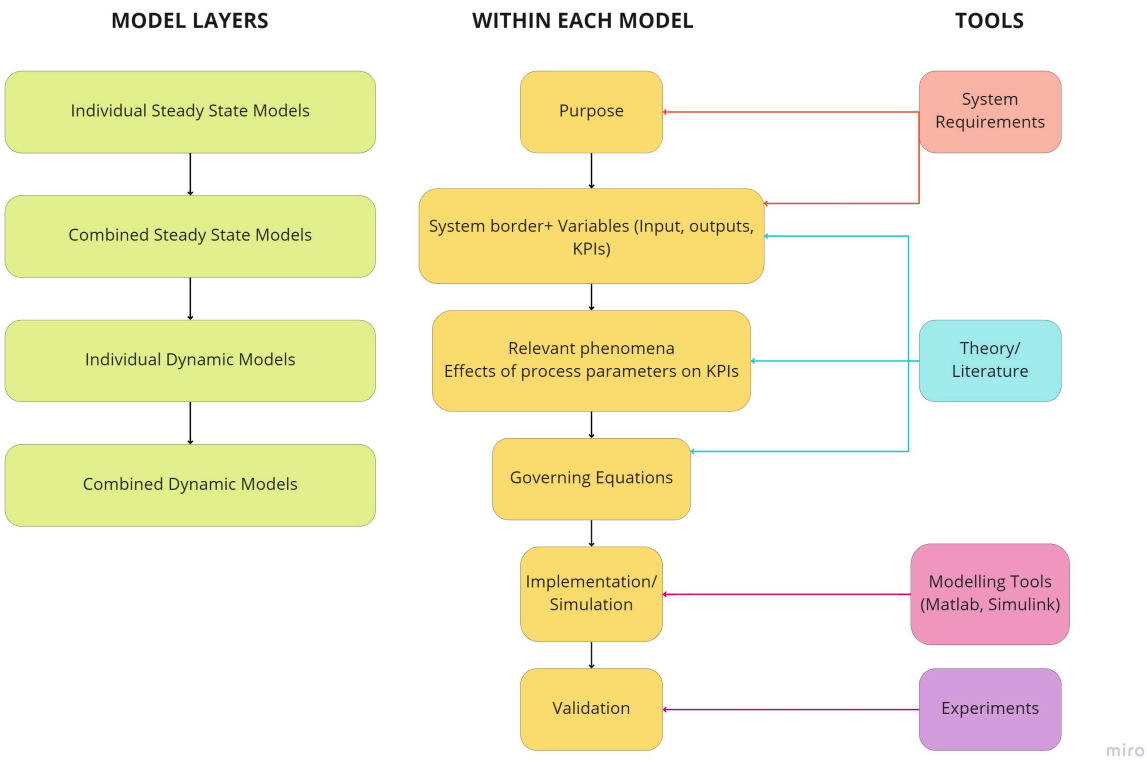

Figure 4.1: Layered modelling approach with the required tools

Figure 4.2: Modelling Approach

4.2. Purpose

The purpose of this model is to provide ZEF with a development tool that can predict the reaction of the FM system in a dynamic environment and ultimately provide a control strategy to operate in the optimum operational envelope. It also aims to give new insights into the science of micro-scale rolling piston compressors operating in high pressure conditions with very low and dynamic mass flow rates.

Moreover, despite the fact that drying accounts for 12% of all industrial energy expenditures [30], there is very little research done to model multiple cycles, albeit over a longer period of time and analyse it. This thesis aims to shed new light on both these gaps in science, while integrating them for ZEF's design needs.

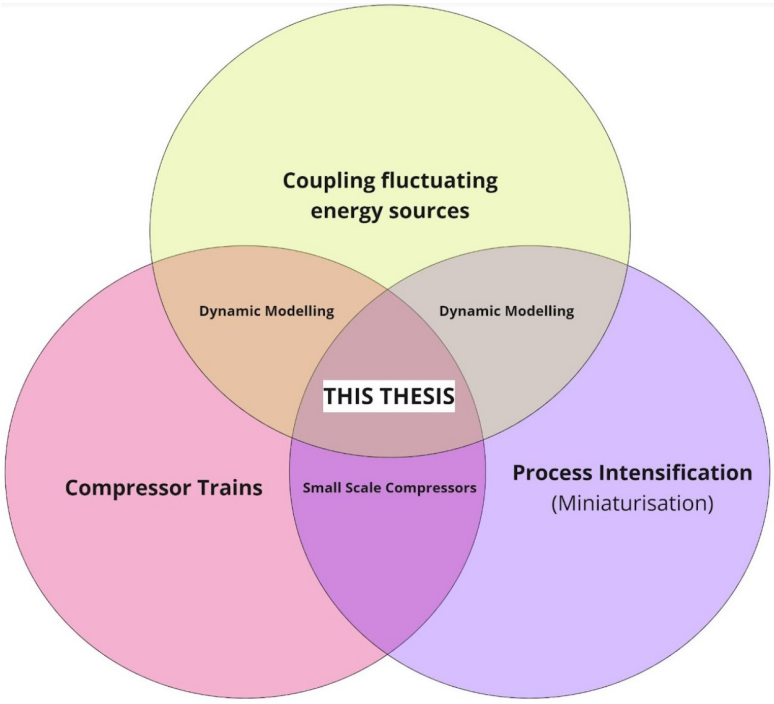

Figure 4.3: Scientific Relevance of this thesis

4.3. Key Performance Indicators

After studying the systems and ZEF's requirements[1], the most interesting parameters were selected to be studied in the model. The devised model, at the end of this study, should replicate the actual effects of the process parameters on each of the KPIs (shown in Table 4.1).

Table 4.1: Key Performance Indicators of the FM system

		DRYING SYSTEM	COMPRESSOR
PROCESS PARAMETERS	**Inputs**	Input quality (wt%), Relative humidity	Fluid pressure
	Temperature	$T_{ambient}$, T_{heater}, $T_{wet\ gas}$, $T_{re\text{-}loop}$	T_{Inlet}, T_{outlet}
	Dimensions	Silica gel diameter, column length, column diameter, void fraction	Buffer volume, displacement volume
	Properties	Packed bed conductivity, heat and mass transfer coefficients	Specific heat ratio (γ_{gas}), polytropic index
KPIs		Output quality (wt%)	Output Pressure
		Pressure drop across the drying column	Mass flow rate output
		Regeneration energy (Heat input)	Compression power
		Cycle Time [h]	Isentropic efficiency
		Cyclic Capacity [kg/cycle]	

[1] Discussed in Section 3.8.3

4.4. Relevant Phenomena

Identifying the phenomena that are occurring in each subsystem and measuring on what characteristic time scales they are relevant is important to estimate their significance. This also guides the assumptions going into classifying the steady and dynamic processes, when the individual models are eventually developed. Figure 4.4 shows the relevant phenomena against a characteristic time scale ranging from nanoseconds to five years. Bearing the KPIs in table 4.3 in mind, the phenomena that affect them are enlisted. This list is made as extensive as possible after studying the geometry, thermodynamics and workings of the compressor and drying system. However, it is non exhaustive as the experiments are yet to be performed. The key advantage of this process is that, it can be reassessed with experimental findings. And in doing so, it remains non-disruptive to the modelling process as it can be added to one of the layers (or blocks) in the final model (which is supported by Simulink).

In Figure 4.4, the orange circle encompasses the time scales (minute to eight hours) that the dynamic model needs to focus on. The maximum of the range is taken due to eight hours being the operation time of the plant during a day and the minimum is taken keeping which effects could accumulate and contribute significantly to the dynamic mode at the end of a day. The events occurring outside the orange bubble, on the left (from nanosecond to a minute) are assumed to happen instantaneously and remain in steady state. The effects of events occurring outside the orange bubble, to the right (from eight hours to five years and beyond) are assumed to be non-existent (zero). The phenomena inside the bubble will be time-dependent models. The enlisted effects are discussed as follows:

1. **Compressor chamber volume changes due to vane switching:** The rolling piston compressor works so that the fluid is compressed due to volume changes caused by the roller movement. During this process, the vane also reciprocates accounting to some volume changes. The frequency of this occurs at an rpm level and is too small to be modelled with variations in time. It can be accounted for in volumetric efficiency of the compressor, as a constant value.

2. **Temperature effects on the fin[2]:** The main modes of heat transfer from the compression chamber to the fin are convection and conduction. To assume the temperature of the fin to be steady state, these modes of heat transfer must be accounted for. The Biot number gives the ratio of conductive and convective resistances. The effects of heat generation inside the compressor on the fin temperature are considered to be negligible due to a low Biot number (high conductivity) of the aluminium fins.

$$\mathrm{Bi} = \frac{h}{k} L \tag{4.1}$$

where, k of aluminium is $237 W/mK$, h_{air} is $25 W/m^2K$ [31]and L is in the magnitude of 10^{-2} m, therefore the Biot number is well below 0.1, to justify the assumptions.

3. **Fan energy input:** The amount of energy consumed by the fan increases with the duration of operation and is important to the efficiency of the total system. However this input is a constant over time and can be considered an instantaneous increase as it is switched on.

4. **Cooing due to oil passing through the compressor:** If the oil entrapped in the thin valves of the compressor would break into tiny droplets (atomise), then it would lead to a cooling effect on inside the compressor. This is due to the increased surface area for heat transfer, caused by the droplet formation. In addition, there would be increased heat transfer due to the higher heat capacity of the lubricant oil than that of CO_2. To investigate the droplet formation, the Weber Number, given by Equation 4.2, (for surface tension effects) and the Ohnesorge Number, given by Equation 4.3, (for viscosity effects) must be determined. When the critical Weber number associated with the Ohnesorge number is equal/ close to the Weber number, a final droplet size is assumed. The critical Weber number associated with an Ohnesorge number is given by [32] and [33].

$$We = \frac{\rho_{\mathrm{CO}_2} u^2 D_d}{\sigma} \tag{4.2}$$

[2]At a later stage, the compressor used in the integrated working setup did not use a compressor housing with fins.

$$Oh = \frac{\mu}{\sqrt{D_d \rho_{oil} \sigma}} \tag{4.3}$$

σ- surface tension of the oil 0.0286[N/m], ρ- density of CO_2 1.7 [kg/m^3] and density of oil is 977 [kg/m^3], μ- dynamic viscocity of the oil 0.19 [Pa/s] at inlet and 0.0025 [Pa/s] at outlet, obtained from the oil data sheet, D_d- droplet diameter taken to be 1000[μm], u- tangential velocity [m/s] which depends on the RPM, compression chamber diameter (D_C) and length of gap (L_g) given by

$$u = \omega r = 2\pi \frac{RPM}{60} \frac{D_c - L_g}{2} \tag{4.4}$$

The droplet size found for the dimensions of the compressor used for this project (Stage 1, up to 8bars) exceeds 1000 μm. The atomisation of droplets beyond this measure does not have any significant effect on the heat transfer and can be considered negligible.

5. **Back-flow at outlet:** As mentioned in Chapter 3, at the start of compression, there is a pressure difference between the compression chamber and outside the discharge valve, which results in a back-flow. Due to this, there is a loss as more work is being done on already compressed fluid. This also, however, occurs at an rpm level and can be lumped into the volumetric and thermal efficiencies of the compressor, as a constant.

6. **Internal leakages:** Due to the tolerances inside the compressor, there are expected to be a couple of leakage paths where the compressed air goes out, resulting in a pressure drop due to re-expansion. However, this is highly dependent on the frequency (rpm) of a compressor. As a result of predecessor's work [8], a linear relationship was found between the leakages and the output pressure (at a given rpm), which can be taken into account in the overall volumetric efficiency.

7. **Temperature effects on the casing:** The temperature effects on the casing accumulate over the duration of operation (eight hours) due to the high thermal inertia of the aluminium casing. It is therefore considered important to model this over time. Thermal inertia or volumetric heat capacity is a bulk material property that depicts its tendency to withhold heat for a long period of time or its resistance to transmission. It is the product of material properties that have an effect on the rise in temperature and is given, for aluminium, by:

$$I = \sqrt{k\rho c} = 24.1 \times 10^3 J/m^2 K s^{\frac{1}{2}} \tag{4.5}$$

8. **DAC output pressure fluctuations and changes due to the drying system:** As the conditions (temperature, pressure, quality) of CO_2 captured by the DAC system are highly dependent on the ambient conditions, these inputs are considered the most volatile working conditions of the input fluid. The fluctuations in ambient occur due to seasonal and day-to-night variations and are very relevant to the characteristic time scale of the model. These fluctuations can be dampened to some extent using a buffer at the end of the output stream, whilst also sizing the tank (discussed in Point 15)accordingly. It is aimed to keep the fluctuation in pressure changes above 20 mbars to avoid any leakages.

9. **Friction losses:** Due to the increase in temperature of the compressor over the duration of operation, the mechanical losses inside the compressor also increase.

10. **Heat capacities:** The values of convective heat transfer coefficients of air (h_{air}), specific heat capacities at constant pressure (C_p) and at constant volume (C_v) change with temperature and so does their ratio (γ) The rise in temperature occurs throughout the duration of operation due to heat generation inside the compressor (due to compression, friction etc) and also due to changes in ambient (happens significantly over a day-to-night scale). Therefore, this is included and significantly influential in the characteristic time scale of the model.

11. **Metal expansion:** The effects of metal expansion are changes in compression chamber volume and heat exchange surface to volume ratio of the housing. The thermal expansion coefficient (αL) of aluminium is 23.6e-6 (m/m°C) [31] and the length of the aluminium housing is 12cm, which

gives the change in length per rise in one °C as 3e-6m, which is negligible. The characteristic time scale of this is also higher than the duration of operation, as the length of expansion is only significant for higher temperature differences, which might be possible for a longer operation time of the compressor.

12. **Motor heat generation:** According to [22], motor losses are highly significant and could contribute up to 50% of the losses, over the duration of operation. Therefore, this will need further investigation in the case of ZEF's compressors (see section 6.5).

13. **Changes in RH & Temperature due to the drying system:** Due to the continuous operation of the two drying columns, the RH and temperature of the output gas change over time of operation. This variation increases dynamically over time, as the silica gel beads get more saturated and lose capacity to adsorb further. It is one of the main phenomena to be modelled in this project along with 14 and 15.

14. **Changes due to compressor in pressure of the reflux fluid:** As there is mass flow to and from the compressor into the drying system, the pressure and temperature effects of the reflux mass flow on the drying column must be modelled.

15. **Effects on DAC Buffer (upstream) due to variation in pressure:** In the end, the wet CO2 that is purged from the desrobing column goes back into the DAC flash tank, to keep the system closed and to conserve the CO2 captured. This backflow and the pressure variations caused by it inherently has effects on the DAC Flash Tank sizing. The sizing of the flash tank depends on the sorbent levels inside the DAC stripper. As the sorbent has a density close to 1 g/cc, a change in pressure of 1 mbar inside the flash tank will lead to a 1cm rise in sorbent level. A high pressure difference will lead to either

    - High pressure in the stripper requiring most of the sorbent to be purged out of the stripper- which is undesirable, or
    - Low pressure in the stripper leading to a higher intake of sorbent which might lead to an overflow into the buffer.

    This prescribes a maximum of 20mbar of pressure difference in the DAC buffer flash tank.

16. **Changes in solar irradiation:** Due to the variation of solar irradiation over the period of a day, the power supplied to all the subsystems will be affected. Although this remains true, the power supply of the components involved in FM is a constant voltage supply. Therefore, any voltage lower than this would mean a total shutdown of the subsystem. Besides the power supply, this also has effects on the air quality variations throughout the day, which could influence the RH input of the drying system. The time-scale of these variations could also be increased to half-year, if seasonal variations are to be considered. However these are considered out of the scope for this research.

4.4.1. Characterisation of the Drying System

To derive the parameters given in equations 3.14, 3.15 and 3.16, an understanding of the transport phenomena inside the drying system is required. Thus a scaling analysis is performed and the drying system is characterised. The correlations used to obtain various parameters in the aforementioned equations are also listed below.

1. **Permeability:** It is a transport phenomenon that quantifies the ease with which a transporting substance can pass through the material. It is an important parameter that helps estimate the pressure required for a flow to pass through a packed column- thus also allowing to calculate the energy required to drive this flow [34]. It depends on the moisture content, solid phase geometry (pore structure) and porosity and can be calculated using the Kozeny Carman Equation given by Equation 4.6, for packed beds of uniform spherical particles 4.6 [35]

$$K = \frac{d_p^2 \varepsilon^3}{\beta(1-\varepsilon)^2} = 1.2 * 10^{-7} m^2 \tag{4.6}$$

Here, ϵ is the void fraction (0.6), d_p is the particle diameter (4mm) and β is taken as 180 from [36] and [37].
The pressure difference through the packed bed of silica can then be calculated using this permeability and the Darcy's Law for fluid flow through porous media given by Equation 4.7.

$$q = -\frac{k}{\mu L}\Delta p \tag{4.7}$$

Here, q is fluid flux [m/s] k is the permeability [m^2], μ is the dynamic viscosity 1.837e-05 [Pa.s], L is the length of the column 0.3[m] and δp is the pressure drop [Pa]. From this the **pressure drop is calculated to be a meager amount of 3.45 Pa, which can be negligible** keeping in mind the outlet conditions of DAC being 10^5 Pa (1 bar) and outlet conditions of the compressor being $55{*}10^5$ Pa (55 bars).

2. **Axial diffusion coefficient:** All the mechanical diffusion effects are lumped with the molecular diffusion in this term [38]. In this work, five different correlations are given for Axial diffusion based on the Peclet (Pe) number of the pellets as a function of the Reynolds number (Re) and Schimdt (Sc) number. Various correlations of Pe are given by [39] for Equation 4.9, [40] for 4.10, [41] for 4.11, [42] for 4.12 and [43] for 4.13.

$$Re = \frac{2\rho_f \varepsilon v_i R_p}{\mu}; \quad Sc = \frac{\mu}{\rho_f D} \tag{4.8}$$

$$\frac{1}{Pe} = \frac{20}{\varepsilon}\left(\frac{D}{2vR_p}\right) + \frac{1}{2} = \frac{20}{R_{eSc}} + \frac{1}{2} \tag{4.9}$$

$$\frac{1}{Pe} = \frac{0.73\varepsilon}{\mathrm{ReSc}} + \frac{1}{2\left(1 + \frac{13\cdot 0.73\varepsilon}{ReS_c}\right)} \quad 0.0377 < 2R_p < 0.607 \text{ cm} \tag{4.10}$$

$$\frac{1}{Pe} = \frac{0.45 + 0.55\varepsilon}{\mathrm{ReSc}} + 0.5 \tag{4.11}$$

$$\frac{1}{Pe} = \frac{0.7\varepsilon}{\mathrm{ReSc}} + 0.5 \tag{4.12}$$

$$\frac{1}{Pe} = \frac{0.3\varepsilon}{\mathrm{ReSc}} + \frac{0.5}{\left(1 + \frac{3.8}{ReS_c}\right)} \quad 0.008 < \mathrm{Re} < 400 \quad 0.28 < Sc < 2.2 \tag{4.13}$$

where, R_p is the pellet radius 2[mm], v is the superficial velocity and D is the diffusion coefficient. A suitable relation out of these can be chosen to calculate the Peclet number and the corresponding axial diffusion coefficient can then be obtained by:

$$D_L = \frac{2vR_p}{Pe} \tag{4.14}$$

As the Re and silica gel bead size used in this project are within the range given by 4.10, the given **Edwards-Richardson correlation is used.** This method is also selected by works similar to this (TSA using silica gel packed bed) [6] and [44] for calculating D_l. A simplified form of this correlation, that is implemented in the model is:

$$D_L = 0.73D_M + \frac{0.5ud_p}{(1 + 9.7D_M)/(ud_p)} \quad \begin{matrix}(0.008 < Re < 50) \\ (0.377 < d_p < 6 \text{ mm})\end{matrix} \tag{4.15}$$

3. **Correlations used to obtain heat and mass transfer coefficients:** There is a huge variation in literature about the methods used to obtain the heat and mass transfer coefficients. For example, Plumb et al. [45] calculate the convective heat transfer coefficient (h) by the Nusselt number (Nu), which in turn depends on the flow geometry, Reynold's number and Prandtl number. Then they

proceed to use the Chilton-Colburn analogy in Equation to derive the mass transfer coefficient. Via this approach, the mass transfer coefficient, h_m, is found to be 0.016 [m/s].

$$h_m = \frac{hD_c Le^{1/3}}{k} = 0.016 m/s \tag{4.16}$$

here, Le is the Lewis number- which can be considered 1 for water vapour in air, h is the convective heat transfer coefficient of air 20 W/m^{2}K], k is the thermal conductivity of air which is 0.025 [W/mK] and D_c is the diffusion coefficient of water vapour in air 2$*$10^{-5} [m^2/s].
In other works like [38], the mass transfer and heat transfer coefficients from gas phase to solid pellets are calculated using a film diffusion empirical correlations that use the Reynolds number and the Sherwood number. Then the heat transfer from fluid to wall using another empirical correlation by [46]. However this study was performed for packed zeolite (5A) beds and not silica gels.
In a study of TSA for Butanol dehydration using zeolite (3A) by [47], the mass transfer of the linear driving force model is derived by Equation 4.17 supported by the film diffusion coefficient given by Equation 4.18

$$\frac{1}{K} = \frac{d_\mathrm{p}}{6k_\mathrm{f}} + \frac{d_\mathrm{p}^2}{60\varepsilon_\mathrm{b} D_\mathrm{p}} \tag{4.17}$$

$$\frac{k_\mathrm{f} d_\mathrm{p}}{D_\mathrm{AX}} = \frac{1.09}{\varepsilon_\mathrm{b}} \left(\frac{\mu_\mathrm{L} D_\mathrm{AX}}{\rho_\mathrm{l}}\right)^{1/3} \left(\frac{u_\mathrm{LR} d_\mathrm{p} \rho_\mathrm{l}}{\mu_\mathrm{l}}\right)^{1/3} \tag{4.18}$$

A model by [48] of a packed bed drying of willow chips with forced air convection also uses an empirical relationship to derive the heat transfer coefficient from the Nusselt number (Nu), Reynold's number and Prandtl number. It then follows to use a modified version of the Chilton-Colburn analogy to calculate the mass transfer coefficient [49]. However all of the above studies [45], [38], [48], [47], among many others, concluded that the theoretical estimations of these coefficients deviated from reality. This remains prevalent especially for the mass transfer coefficient, which is usually fitted to the experimental data.
Studies by Park and Knaebel [6] and Nastaj and Ambrozek [26], that have comparatively similar settings to this project, use a fitted **overall heat transfer coefficient of 8.37 [W/m^{2}K].** This overall coefficient considers the effects of natural convection to the external wall given by [50], thermal conductivity of the wall and the internal effective heat transfer coefficient given by [51].
From the same works, an estimate for the mass transfer coefficient was found to be 0.018 [s^{-1}], which is close to the one given by the Chilton-Colburn analaogy, Equation 4.16 for this setup. However, later on, a better suited **Petrovic and Thodos empirical correlation** found in works of [52] and [39], is **used for the mass transfer coefficient.** This helps ensure degree of freedoms for future design iterations- by providing a consistent calculation for varying sizes of silica gel or column dimensions, for the given Re and R_p.

$$K_f = \frac{0.357}{\epsilon} Re^{0.64} Sc^{0.33} \frac{D_m}{2R_p} \quad 3 < Re < 2000 \tag{4.19}$$

$$K = K_f \frac{\alpha}{\rho} \tag{4.20}$$

where K is the overall mass transfer coefficient, K_f is the fluid-film mass transfer coefficient, α is the surface area to volume ratio and D_m is the molecular diffusivity of water in air.

4. **Biot Number (for mass transfer):** The Biot number which is a ratio of conductive and convective heat transfers gives a good judgement of whether the system can be lumped or not. If the Biot number relating to the mass transfer of the drying system is less than 0.1, then the saturation gradients within the drying material (silica) can be neglected- hence, the model can be lumped [45].

$$Bi_m = \frac{h_m L}{D_l} \tag{4.21}$$

where h_m is the mass transfer coefficient 0.016 [m/s], as calculated from Equation 4.16, L is the thickness of the column 0.036[m] and D_l is the effective diffusivity of the liquid phase (water) given

as 1.34e-04 [m^2/s] by [45]. This gives a high Biot number of 4.43, reinforcing the assumption that the saturation gradient cannot be lumped. In other words, the drying rate is not constant and the time dependence needs to be modelled (as done using the Linear Driving Force method here).

5. **Thermal conductivity:** An effective thermal conductivity is necessary to model the heat transfer inside the bed that happens via conduction. A relationship for an quiescent bed of spherical particles is given by [38] in Equation 4.22 and is corrected to the fluid flow in Equation 4.23

$$k_e = k_f \left(\frac{k_s}{k_f}\right)^n \quad \text{with} \quad n = 0.280 - 0.757 \log_{10} \varepsilon - 0.057 \log_{10} \left(\frac{k_s}{k_f}\right) \tag{4.22}$$

$$k_{eff} = k_f \left(\frac{k_e}{k_f} + 0.75 \,\mathrm{Pr}\, Re\right) \quad \text{where} \quad \mathrm{Pr} = \frac{c_p \mu}{\rho_f k_f} \tag{4.23}$$

where k_e and k_{eff} are the effective thermal conductivity coefficients without and with flows and Pr is the Prandtl number.
It is unclear how a similar work of Park & Knaebel [6] obtains this value, but from literature about moist silica gel, it is found to be 0.2[W/mK] [53] and [54].

6. **Adsorption Equilibrium Isotherms:** It is important to know the profile of equilibrium concentration increases over temperature. In literature, these profiles are classified into six different types of isotherms, based on the type of adsorbent, type of adsorption and interactions amongst the adsorbent particles. The most widely used isotherms for single-solute adsorption are Langmuir-Freundlich isotherm and the Dubinin-Radushckevich isotherm [55]. Literature survey by [56] about experimental data on adsorption by regular-density silica gel concludes that it can be represented by a type-IV isotherm. A generalised form of this **adsorption isotherm is the one given by the Dubinin-Radushkevich** [57] (also sometimes referred to as the Dubinin-Astakhov isotherm). This relation is used to calculate the equilibrium states in this model, as mentioned in section 3.8.2.

7. **Pressure drop across the packed bed:** As mentioned before, the pressure drop across the packed bed does not only influence the energy required for the drying system to pump fluid through, it also increases the energy costs of the compressor downstream. A negligible amount of pressure drop (3 Pa) was estimated from point 1. As this is one of the KPIs of the model, a more accurate relationship in the form of the Ergun Equation is used.

$$\Delta p = \frac{150 \mu L}{D_p^2} \frac{(1-\epsilon)^2}{\epsilon^3} v_s + \frac{1.75 L \rho}{D_p} \frac{(1-\epsilon)}{\epsilon^3} v_s \left|v_s\right| \tag{4.24}$$

From this equation, an addition of the ‘pressure drop due to inertia’ term can be discerned from the v_s^2 term. In the Carman Kozeny Equation 4.6, only the first term which gives the pressure drop due to laminar flow. The Ergun Equation, as expected, gives a higher **pressure drop of 15 Pa**. However this is still **negligible** when compared to the inlet (1e05 Pa) and outlet conditions (55e05 Pa) of the system.

4.5. Next Steps

4.5.1. Governing Equations and Implementation

After understanding the relevant phenomena to be modelled in each subsystem, their governing equations (discussed in Chapter 3) are implemented into models on Simulink (Matlab). The existing drying system and its model will be studied to see how it can be adapted to have two columns functioning dynamically, spanning over the time of multiple cycles, along with control logic. It would also be further developed for more accuracy to fit the new experimental setup, which could effectively reduce the model’s computational time. Different stiff system numerical solvers (and their settings) for the drying system model will be studied to optimise computational time while moving the model from Matlab to Simulink. The compressor model built by the predecessor will not be used for further analysis, as it dissects the internal thermodynamics of the compressor, at time scales that are not relevant to this work. A thorough documentation of these models, their results and discussion are presented in Chapters 3.8.2 and 6.

4.5.2. Validation- Experimental Plan

A prototype of an integrated setup (with two drying columns and first stage compressor) already exists at ZEF. The dynamic model will be validated by performing experiments using this setup. The design of the modular compressors at ZEF is an iterative process and the latest work by [5] mentioned in this report, is still in progress. For the scope of this thesis, a modular compressor integrated with the drying system will be modelled and tested.

The working fluid for all the gathered experimental data is air and not CO_2. This is due to safety reasons imposed at a lab-scale in ZEF. Therefore, both the compressor and drying system models need to be built to integrate both these fluids' properties. Air- for validation purposes and CO_2 for future research and design purposes. Further, the model and experimental conditions are designed to match the water content [kg/kg] in air to that of CO_2 at a given temperature.

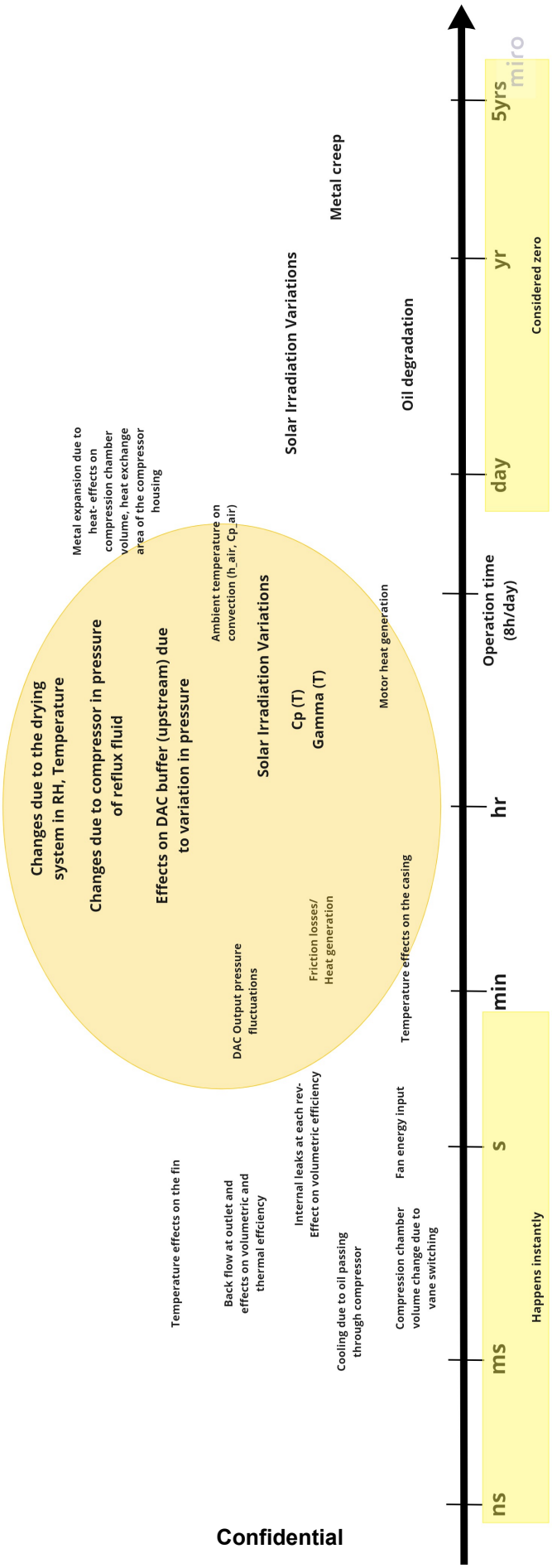

Figure 4.4: Relevant phenomena occurring against a characteristic time scale

5

Drying System Model and Validation

In this chapter the following topics will be elaborated:

- Goal of this model
- Working of this model and its assumptions
- Model results and discussion
- Experimentation methods, results and discussion
- Validation with experimental data and data from literature
- Usage as a design tool

5.1. Goal of this model

The goal of this model is to provide a design tool to ZEF that depicts the dynamic behaviour of the drying system. To accomplish this goal, the drying system model should be able to simulate multiple cycles over longer periods of time (at least 8 h/day). This would include incorporation of an automated control strategy so that both the columns can work in tandem and ensure a continuous operation of the whole system. The model should also be able to adapt to future design iterations at ZEF so it can be used as a design tool.

5.2. Model Assumptions

After already studying the relevant phenomena occurring inside the drying system, as done in Section 4.4.1, some of the effects were quantified. Different empirical correlations chosen and their explanation is also discussed. Certain assumptions about the model can thus be made as follows.

- There are two fluid phase components, that comprise an ideal gas mixture.
- Only one component adsorbs, described by an equilibrium isotherm given in Equation 3.13.
- Linear Driving Force model represents the deviation from equilibrium/ steady-state for both the fluid and adsorbent particles. It is given by Equation 3.14.
- Pressure gradients are negligible[1].
- Thermal exchange across the column wall can be lumped into an overall heat-transfer model.
- The concentration gradient and temperature gradients are only 1-Dimensional.

[1] As shown by the Ergun Equation in Section 4.4.1.

The concentration gradient can be assumed constant radially as the mass flow into the column is uniform throughout the inlet cross-sectional area. If a homogeneous distribution of the spherical silica gel beads packing is assumed, then the concentration difference would only occur along the length of the column.
silica gel is a widely used desiccant, which has the affinity to adsorb many kinds of materials. Carbon dioxide could also be potentially adsorbed by silica gel, in environments where there are other less-selective materials like methane or butane[58], [59]. Nevertheless, in this scenario, the two fluid components are H_2O and CO_2. The desiccant used here is anhydrous silca-gel, which formerly exists in the wet form ($SiO_2 \cdot nH_2O$). Therefore, the anhydrous form has a high affinity towards the water molecules, first. Besides that, silica gel is also a polar adsorbent which makes it even more selective to another polar compound like H_2) when compared to a non-polar compound like CO_2 [60]. Due to these reasons and the bond strength of the H-H type bonds, only more water is expected to be adsorbed by the silica gel, reinforcing the assumption that only one component is adsorbed by the porous desiccant.
The temperature gradient can be assumed one- dimensional due to the change in the heating systems

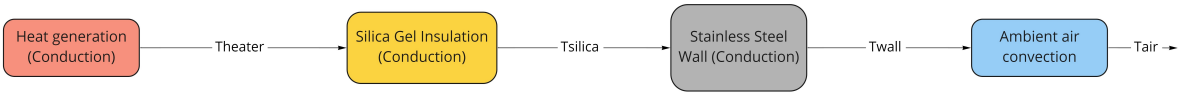

Figure 5.1: Thermal circuit inside a drying column using rod heaters

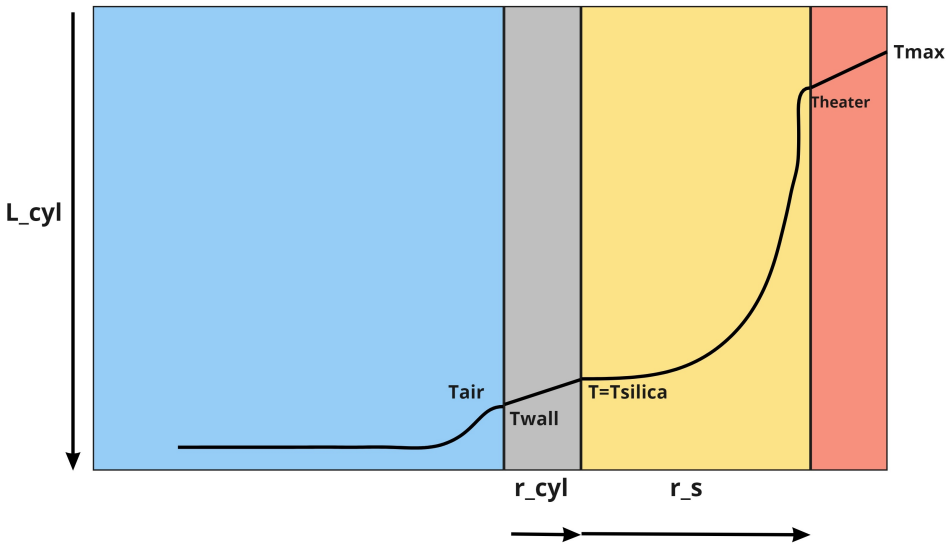

Figure 5.2: Temperature profile in the radial direction using rod heaters

of the setup. Firstly, 'rod heaters' placed in the middle (core) of the drying columns were used to heat up the system and bring it to desorption temperature following the recommendations of previous work, as mentioned in Section 3.8.3. However if this was the case, the heat transfer would have been a 2-D model with the heat transfer in radial direction looking somewhat like in Figure 5.2[2]. This is a result of a simple heat transfer model of a pipe with heat generation at the core and silica gel as an insulation layer. The thermal circuit is shown in Figure 5.1. Results from this model and experimental data showed that the silica gel posed too much insulation- which resulted in an uneven temperature profile amongst the silica beads in the radial direction, as can be seen in the Figure 5.2. This is undesirable for desorption needs as all the beads need to be at desorption temperature to regenerate as quickly as possible. Moreover, since the heaters would still keep heating up, more energy costs would also be involved.

[2]Detailed description about this model is given in Appendix C.

One way to increase heat transfer and ensure an even distribution of temperature in the silica gel is to increase the surface area to volume ratio of the heaters. In other words, the rod heaters need to be replaced with devices that have more contact area with the silica beads. Therefore, a switch to another type of heating system which uses 'band heaters' is made. These heaters are made of silicone pads that encircle the steel walls of the column. The warm-up time of these heaters was calculated by measuring the temperature at the core of the column and just outside the column. Since the steel wall is highly conductive, the temperature loss inside the wall can be neglected. The warm-up time was acceptable, being 30 minutes. Therefore the second method of heating using the band heaters was used. Since the band heaters surround the entire length of the column uniformly, heat transfer can be considered 1-Dimensional.

5.3. Working of the model and implementation

The fundamental energy and mass balances (linear driving force model) inside the column, the adsorption isotherm (Dubinin-Raduschkevich) mentioned in the Section 3.8.2 still apply to each column during adsorption and desorption. Equations 3.16, 3.14, 3.15 and 3.13 describe them respectively.
The created model needs to solve these equations spatially (at each node/slice) for each time step, and then switch to desorption mode. Besides that, attention must be given to the second column so that it operates in either (adsorbing/desorbing) mode depending on the relative humidity feedback of the first column. A working schematic of the drying system is given in Figure 5.3. The flipping of the adsorption and desorption mode in the system, in the working prototype, is done by a 5-way solenoid valve.

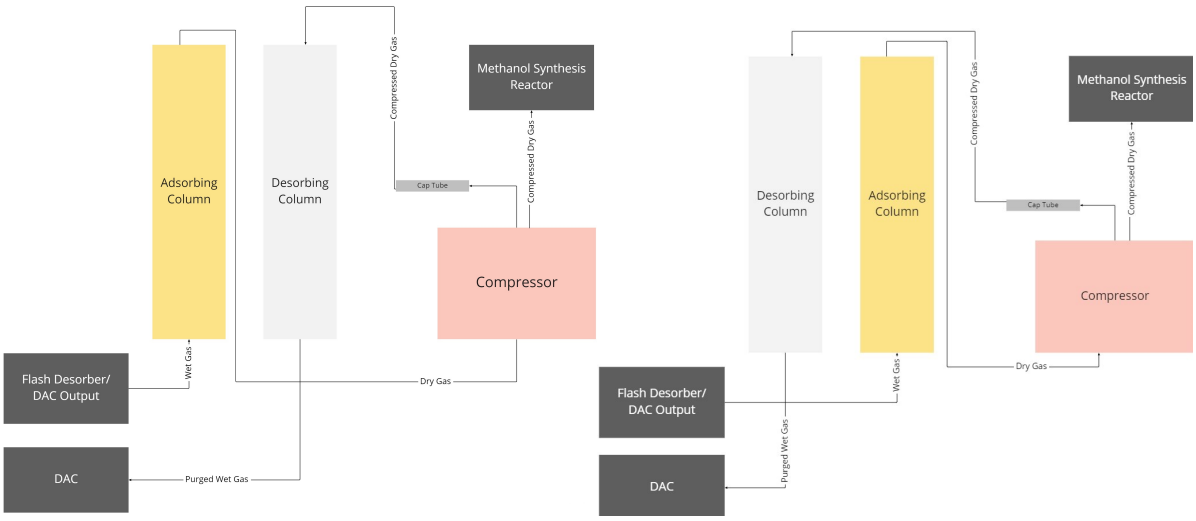

(a) Before breakthrough (b) After Breakthrough

Figure 5.3: Working Schematic of the Drying System

In Figure 5.3a, the left column is adsorbing and the right column is desorbing. When the left column functions as an adsorbing column, wet gas from the DAC downstream passes through the inlet. As the gas passes through the length of the packed bed, the adsorbent starts to dry the gas and the dry gas (RH=0) at the outlet is passed on to the compressor. Due to the heat generated during adsorption, the output gas has a higher temperature. After some time, the silica gel beads closer to the inlet become saturated and the inlet wet gas stays wet until it reaches the next layer of unsaturated silica gel beads. In this manner, the saturation shifts across the length of the drying column. When the last layer of silica gel beads (at the outlet) is saturated, the column is said to have reached 'breakthrough[3]' and the output gas is not dry anymore. At this point, the right column flips and starts acting as the adsorbing column. In the meantime, the right column needs to be regenerated and desorbed for the next cycle. This can be seen in Figure 5.3b. The band heaters around the desorbing column are

[3]Defined at RH=2%, here, as the required purity of the gas was 98%.

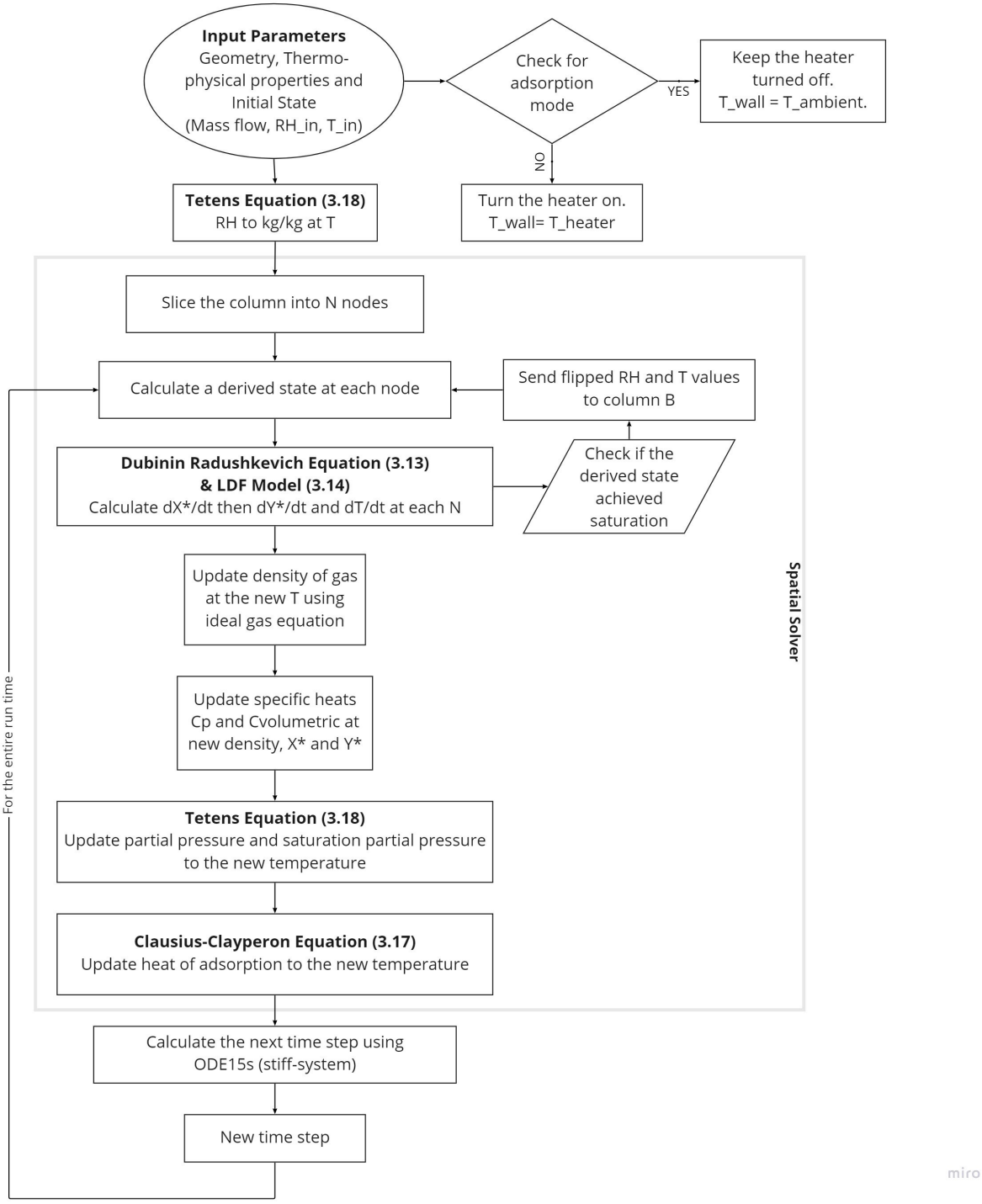

Figure 5.4: Algorithm of the drying system model

turned on to bring all the silica gel beads to the desorption temperature (120°C). The input gas for the desorption column is compressed, dry air coming from the compressor. This compressed gas purges through the packed bed and brings condensed water vapour to the outlet of the desorbing column, thus regenerating the silica beads for the coming cycles. A capillary tube is present between the compressor and the desorption column to control the mass flow rate that re-loops back into the drying system. This ensures that only a minimal amount of compressed gas is used for regeneration of the column- as the main purpose of the compressor is to provide the methanol synthesis reactor with compressed gas.

5.3.1. Implementation

An algorithm of the dynamic model which encompasses two columns that can run in adsorption and desorption (complete cycles) over a period of time is shown in Figure 5.4. The geometric properties like column dimensions, silica gel dimensions, void fraction are inputs. Thermo-physical properties like the overall mass transfer coefficient, axial diffusion coefficient, overall heat transfer coefficient, conductivity, bulk density of the silica gel and molar volume of the gas are gathered from literature and/or calculated using empirical relations mentioned in Section 4.4.1. The initial physical state (initial bed loading, pressure, temperature and mass flow at the inlet) is taken as an input.
After reading the input, the model checks if the column is adsorbing or desorbing, to decide if heating is required. Then the column is divided into N different segments with the boundary condition at the first segment being the initial physical state at the inlet, at the first time step. Taking this as the equilibrium state, the rate of change in concentrations of water vapour in solid ($\frac{dX^*}{dt}$) and gas ($\frac{dY^*}{dt}$) states along with the temperature ($\frac{dT}{dt}$) is calculated. At this point, the nature of increase or decrease in these derivatives is continuously checked by the solver. If there is a change in the sign of these derivatives, i.e., if the temperature suddenly stops increasing/decreasing, the solver detects breakthrough[4]. Then the columns are flipped for adsorption or desorption modes. If no change in sign is detected, the solver continues to update the properties required to calculate the equilibrium state of the next node. The gas properties (ρ, C_p and C_Σ) are updated depending on the new temperature and concentration. Using these values and the renewed partial pressure values, the new heat of adsorption is calculated. The solver calculates the next time step and the new equilibrium state is derived using the updated values[5]. This entire process continues for the duration of run time that is given.

5.3.2. Challenges during Implementation

During the design of the drying system model, the following key changes needed to be made to fulfill its goals.

Control Strategy for full cycle:
In order to mirror the real system, the half-cycle (adsorption or desorption) model needs to be converted not only into a full-cycle (adsorption and desorption) model but also inherently control when to flip between these half-cycles. The ODE15s solver was used to solve the set of discrete equations 3.19, 3.21 and 3.20 in the half-cycle model. This is a stiff-system solver and is used due to a large differences in the time-scales inside the system- the time-scales being the residence time of the gas inside the packed bed (0.1 s/node), time-scale of transfer phenomena and the total time of simulation (8 h) [1]. In addition to that, the constant changes in nature[6] of the derivatives alternate between positive and negative values- which could lead to numerical instabilities[7] and would need smaller time-steps to be stable. In order to reduce the computational time of a stiff-system, the solver chooses a variable-step size method. To add the aforementioned control strategy, the solver settings need to be changed. Besides changing the error tolerances and reducing the maximum step-size for more accuracy, the new solver settings use a different technique to consistently check for breakthrough. As discussed in the previous Section 5.3.1, the model flips modes when saturation is detected via a change in the sign of one of the derivatives. This is done by 'resetting' the solver externally when such a change is detected. The external reset is connected to a flipped state of the previous half-cycle (say, adsorption), which will be the new input for the coming half-cycle (say, desorption). The solver settings used in the previous model and the new model are given in Table 5.1.

Control Strategy for System Integration: The integration of the drying system does not encompass just the two packed bed drying columns, but also the compressor. In order to integrate these models, the 'interacting parameters' are identified as follows:

- Mass flow into the compressor ($\dot{m}$) dictates the driving mass flow into the adsorbing column of

[4] By an 'external reset' model setting.
[5] Information about how the solver calculates the next time-step and other solver settings are given in the next section 5.3.2
[6] Increasing or decreasing
[7] Especially when the columns are to be flipped from adsorbing/desorbing modes.

Table 5.1: Solver Settings

Solver Setting	Option	Previous Model	New Model
Time Step Size	Maximum Step Size	5.00E+00	2
Solver Output	Non-negative	All (3*N)	External Reset
Error Control	Absolute Tolerance	1.00E-05	Auto
Error Control	Relative Tolerance	Auto	1.00E-04

the drying system.

- Mass flow out of the compressor that then passes through a capillary tube ($\dot{m_{cap}}$), drives the input flow into the desorbing column.
- The re-loop flow from the capillary tube also influences the pressure and temperature at the inlet of the desorbing column.

Once these parameters are identified, the compressor model[8] mass-flows can be connected to the drying system mass-flows. As for the control strategy for uninterrupted operation, the model essentially needs to simulate the five-way solenoid valve present in the prototype. Therefore, in addition to both the drying columns flipping between adsorption and desorption cycles, they also need to feedback each other when this flip occurs. Moreover, when this shift happens the mass-flows from the compressor also change accordingly, as illustrated in the working schematic, Figure 5.3.

System Integration Effects:
Due to the dynamic nature of both the compressor and the drying system model and the continuous renewal of these interacting parameters, the computational time of the model is hypothesised to slow down. When tested after integration, this does prove to be the case. However, this only spans over the time that the compressor achieves the desired outlet pressure and the maximum of this time-scale is about 300 s. After the first 300 s, the mass flow input is almost constant. This is a negligible amount compared to the run time (8 hours) of the drying system model and therefore the dynamic effects of integrating the compressor model are uninteresting. This is the most important reason for the compressor model to follow a black-box approach[9]. The most interesting dynamic behaviour of the entire system thus depends on the drying system cycles over the runtime of the ZEF plant. The cycle capacity (amount of air that can be dried in one cycle) and cycle times (amount of time taken for regeneration vs amount of time taken for adsorption) thus become the key parameters for the continuous operation of the system and especially for the sustenance of the compressor downstream.

5.4. Results and Discussion

In this section, the results of a typical run of the model are illustrated and their behaviour is discussed. Figure 5.5 shows the Temperature (°C) of all the nodes of one of the columns (A), given by the model, during a 36 hour run. The inlet RH was 100%, and temperature was 20°C. The heater temperature was 120°C, ambient temperature was 20°C and re-loop temperature(from the compressor) was 70°C. The flip time for breakthrough was 5 hours.

Here, each cycle constitutes adsorption and desorption. It can be observed (in Figure 5.6) that there are three modes of operation in each cycle, that can be distinguished by the rise and fall of the temperature curves:

1. Adsorption (in yellow)
2. Desorption with the heater turned on (in red)
3. Desorption with the heater turned off (in grey)

[8] Described in detail in the next chapter 6.
[9] Also elaborated in Chapter 6

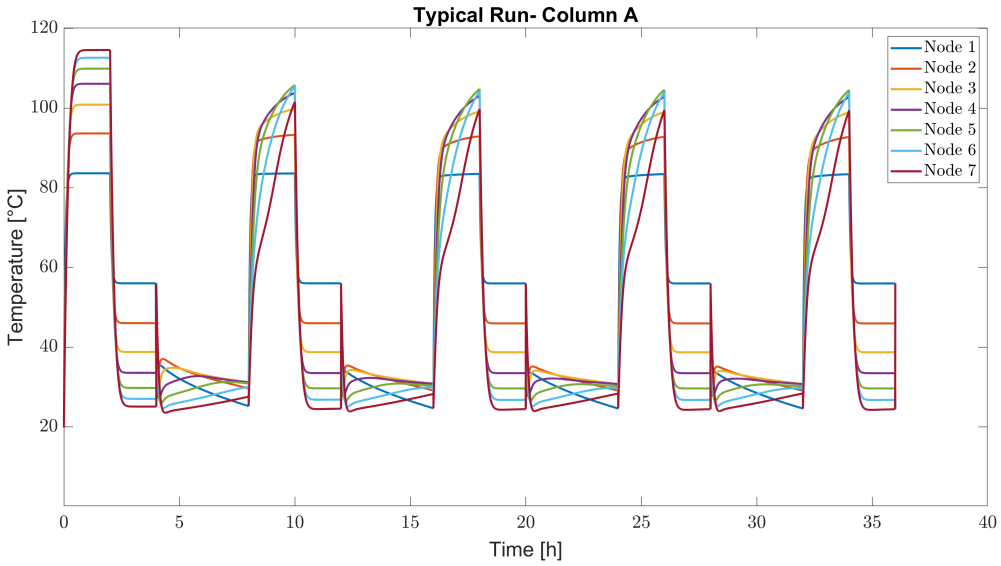

Figure 5.5: Temperature of all nodes given by 36 hour run at
L=0.3m, RH_{in} = 100%, T_{in}= 20°C, T_{heater}=120°C, $T_{re\text{-}loop}$=70°C and $T_{ambient}$=20°C

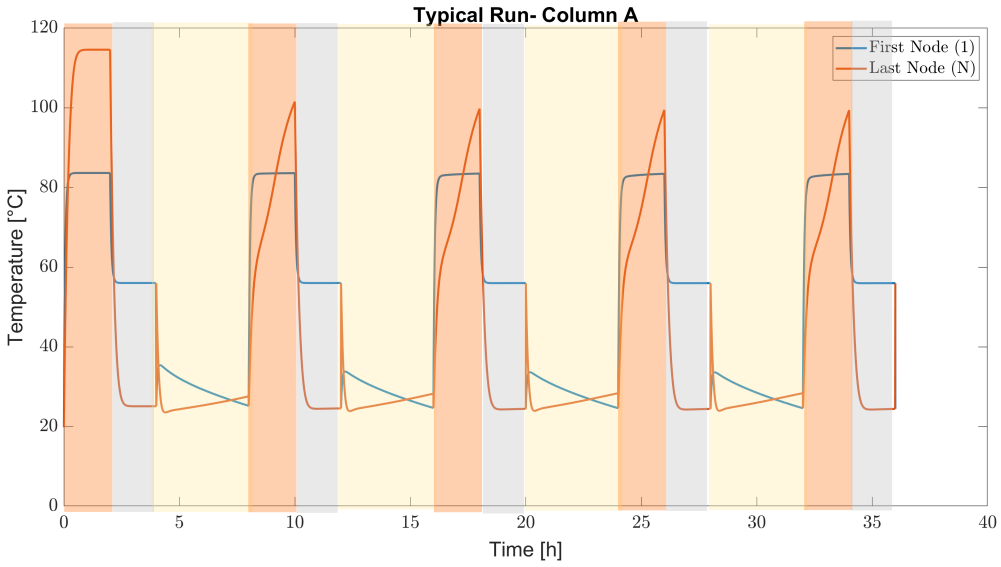

Figure 5.6: Temperature of the first and last nodes given by 36 hour run at
L=0.3m, RH_{in} = 100%, T_{in}= 20°C, T_{heater}=120°C, $T_{re\text{-}loop}$=70°C and $T_{ambient}$=20°C, where
Red- Desorption mode with heating, Grey- Desorption Mode without heating and Yellow- Adsorption mode

To see clearly what is happening at the inlet and outlet of the column, Figures 5.6 and 5.7 show the temperature curves and water content in the gaseous phase at the initial and final nodes, respectively. Figures 5.8 and 5.9 show the distinguished modes of operation.

5.4.1. Desorption Mode

Temperature

For the illustrated column (A), the desorption cycles consist of two modes- with the heater turned on for half of the desorption cycle length, in order to activate the desorption temperature. After this time, all the silica gel beads attain steady-state and maintain this desorption temperature for the rest of the cycle. Therefore, the heater is turned off for the other half of the desorption cycle, to reduce energy consumption.

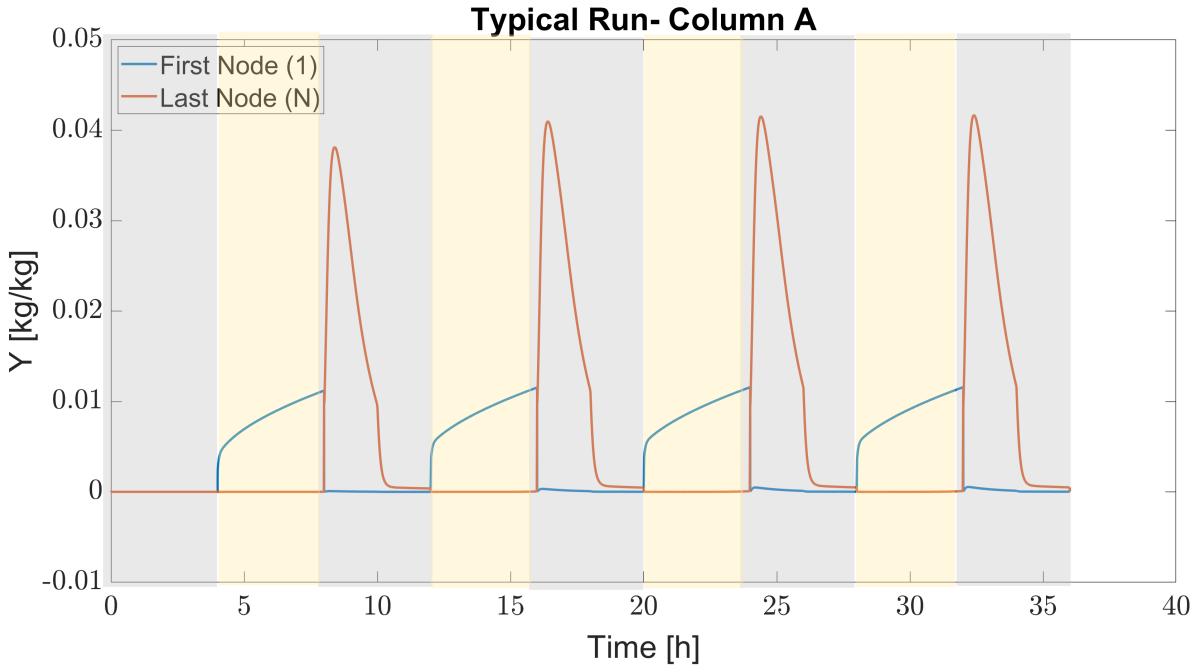

Figure 5.7: Water Content in Gas Phase of the first and last nodes given by 36 hour run at L=0.3m, RH_{in} = 100%, T_{in}= 20°C, T_{heater}=120°C, $T_{re\text{-}loop}$=70°C and $T_{ambient}$=20°C, where Grey- Desorption Mode and Yellow- Adsorption mode

This can be seen in Figure 5.8, where Figure 5.8a shows the column being heated to almost 120°C for the first 2.5 hours and then the heater is turned off, as seen in Figure 5.8b, and the temperature reduces until the column flips at 5 hours. This pattern continues for all the marked bands throughout the run time of thirty-six hours.
At the start of the desorption, the entire column is heated to 120°C and re-loop air from the compressor (at 70°C) enters through the top of the column, as shown in the schematic of Figure 5.8c. Due to the temperature difference of the fluid and column at the top, the temperature at the top of the column (80°C) is lower than the temperature at the bottom of the column (120°C). Looking at the model results, it can be seen that the last (red) node depicts the bottom of the column and the first node (blue) depicts the top of the column.
After the heater is turned off, the column temperature at the bottom falls to the ambient temperature, whereas the top temperature is higher at 70°C, as it comes from the compressor outlet. Therefore, from 2.5 to 5 hours, the temperature of the top (first node in blue) is higher than that of the bottom (last node in red).
As desorption is an endothermic process and the flow is from the top to bottom, the temperature decreases downwards, with each node, along the length of the column. This decrease is apparent when the heater is turned on, where the bottom nodes are hotter than the top ones. However, while there is no heating, the bottom node becomes the hottest node (due to compressor output) and the top node becomes the coldest (due to low ambient temperatures) node. The cooling effect still remains but is reversed.
Another important observation to note is the shape of the temperature curve in all the desorption cycles. In the first cycle, the increase of temperature, of both nodes, is almost linear while heated. Then the temperature stagnates at the heater temperature, and eventually decreases after the heater is turned off. However, this is not the case for the remaining cycles. The remaining cycles observe a linear increase, followed by an exponential increase, which becomes linear again with a reduced slope. The discrepancy in shape can be explained by the amount of water content inside the silica gel beads. Column A starts with a desorption cycle because the other column is then adsorbing. However, at the start of the run time (at Time= 0h), the desiccant is dry and therefore has no water content. The temperature increases linearly because it simply follows the temperature profile of the heaters. But after the first cycle, the desiccant adsorbs water from the fluid, and therefore has a significant amount

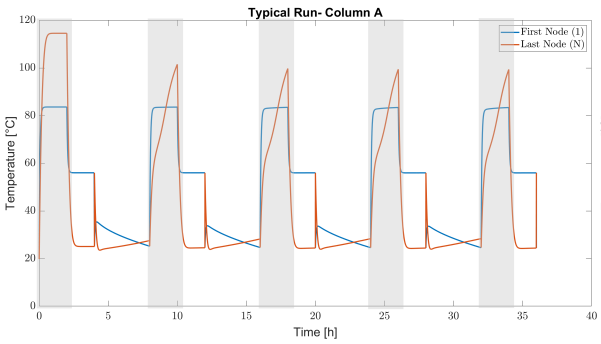

(a) Model-Heater On

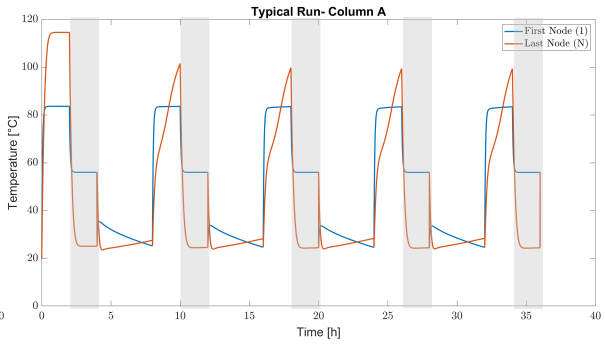

(b) Model-Heater Off

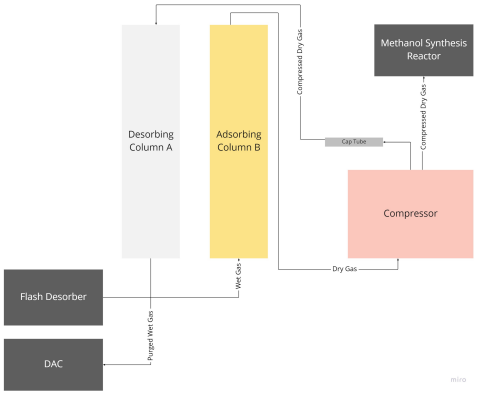

(c) Schematic

Figure 5.8: Desorption Mode

of water content. The exponential increase is caused due to the latent heat produced from the phase change of water when the temperature reaches the desorption temperature (70°C). This is only seen by the bottom (red) node due to the flow direction being downwards. In Figure 5.5, it can be noticed that the change in shape starts is more pronounced in the bottom nodes rather than the top ones.

Water Content in the Gas Phase

Furthermore, the water content in gas phase, seen in Figure 5.7, increases with time at the bottom of the column. This is because of the desorption and purging of water towards the bottom from the silica beads by the re-loop flow. The water content at the top, however, increases for the first few minutes until this node section is completely dry and then remains constant. In the figure, this can be seen by the profile of the first node (top) being almost constant, except for the first few minutes. It is also noticeable that there is an increase in water content with each cycle, and thus an increase in the time for which it needs to be fully dried[10]. The last node's (bottom) profile increases sharply at the start and then decreases rapidly- implying that the column is fully dried before the flipping time provided. This is very desirable for the system as the design is based on the assumption that the time taken to regenerate the column is much lower than that taken for adsorption.
As mentioned before, this column starts with desorption mode and thus with dry gas. Therefore, it is inherent that the water content in the gas phase is zero for both top and bottom sections for the first five hours during desorption.

5.4.2. Adsorption Mode

[10]More discussion on this cyclic capacity is presented in Section 4.1.

Temperature

After the column is satisfactorily regenerated, (5 hours, here) the column shifts to adsorption mode. As explained in Section 5.3.1, the model replicates this by 'flipping' (column-wise) the statespace. Consequentially, the inlet state now becomes the bottom, the outlet state becomes the top and vice versa. In Figure 5.9, this can be seen by the first node (blue) which previously represented the top, now becomes the bottom of the column. In either case, it is still the inlet, as can be seen in the schematic shown in Figure 5.9b.

Adsorption is an exothermic process and the flow is from the bottom towards the top. Hence, at

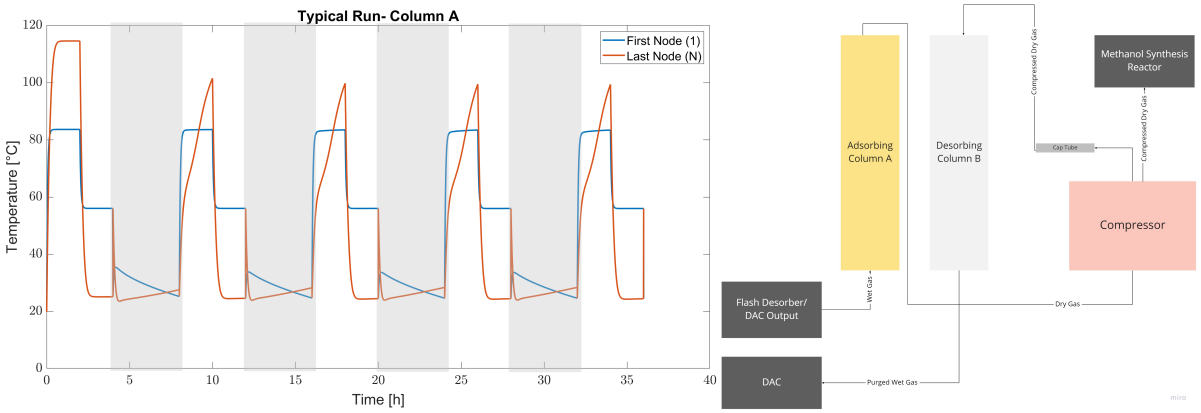

(a) Model (b) Schematic

Figure 5.9: Adsorption Mode

the start of the adsorption cycle (Time= 5 h), the temperature at the bottom is higher than that of the top. After some time, the desiccant at the bottom node saturates and does not produce more heat. Therefore, the temperature of the bottom node starts to decrease with time. Then the beads in the next node start to generate heat until they saturate as well and this goes on until the top node is saturated, and the column attains breakthrough. This leads to the temperature of the bottom to increase with time. The gradual shift in saturation of the beads along the column, upwards, can be seen more clearly in Figure 5.5, as the rise in temperature of the top nodes (5-green, 6-cyan and 7-maroon) can be seen with time. The peaks in temperature fall down due to the heat loss to ambient and convective flow upwards. However, at the bottom, the second node's (red) peak temperature is higher than that of the first one (blue), exactly at the start of the fall of the first node. This is because even as the first node beads stop producing heat after they saturate, they do not cool down immediately- thus adding to the temperature of the next node.

Water Content in the Gas Phase

The water content in the gas phase at the top of the column should always be zero, to ensure that only dry gas enters the compressor downstream. Therefore, the flipping time is decided by when the water content of this node section is not zero anymore. From Figure 5.7, it can be seen that the last node (top) in red always has no water content. In the mean time, the first node (bottom) has a constant influx of wet gas and therefore increases in water content over time. Nevertheless, at the start of each adsorption cycle, the water content in the gas phase at the bottom does not increase as steeply until the desiccant is saturated in this section.

5.5. Experimental Setup

The experimental setup of the drying system is connected to the compressor as shown in Figure 5.3. The flipping of the columns is controlled by a 5-way solenoid valve, that switches the inlet and outlet flows coming from the compressor into the drying system.

In order to measure the process parameters, each drying system column is equipped with Temperature

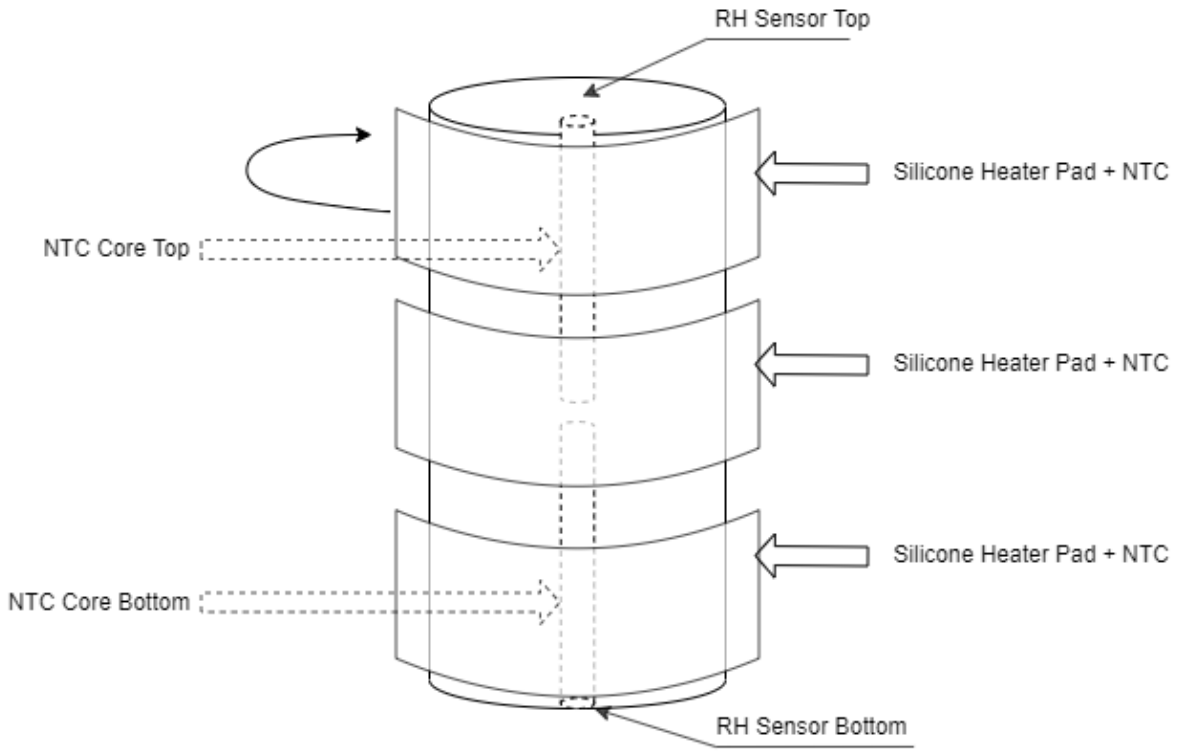

Figure 5.10: Experimental Setup of a Drying Column

(NTC) and Relative Humidity (RH) sensors. Three silicone pad type heaters[11], circumscribing the column on the outside, are used to heat up and thus regenerate the desiccant columns. The temperature generated by these heaters is monitored, by using NTCs attached in the middle of these heaters, as shown in Figure 5.10. The power input to them is controlled by a PID controller so that the temperature is maintained at that point until another input command is provided. To measure the core temperature of the packed bed, the NTCs inside the previously used rod-heaters[12] are used. As shown in Figure 5.10, these core-temperature measurements are not taken exactly at the inlet and the outlet, but somewhere at one-third length of the column at the top and bottom. However, the Relative Humidity (RH) sensors are located just outside the inlet and outlet of the column, as shown in the Figure.

5.5.1. Challenges

The goal of the experimental plan was to collect data of the process parameters that could be compared against the model data to validate the latter. As this is the first fully-integrated prototype of the FM subsystem, there are still optimisations that needed to take place, especially with regard to the measurement equipment.
In order to have a fair comparison of the model results and the experimental results, the following challenges needed to be circumvented:

Location of the NTC Sensors

As discussed in Section 5.5, the exact location of the core-temperature measurement is not known. This is due to the entire rod heater (which is about 10cm long) doubling as the NTC at the core of the packed bed, which gives a mean temperature reading. Although they are illustrated as the top and bottom measurements in the experimental data (in the coming sections), it must be noted that the actual values correspond to the sections that are a bit below and above the column's inlet and outlet.

[11] The design choice is explained in Section 5.2.
[12] Also in Section 5.2

Errors in the Relative Humidity Sensors

The most vital and peskiest challenge during experimentation was finding appropriate RH sensors that could give accurate data for the drying system requirements. As the measurements needed to be done both during adsorption and desorption, the RH sensors must be capable of measuring values well above 98% and under 2% up to 0 %. The sensors currently in use[13] have an error of $\pm 2\%$. This hinders the estimation of the system's drying capability during adsorption as the sensor data is unreliable below 2%. The exact desorption cycle time can also not be determined, as the sensors stop functioning when the water condensation occurs (RH =100%).

$$RH(\%) = \frac{P_{\text{water vapour}}}{P_{\text{saturation}}} \cdot 100$$
$$RH_2 = RH_1 \cdot \frac{P_{\text{Compressor}}}{P_{\text{Drying System}}} \tag{5.1}$$

To overcome these errors, the RH was 'amplified' using the compressor pressure output. As the pressure of fluid at the compressor outlet is higher than that at the outlet of the drying system, the measured RH would also be higher. This increase is directly proportional to an increase in pressure as, by definition, relative humidity depends on the water vapour pressure (given by Equation 5.1). In addition to that, the saturation pressure is independent of pressure changes. By doing this, the RH value at the drying system outlet can be extrapolated and the adsorption or drying performance can be measured more accurately.

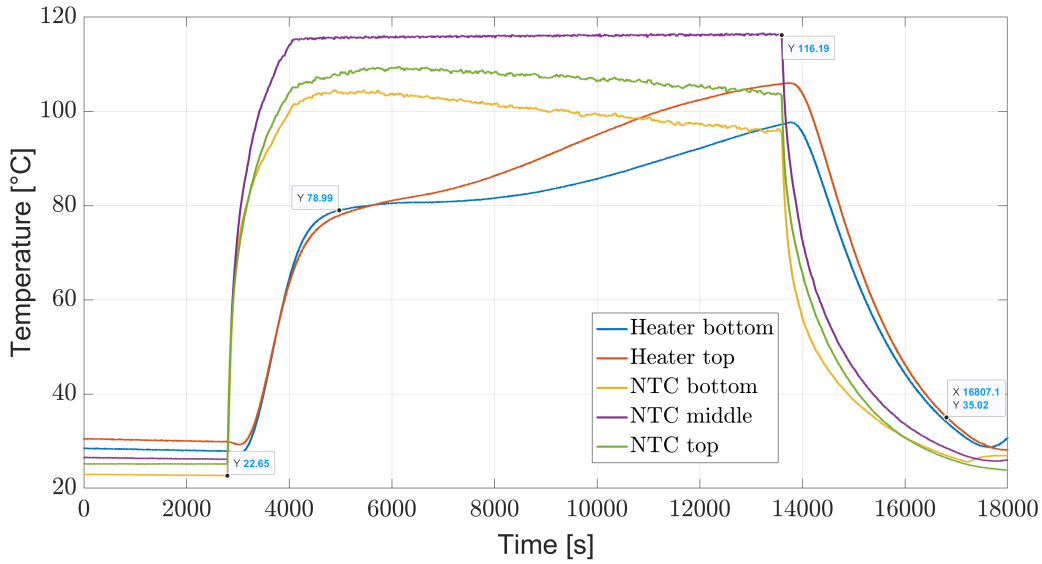

Figure 5.11: Experiment Data of the temperature profile of a desorbing column with heater turned on

Although the RH sensors start malfunctioning after observing some condensation on them, during desorption, the exact time of condensation can be seen clearly in the temperature curves. When the desiccant bed is dry and is heated, the column follows the profile of the heater, whereas wet silica gel beads show resistance to the temperature rise. When condensation occurs, latent heat is produced resulting in a 'kink' in the temperature profile, as can be seen in Figure 5.11, around desorption temperature (80°C).

This effect is also noticeable in the temperature profile results of the model, illustrated in Figures 5.5 and 5.6.

[13] Honeywell HIH8121 Type Sensors- Data Sheet can be found in Appendix B.

5.6. Validation

Bearing the shortcomings of the experimental setup in mind, a comparison is made between the experimental and model results so as to validate the latter. In particular, the temperature data is discussed in detail, as it was the most reliable dataset.

Experiment with L=0.3m and Real-Time Conditions

The first iteration of the experimental setup contained two cylindrical drying columns of 0.3m in length and 0.036m in diameter[14]. An experiment was run with the integrated prototype to simulate ZEF's real-time conditions[15]. In these conditions, the output from the direct air capture unit gives CO_2 at 40°C, 1 bar with 100% humidity. This meant heating the input gas from direct air capture downstream (CO_2) to 40°C and the columns to maintain an ambient temperature of 30°C. As the working fluid in the setup is air[16], and the KPI of the system is cyclic capacity- the water content of real-time situations were simulated, instead of the exact temperatures. At the DAC output, the amount of water vapour present is 27.7g per 1kg of CO_2 [1]. Therefore, air was heated to 33°C, using the flash desorber, so as to emulate the same water content that CO_2 has at the end of DAC output [61],[31]. The silicone pad heaters around the column were turned on during adsorption to maintain the columns at 30°C and when flipped increased their heating power to 120°C for desorption purposes. The compressor downstream was running at a pressure capped at 3 bars at 4000rpm frequency.

In the model, the mass flow input was calculated using the compressor input parameters and the compressor model[17]. The gas input temperature was also set to 33°C, the ambient temperature was set to 30°C and the heater temperature after flipping was set to 120°C. The results of the experiment and the model that show the temperature profile at the first and last node are given by Figure 5.12.

The dashed lines in the plot show the experiment's results and the normal lines represent the results of the model. It can be observed that in both cases, the bottom temperature (blue) is higher than the top temperature (red) at the beginning of adsorption. As discussed in the previous sections, this is the typical behaviour of the setup, due to the heat release during adsorption of water onto the silica gel beads. The top temperature gradually increases and eventually, once the bottom beads are saturated, exceeds the bottom temperature. This is also typical of the system, as the saturation passes on upwards until the end of the column and the setup hits breakthrough. The breakthrough of the experimental setup can be seen as both the top and bottom temperatures start cooling down after 1.25 hours. When the desiccant is fully saturated and cannot dry the input gas any further, there is no longer any generation of heat inside the column. Meanwhile, the convective flow upwards quickly cools the column down after breakthrough. In contrast to this, the model sees a 'flip' at 1.25 hours when the blue and red lines interchange- implying a flip in the statespace- where the first node now becomes the top and the last node becomes the bottom. The model notices the breakthrough, as it also monitors the relative humidity values and shifts to desorption mode which can be seen after 1.25 hours.

The relative humidity profile for the duration of the experiment and the model, at the outlet (top) of the column, are shown in Figure 5.13. The three dashed lines (blue, green and red) represent the sensor data from the experiments. At the time of this experiment, three RH sensors (of the same kind) were placed just outside the top for precise measurements. Evident from the figure, the unreliable RH sensors, especially at the low RH levels, show varying values albeit within their error range. Nevertheless, they all follow the same trend of increase in relative humidity and thus the water content at the top with time, again as expected. The column hits breakthrough at 1.25 hours, when the air has 1% RH and the experiment is then shut down in order to avoid any damage to the compressor downstream. The model flips, as can be seen by the model in blue normal line, and eventually goes to 100% for desorption mode, if the run time was a bit longer.

Overall, it can be seen that the model closely predicts the behaviour of the desiccant qualitatively. Especially considering that the primary goal of the system is to send dry air to the compressor, thus focusing on the RH and breakthrough times. However, quantitatively, there are discrepancies in the predictions of the model when compared to the experiment.

[14] More details on the experimental setup are illustrated in Appendix A.
[15] (Sahara) Desert Conditions.
[16] Choice explained in Section 4.5.2.
[17] Explained in more detail in Chapter 6.

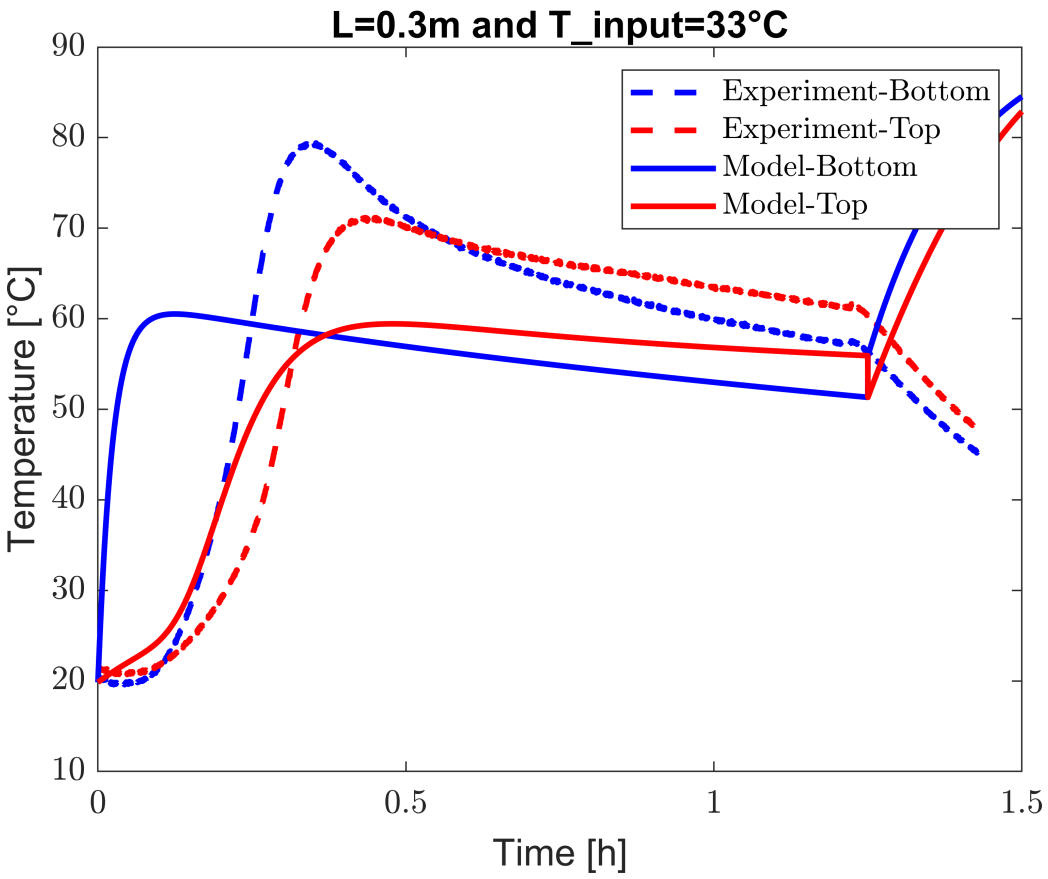

Figure 5.12: Temperature Profile at the top and bottom nodes of the experiment and the model, when T_{in}=33°C, $T_{ambient}$=30°C and L=0.3m

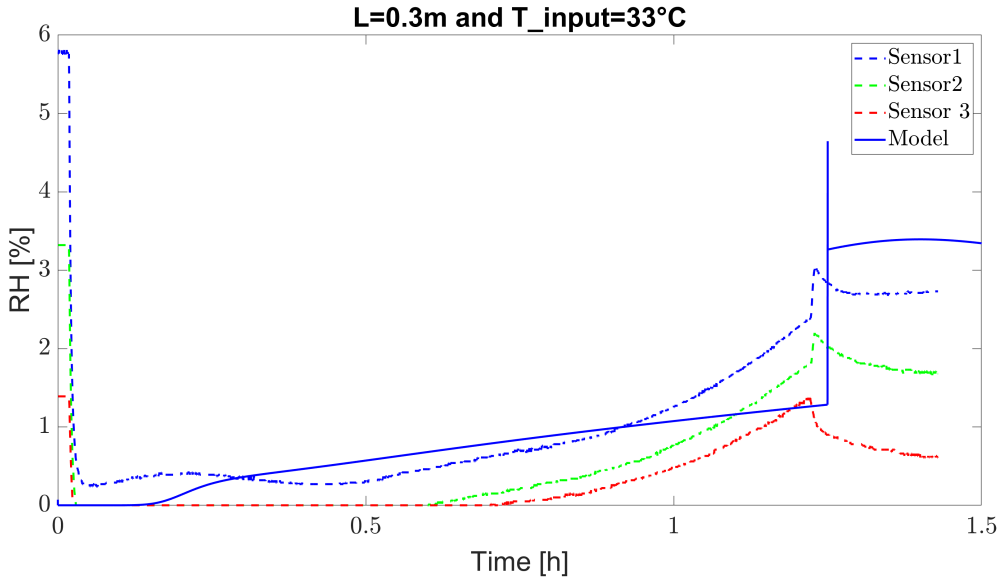

Figure 5.13: RH Profile at the top and bottom nodes of the experiment and the model, when T_{in}=33°C, $T_{ambient}$=30°C and L=0.3m

5.6.1. Discrepancies in the model and experiment data

The key differences in this scenario are:

- The magnitude of peak temperatures in both nodes
- The time taken to reach peak temperature in both nodes
- The difference between the peak temperatures of both nodes (T_{bottom}-T_{top})
- The shape (rate of decrease in the temperature) after the peak temperature has been reached
- The shape (rate of increase in the temperature) of the bottom node at the beginning

There are three broad possibilities owing to the aforementioned discrepancies- change in heat or mass transfer properties, or a combination of both. To understand specifically why these discrepancies arise, the energy and mass equations used in the model are broken down and studied further. For instance, the energy equation (Equation 5.2) is made up of four different paths of heat transfer due to conduction, convection, adsorption and ambient. Whereas the mass transfer comprises three different sources- diffusion, convection and adsorption as shown in Equation 5.3. Equation 5.4 also shows mass transfer that is caused due to the LDF model.

$$\frac{\partial T}{\partial t} = \underbrace{\frac{k_e}{c_\Sigma}\frac{\partial^2 T}{\partial z^2}}_{Conduction} - \underbrace{\frac{J_i c_{p_g}}{c_\Sigma}\frac{\partial T_w}{\partial z}}_{Convection} + \underbrace{\frac{\rho_b \Delta H_w}{c_\Sigma}\frac{\partial X_w}{\partial t}}_{Adsorption} - \underbrace{\frac{4k_w}{Dc_\Sigma}(T - T_\infty)}_{Ambient\ Losses} \tag{5.2}$$

$$\frac{\partial Y_w}{\partial t} = \overbrace{D_l \frac{\partial^2 Y_w}{\partial z^2}}^{Diffusion} - \overbrace{\frac{J_i}{\epsilon \rho_i}\frac{\partial Y_w}{\partial z}}^{Convection} - \overbrace{\frac{\rho_b}{\epsilon \rho_i}\frac{\partial X_w}{\partial t}}^{Adsorption} \tag{5.3}$$

$$\frac{\partial X_w}{\partial t} = K_w\,(X_w^* - X_w) \tag{5.4}$$

Each of these paths are dependent on their respective coefficients of transfer as follows:

1. **Heat transfer**

   - **Conduction**: Depends on the thermal conductivity of the adsorbent bed (k_e) and overall volumetric heat capacity (c_σ). The thermal conductivity of the adsorbent bed was taken to be 0.2[18] W/mK taken from literature sources. The overall volumetric heat capacity is obtained by a summation of proportions of the heat capacities of the fluid (air), gas (water vapour), liquid (water) and the solid desiccant (silica gel) as shown in Equations 5.5 and 5.6. These equations are updated with each time-step, correcting to the new Y_w, X_w and ρ_i[19] values.

$$c_{p_g} = (c_{p_i} + Y_w c_{p_{w,g}}) \tag{5.5}$$

$$c_\Sigma = \rho_b(c_{p_s} + X_w c_{p_{w,l}}) + \epsilon \rho_i c_{p_i} \tag{5.6}$$

     As the c_σ values are evaluated for each time step, there is little scope to change this parameter directly. The only way to check for discrepancies caused by this would be to re-check the validity of all the heat capacity and density values used in the equations above. The assumption that an ideal gas mixture is used to calculate the density could also be a factor. However, the value of k_e is derived from correlations from literature. Other models with similar conditions of working fluid (air), desiccant particle diameter to tube diameter ratio and porosity give values within the range of 0.131 to 0.261 W/mK- with 0.131 W/mK given by the Maxwell model [62], 0.211 W/mK given by Zehner/Bauer model [63], [64] and 0.261 W/mK given by the Krischer model [65]. Figure 5.14 shows the influence of this conductivity range. Evidently, the influence of the conductivity in this range is negligible- mostly due to the small variation 0.13W/mK.

[18] Explained in Section 4.4.1.
[19] Calculated from the Ideal Gas Law using the new temperature T of the current time-step.

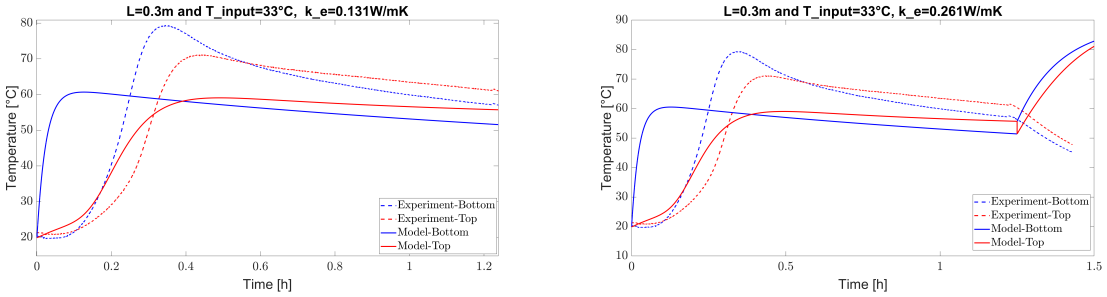

(a) k_e=0.131W/mK (b) k_e=0.261W/mK

Figure 5.14: Temperature profile of first and last nodes with varying conductivities, when T_{in}=33°C, $T_{ambient}$=30°C and L=0.3m

- **Convection:** This mode depends on the mass flux density (J_i), void fraction (ϵ), specific heat capacity of the gas phase (c_{pg} and overall volumetric heat capacity (c_σ). Void fraction depends on the packaging of the packed bed (which is known) and the heat capacities, as indicated earlier, are already given properties for air. The mass flux density, however, depends on mass flow- which is given by the compressor model, and the area of the bed (which is known). Therefore, the most likely factor that could be a source of discrepancy, owing to convection, could be the mass flow input dictated by the compressor model. However, the compressor model, discussed in the next chapter (6), is an empirical one and has a maximum error of 80[20] g/h. This rate of mass flow could be influential in the time taken to reach peak temperatures. An increase in mass flow rate leads to a higher amount of water content that passes through the column per given unit time, causing faster saturation, resulting in the faster peaks seen in Figure 5.12. Another intuitive effect caused by an increase in mass flow rate is increased cooling due to convective flow, which leads to lower peak temperatures.
- **Adsorption:** Varies with the heat of adsorption (ΔH_w) which is calculated using the Clausius-Clayperon Equation given by 3.17 and the corresponding pressures by using the Tetens Equation 3.18. The main assumption here is also that the gas was ideal and therefore, a lower saturation pressure than reality. From the Clausius-Clayperon relationship, this lower pressure leads to a lower heat of adsorption. This would mean that it is plausible that this extra heat generated that the model does not take into account is the cause for lower temperature peaks of the top and bottom nodes.
- **Ambient Losses:** This can be varied by the overall heat transfer coefficient (k_w). The value taken from literature was found to be 8.34 W/m^{2}K. However, it is also seen as a common practice to fit this data to the experimental setup, as numerous studies have shown[21]. Figures 5.15 and 5.16 show the temperature profiles given by the model without any losses to ambient, to illustrate the effect of this mode.
  It can be seen that the temperature at the top goes much higher than the experimental values and also the previous run that includes ambient losses (Figure 5.15b). The effect is more prominent when all the peak temperatures of all the nodes are observed, as in Figure 5.16. Without any loss to the ambient, the peaks of temperatures increase along the length of the column. This is due to the build-up of heat generated due to adsorption and shift in saturated silica gel bead sections. On the other hand, the temperature peaks of the model run with losses to the ambient notice an increase until the third node and then a drop in peak temperatures until the end of the column. The decrease occurs due to the heat loss to ambient becomes increasingly significant starting from the middle of the column length. The occurrence of peaks, however, is later without any losses to the ambient, which is similar to that of the experiment. Therefore, the discrepancy in a 'faster' peak value could also be the reaction of an over-estimation of losses to ambient. This effect is clearly illustrated in Figure 5.15a when the losses to the ambient are almost halved (k_w=4.88W/mK) and the

[20] See Figure 6.6
[21] See Section 4.4.1

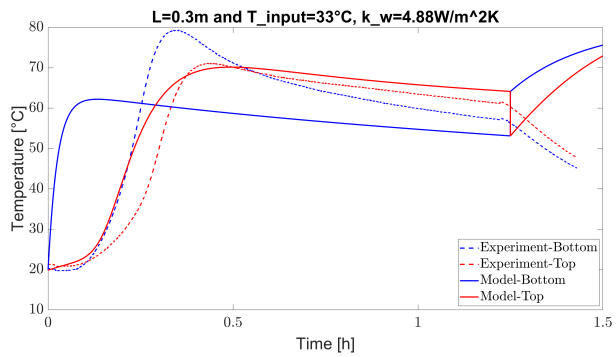

(a) With Losses to Ambient, k_w=4.88 W/m^{2}K

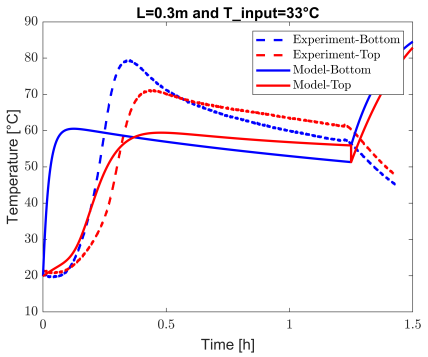

(b) With Losses to Ambient, k_w=8.31 W/m^{2}K

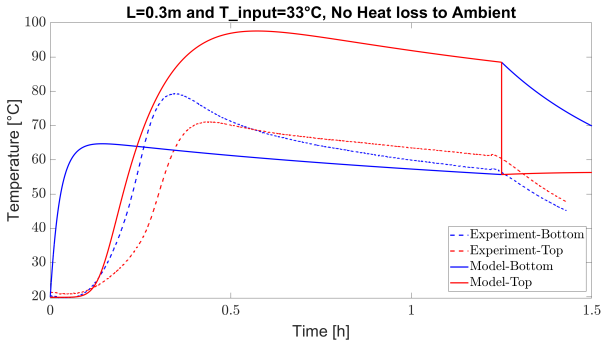

(c) Without Losses to Ambient

Figure 5.15: Temperature profile of first and last nodes with varying losses to the ambient, when T_{in}=33°C, $T_{ambient}$=30°C and L=0.3m

top node reaches its peak temperature value at a time stamp that is very similar to that of the experiment. The bottom node isn't affected because it is dominated by other modes of transfer, as seen in 5.16.

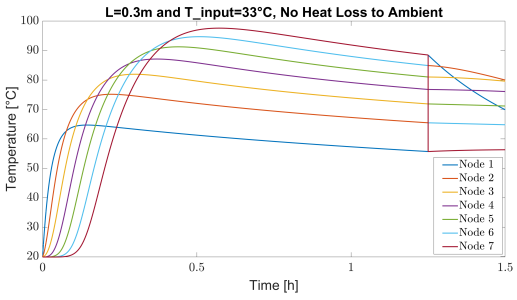

(a) Without Losses to Ambient

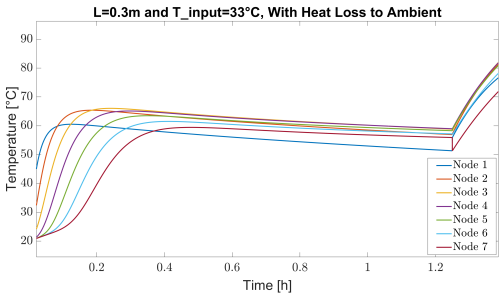

(b) With Losses to Ambient

Figure 5.16: Temperature profile of all nodes with varying losses to the ambient, when T_{in}=33°C, $T_{ambient}$=30°C and L=0.3m

2. **Mass transfer**

- **Diffusion:** This mode depends on the gas diffusion coefficient (D_l) which is derived from the Edwards-Richardson correlation. This correlation is chosen due to the range of Re and Pe numbers and pellet size (d_p)[22].
- **Convection:** This mode depends on the mass flux density (J_i) and density of the gas (ρ_i)-

[22] Other correlations for D_l can be found in Section4.4.1

which is a physical property of air. Therefore, the discrepancies caused by this are mainly because of the compressor model's error range.

- **Adsorption:** The density of the gas and bulk density of the solid (ρ_i and ρ_b) and epsilon (ϵ) cause fluctuations in this mode. All of these properties are well-known, therefore the difference in the temperature curves due to this mode is less likely.
- **Linear Driving Force:** The use of LDF model to describe the mass transfer is quite common where the rate of drying is not constant. The calculation of the mass transfer coefficient (K_w), however, varies from each work of literature as seen in Section 4.4.1. Previous works have shown a significant impact of the mass transfer coefficient on the temperature and Y_w profiles of the model [1]. This effect is further investigated by exaggerating the mass transfer coefficient and varying it considerably. The mass transfer coefficient used in the Figure 5.12 is 4.74*10^{-4}[-/s]. This value is altered by a factor of 1/10, 10 and 100. The results are shown in Figure 5.17.
  Clearly, increasing the mass transfer coefficient shows an increase in the peak temperatures

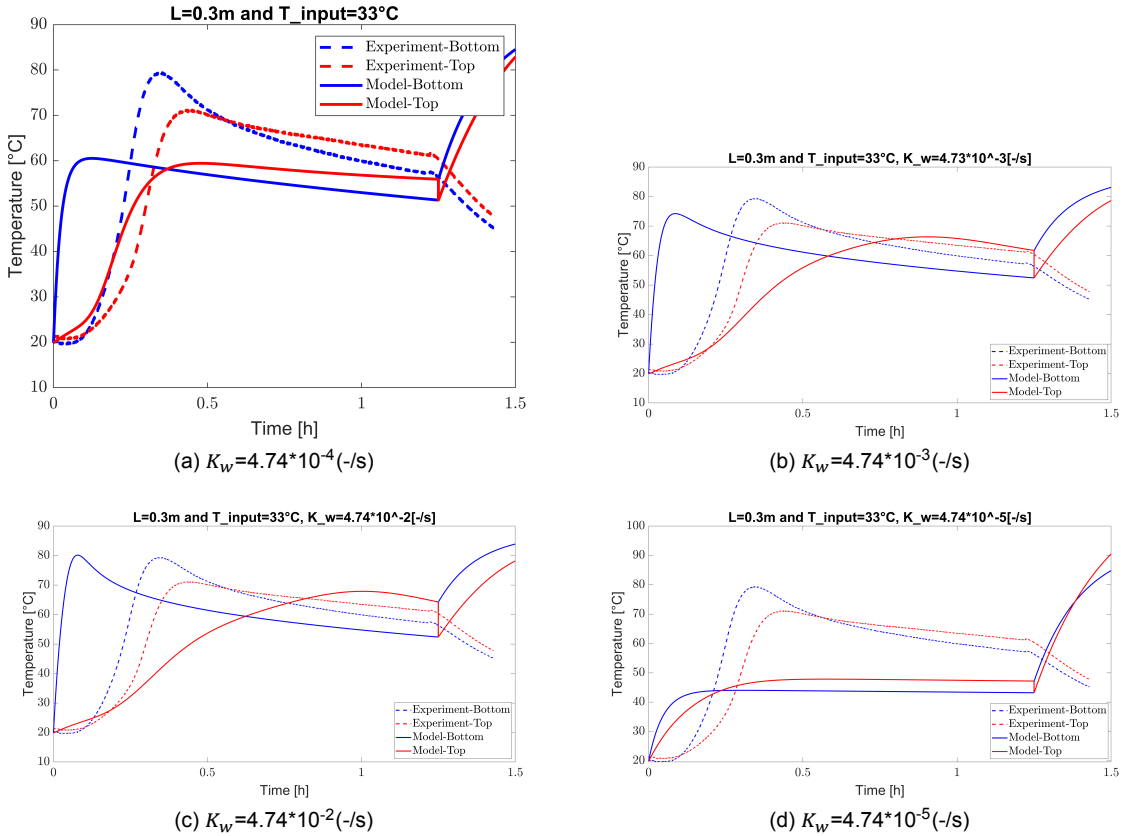

(a) K_w=4.74*10^{-4}(-/s) (b) K_w=4.74*10^{-3}(-/s)

(c) K_w=4.74*10^{-2}(-/s) (d) K_w=4.74*10^{-5}(-/s)

Figure 5.17: Temperature profile of first and last nodes with varying mass transfer coefficients, when T_{in}=33°C, $T_{ambient}$=30°C and L=0.3m

of both nodes. This is also the first parameter that has shown an increase in the peak of the bottom node temperature as well. The variation does seem to affect the time taken for the top node to reach peak temperature, as can be seen by the change in the shape of the top node curve. Since the temperature difference is expected not only due to underestimation of mass transfer, but also that of heat transfer, a factor increase of 10 is deemed appropriate to depict the bottom node temperature increase.

After investigating the heat and mass transfer coefficients, most of the dissimilarities enlisted above have been tended to- except for the difference between the peak temperatures (i.e, T_{bottom}-T_{top}) and the shape of the bottom node at the beginning of the experiment. To understand why this is the case,

some factors concerning the experimental setup[23] are scrutinised. The most important conclusion was found to be the deviation caused by the location of the temperature sensors. Since the exact location of the node that corresponds to the experimental data is unknown, different nodes from the model are plotted and compared in Figure 5.18. It is clear that nodes 3 and 5 show a similar temperature profile to that of the experimental data- where both the maximum peaks and the difference between them (T_{bottom}-T_{top}) are similar to the experimental data. As the column is 0.3m and there are 7 nodes, the sensor data, therefore, corresponds to the sections that are at a distance of 8.6cm to 12.9cm from the top and bottom of the column.

From the analysis above, all the fitted parameters are implemented in the model and the results are

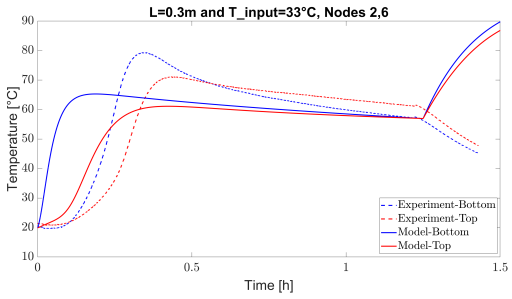

(a) Nodes 2 and 6

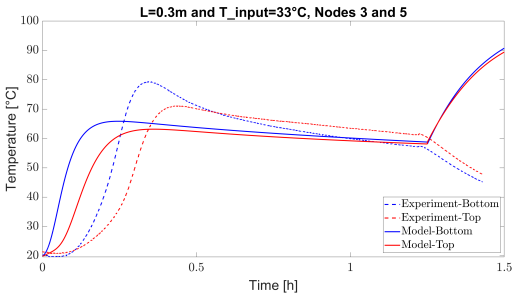

(b) Nodes 3 and 5

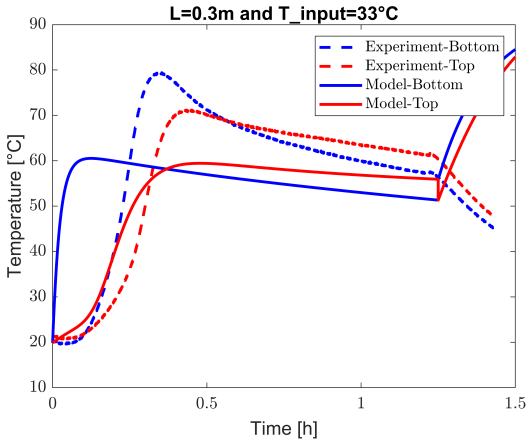

(c) Nodes 1 and 7

Figure 5.18: Temperature profile with varying location of nodes, when T_{in}=33°C, $T_{ambient}$=30°C and L=0.3m

shown in Figure 5.19a, whereas those of the previous parameters are shown in Figure 5.19b. Most of the deviations like the peak temperature magnitude and the difference between them, the time taken to reach the peak and the shape (rate of increase) of the bottom node profile have been corrected. The shape (rate of decrease) of the top node after the peak has been reached, however, still needs modifications[24].

5.7. Using the model as a design tool

After understanding the model responses to each parameter, it can be considered reliable to be used as a design tool. As seen in the previous section, the experiment performed and the model results show that the breakthrough time, in the desert/real-time conditions, is well under 1.5hours. This is highly undesirable for ZEF's operating conditions, as the total duration of operation would be 8 h/day. With such a short time for adsorption, the principal hypothesis that the drying time would be higher than the regeneration time would not be valid and the continuous operation of the entire system would not

[23] See Appendix A.
[24] Discussed further in Chapter7

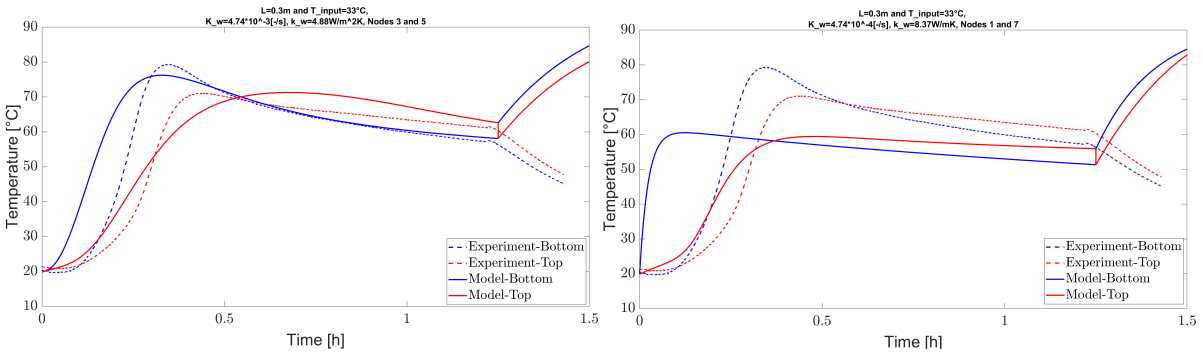

(a) Fitted Parameters (b) Previous Parameters

Figure 5.19: Temperature profile with fitted parameters, when T_{in}=33°C, $T_{ambient}$=30°C and L=0.3m

be possible.
To avoid the intermediate shut down of the system due to short breakthrough times, another system is designed with a column length that is double the size of the previous setup, with the new column length being 0.6m. This change is expected to prolong the adsorption time and strike a good balance with the time for desorption. All the other equipment within the experiment remained the same, except for the column length and intrinsically, the amount of silica gel beads that filled up the column. Although, the packing fraction (ϵ) still remains unchanged[25]. Results of the experiment showed in Figure 5.20 prove this hypothesis and the breakthrough time, in fact, increases by more than a factor of 2. A comparison is made between the previous parameters used and the fitted parameters from the analysis made in Section 5.6.1- to check the validity of the new parameters. The only exception is the node location because the estimated location found previously was in the range of 8.6-12.9cm. That would translate to either the first and last nodes or the second and sixth nodes when the column length is resized to 0.6m.

From Figure 5.20, it can be seen that the previous parameters suit this case better- with respect to the rate of saturation of the beads (rate of decrease, after the peak has been reached) in the column. As the cycle time is an important KPI, especially in this scenario of column sizing, the previous parameters are deemed more relevant. On the contrary, the fitted parameters predict the peak magnitude itself and the rate of increase, before the peak is reached, much better. Upon further inspection of the source, the disparity was found to be due to the change in the overall heat transfer coefficient. As the column is doubled, the overall heat transfer coefficient had to be modified back to 8.37W/m^2K from 4.88W/m^2K, depicted by 5.20b and 5.20c. Since the packaging (ϵ) remained the same (due to a proportional increase in the column size and the amount of silica gel beads), the mass transfer coefficient was kept at 4.74*10^{-3}[-/s]. This also helped retain the peak magnitude values and the rate of increase of the fitted parameter curves seen in 5.20a. Moreover, nodes 1 and 7 (shown in Figure 5.20c) depict the experimental data better and the sensor data, therefore, corresponds to 8.6cm.

5.8. Evaluating the KPIs

The KPIs provide a good basis to facilitate a fair comparison between different iterations of the drying columns. With the different ambient conditions, heating costs (operational expenditure) and setup costs (capital expenditure) in mind, the cyclic capacity (kg of H_2O adsorbed per cycle) and the cycle time (time taken to reach breakthrough), when breakthrough is defined at RH= 2%. Figures 5.21a and 5.21b show the variation of this cyclic capacity over time. It can be clearly seen that at the end of each cycle, the amount of water inside the bed increases, despite being run for the same amount of cycle time, with the same heating conditions. The water content at the start of each desorption cycle is also higher than the previous one, implying that the column does not regenerate fully each time. The water content in Figure 5.21a is naturally much higher than that of Figure 5.21b because of the inlet conditions[26] On

[25]The column volume and the amount of silica gel beads, thus the volume, are both doubled. The ratio remains the same.
[26]Air holds more water content at higher temperatures, as explained in Section 5.6.

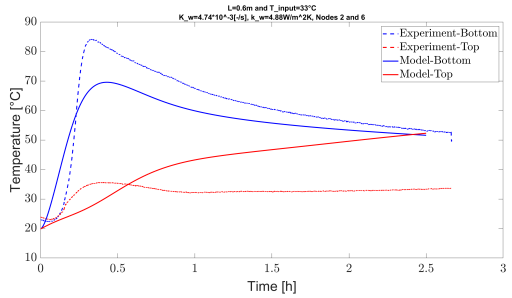

(a) Fitted Parameters

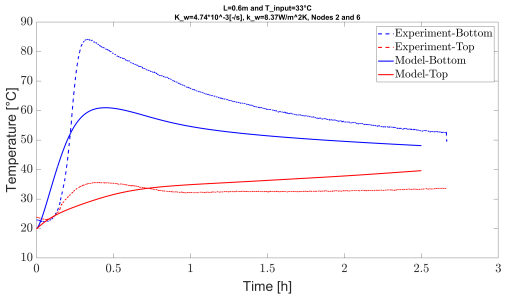

(b) Modified Heat Transfer Coefficient with Nodes 2 and 6

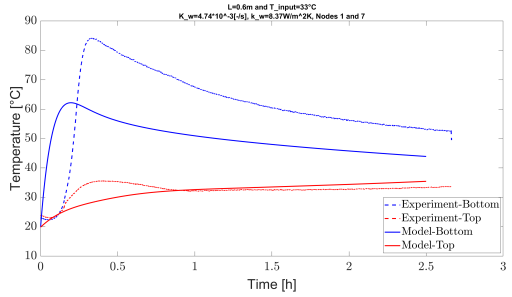

(c) Modified Heat Transfer Coefficient with Nodes 1 and 7

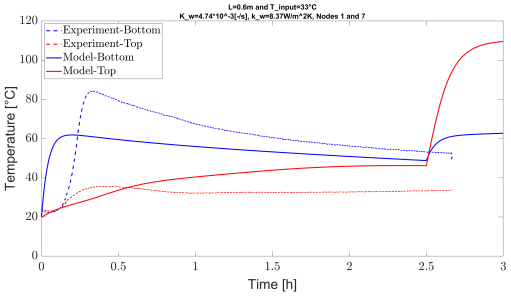

(d) Previous Parameters

Figure 5.20: Temperature profile when T_{in}=33°C, $T_{ambient}$=30°C and L=0.6m

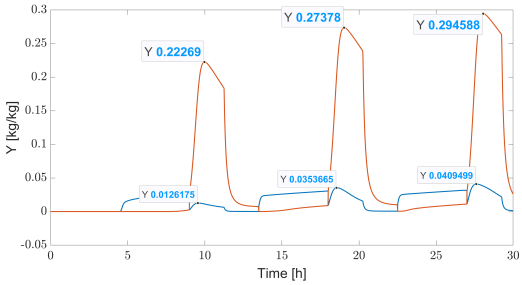

(a) L=0.6m, T_{in}=33°C and $T_{ambient}$=30°C

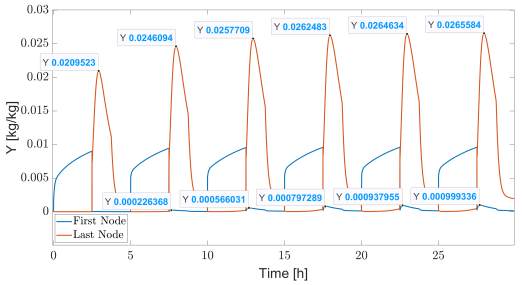

(b) L=0.3m, T_{in}=20°C and $T_{ambient}$=20°C

Figure 5.21: Variation in cyclic capacity over multiple cycles

the contrary, the cycle length of the former is much longer than that of the second, implying a different energy input per unit H_2O dried.

To conclude, the model can safely be used as a design tool[27] to predict the KPIs (cyclic capacity and cycle times) of the FM system when the set of extensive parameters is sized accordingly. The methodology to vary these parameters can be drawn from the sensitivity analysis performed above and from Sections 4.4.1 and 5.6.1.

[27] Supporting resources: [47] shows how to scale-up by keeping some ratios constant, using the breakthrough curves.

6

Compressor Model and Validation

In this chapter, the following topics will be elaborated:

- Goal of this model
- Selection of modelling method and how it works
- How to integrate this model with the drying system
- Experimentation- methods, results and discussion
- Validation

6.1. Goal of the Model

The compressor model design needs to consider that the goal of this entire project, as mentioned in section 2.1, is to provide a design tool that predicts the dynamics of the entire system. The characteristic time scale of these 'dynamics' could go up to the stipulated operation time (8hours/day) of ZEF or a bit higher. **The role of the compressor model is to identify the output parameters that change over time, quantify this variation and supply the drying system with feedback about the same.** This feedback ensures continuous operation of the drying system model, while simulating the fluctuations that happen within the compressor as well.

6.2. Selection of the Modelling Method

Following the approach mentioned in Chapter 4, all the relevant phenomena have been scrutinised over a characteristic time scale. Proceeding to devise the model, it is important to note the following:

- The process parameters of the compressor that interact with the drying system are the mass flows, pressures and the temperatures at the inlet and outlet.
- The characteristic time scales of the 'interacting' parameters of the compressor and the drying system.
- A steady state analysis of the modified rolling piston compressors used by ZEF has been previously performed (by [8]). Although this specific model does not reproduce the compressor performance to satisfaction, an adequate understanding of the thermodynamics has been established.
- The modifications done to the first stage compressor not only suffice the requirements of ZEF (8bars) but also ensure consistent performance. Therefore, most of the geometry of the existing compressor is deemed to prevail for a considerable amount of time in ZEF's iterative design process.

- At the time of this work, a design choice of having only two stages in the compressor train[1] is made- due to the reliability and consistency of the compressor performance, as was suggested by [8].

The most crucial point being the characteristic time scale comparison. From Figure 4.4, the only parameters that vary in the compressor in a comparable scale to the drying system are the pressure and temperature of the fluid, ambient temperature on convective heat coefficient of air, specific heats of the fluid and motor heat generation. These are investigated more in depth and a hypothesis is formed that the active cooling provided by a fan cools down the heat generated by the compressor (and motor), maintaining a low temperature gradient to the ambient- resulting in a uniform temperature of the motor and the casing. Therefore, the changes in thermo-physical properties caused by temperature variations can be neglected. More explanation on this is given in section 6.5. This leaves the pressure' and temperature variation of the fluid as the most interesting phenomena to be modelled.
There are multiple ways to model and measure these variations- one of which is to develop the governing equations mentioned in Chapter 3. This kind of a model is a 'mechanistic' or 'theoretical' model. A mechanistic model comprises all the physics and the parameters that exist in them. Although this kind of a model could provide one with opportunities to extrapolate data to a wide range of situations, it is extremely difficult to verify them. Moreover, designing a mechanistic model (as was the case with the Drying System in Chapter 5) involves conducting costly and time consuming experiments to unveil and measure the parameters involved. In most cases, a theoretical model gives an insight into the actual mechanism. However in the end, it does not give good results when applied to a specific real-life case [66]. In this particular scenario, such a mechanistic model that describes the geometric dimensions to maximum detail, is already in possession of ZEF, as mentioned above. What is necessary

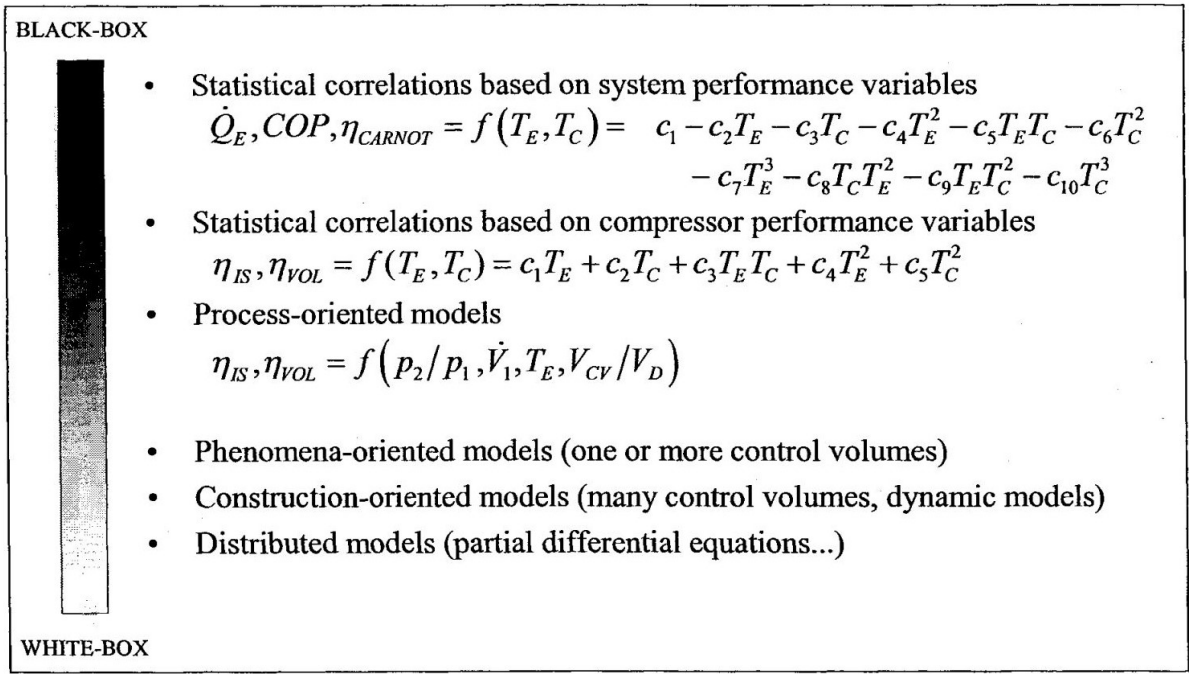

Figure 6.1: Categorisation of compressor models taken from [7]

is a model that gives accurate predictions of the 'interacting' parameters and how they change over time. **An 'empirical' or a 'statistical' model could be a perfect answer for the present needs.** An empirical model is designed with statistical correlations based on experimental data or from previous studies. They are easier to handle numerically even though they may incorporate some mechanistic assumptions. These models can be applied to other identical conditions, albeit a local (interpolation in between a range of observations) prediction instead of a global (outcome of all future experiments) one [67]. For instance, an empirical model for the first stage compressor could be partially modified to

[1] This implies a higher pressure ratio for the second stage compressor and therefore a higher temperature rise. The study of these effects is beyond the scope of this project.

emulate the higher stages, if they still use similar compressors.
According to a review of compressor models, the simplest compressor model is deemed to be a black-box (empirical) model which can relate the compressor performance (refrigerant mass flow rate and compressor electrical power) to operating conditions like the evaporating and condensing temperatures [7]. This review also distinguishes the variables that characterise the compressor performance- for the sake of this project, the 'energetic performance' variables are computed. As per the conclusions of [7], **compressor-oriented variable (polytropic efficiency) is chosen over a system-oriented variable (COP) to model the energetic performance more precisely.** An overview of the phenomena modelled ranging from a blackbox model to a graybox model is given in the Figure 6.1.
In order to formulate such an empirical model, a lot of data from experiments is required and will be discussed in Section 6.5.

6.3. Model Implementation

Following the modelling approach described in Chapter 4, the purpose (Section 6.1), system variables (Section 4.3), governing equations (Sections 3.4, 3.5 and 3.6) and relevant phenomena (Section 4.4) have already been identified. The following assumptions have been made for the sake of simplification:

- The working fluid is considered to exhibit ideal gas properties.
- The compression can be described by a polytropic process.

The workings of the simulation and its implementation in Simulink will now be described using the algorithm in Figure 6.2.
The model requires some geometrical dimensions (displacement volume and total volume), physical

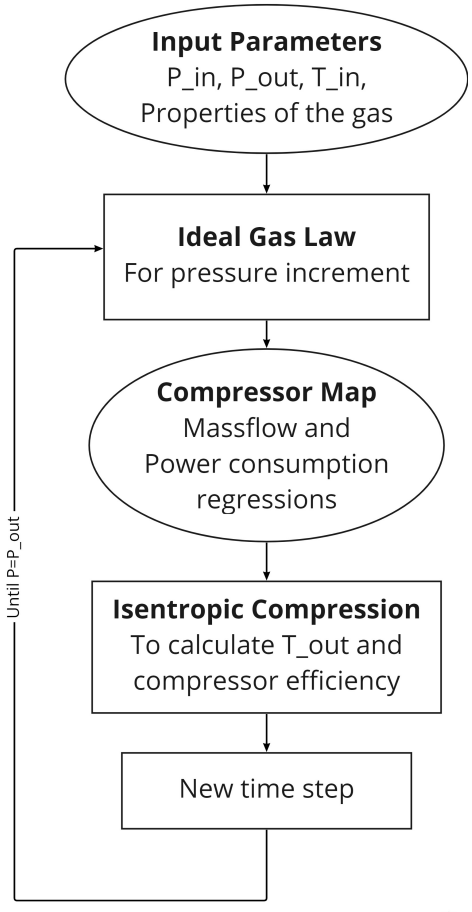

Figure 6.2: Algorithm that describes workings of the compressor model

state (pressure and temperature input) and thermo-physical properties (molar mass, density and heat capacity ratio of the fluid) as inputs. A compressor map that predicts the mass flow and power at each physical state point exists within the model. A mass flow rate for the current time step and physical state is calculated. As the time step increases, it uses the Ideal Gas law to calculate pressure increments and update the pressure values as in equation 6.1. The updated pressure values also lead to a change in the mass flow rate for the corresponding time step. The actual power consumed at each time step, for each state point is also calculated in a similar fashion. In the meantime, the model also calculates the isentropic efficiency of the compressor, again for each time step, by assuming a polytropic compression process shown by equation 6.2. With this information, the output temperature can be calculated 6.3. This process is repeated over time until a specified desired pressure output is reached. For the case of the first stage, this desired output would be 8[bars]. Details about how to obtain the compressor map and the polytropic coefficient n are reported in the subsequent Section 6.5.

$$\frac{dP}{dt} = \frac{dm}{dt}\frac{RT_1}{V} \tag{6.1}$$

here, m is the molar flow rate [mol/s] R is the ideal gas constant and V is the (constant) Volume occupied by the gas which is a summation of the displacement volume and buffer volume.

$$\eta = \frac{\dot{m}\frac{n}{n-1}RT\left(\left(\frac{p_2}{p_1}\right)^{\frac{n-1}{n}} - 1\right)}{P_{actual}} \tag{6.2}$$

here, $\dot{m}$ is the mass flow rate [kg/s].

$$\frac{T_2}{T_1} = \left(\frac{p_2}{p_1}\right)^{\frac{n-1}{n}} \tag{6.3}$$

An explanation of the compressor map and how it is made will be addressed in Section 6.5, along with the experimental data that was used for it.

6.4. System Integration Requirements

The ultimate goal of modelling the compressor system is to integrate it with the drying system and then investigate the effects. From the system schematic (shown in Figure 3.8) the following parameters dictate the thermodynamic state of the drying system

- Mass flow into the compressor ($\dot{m}$) dictates the driving mass flow into the adsorbing column of the drying system.
- Mass flow out of the compressor that then passes through a capillary tube ($\dot{m_{cap}}$), drives the input flow into the desorbing column.
- The re-loop flow from the capillary tube also influences the pressure and temperature at the inlet of the desorbing column.

6.4.1. Capillary Tube Model

A model of the capillary tube is then appended to the compressor model, to understand the phenomena inside it. A simplified algorithm for this is shown in Figure 6.3.

For the mass flow rates, the Darcy-Weisbach equation 6.4 accurately represents the pressure loss due to friction along the length of the capillary tube and relates it to the fluid flow velocity [68][69].

$$\Delta P = f\rho\frac{L}{D_h}\frac{v^2}{2} \tag{6.4}$$

where f is the Darcy friction factor, L is the length of the tube [m], D_h is the hydraulic diameter of the pipe [m] and v is the average flow rate in [m/s].

The capillary tube is cylindrical and therefore its diameter can be considered the hydraulic diameter. The Darcy friction factor is usually derived from the well-known Moody chart. A correlation for this

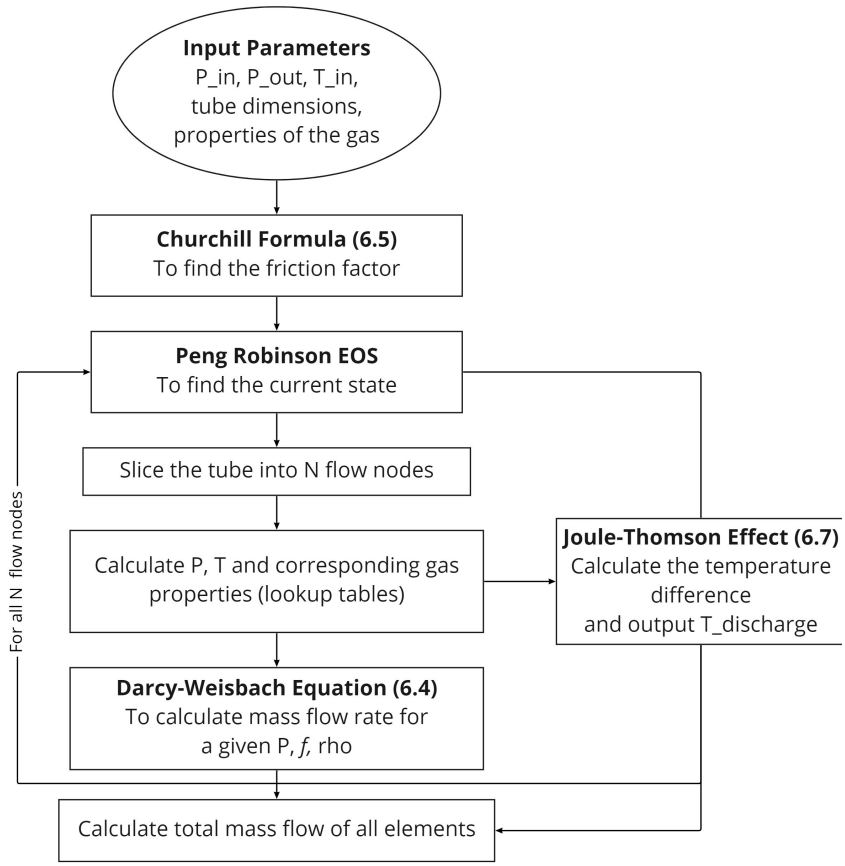

Figure 6.3: Algorithm that describes workings of the compressor model

Moody chart is the Churchill equation given by Equation 6.5. The pressure difference is between the compressor pressure output and the ambient pressure (1 bar) that is outside the capillary tube.

$$\cdot\frac{f}{8} = \left[\left(\frac{8}{\mathrm{Re}}\right)^{12} + \frac{1}{(\Theta_1+\Theta_2)^{1.5}}\right]^{\frac{1}{12}} \quad where \quad \Theta_1 = \left[-2.457\ln\left(\left(\frac{7}{\mathrm{Re}}\right)^{0.9} + 0.27\frac{\varepsilon}{D}\right)\right]^{16}, \quad \Theta_2 = \left(\frac{37530}{\mathrm{Re}}\right)^{16} \tag{6.5}$$

Substituting this information[2], the average flow rate coming out of the capillary tube is obtained. This can then be converted into the mass flow rate [kg/s] using

$$\dot{m} = \frac{\rho \Delta V}{\Delta t} \tag{6.6}$$

The temperature variation caused due to the expansion of gas in the capillary tube is represented by the Joule-Thomson effect.

$$\mu_{JT} = -\frac{\left(\frac{\delta P}{\delta H}\right)_T}{c_p}, \quad T_{out} = T_{\text{in}} - \mu_{JT} \cdot \Delta P \tag{6.7}$$

here, μ_{JT} is the Joule-Thomson coefficient, H is the enthalpy, c_p is the specific heat capacity.
The Joule-Thomson coefficient [K/Pa] varies per gas, the temperature of the gas and pressure before expansion. The value of Joule-Thomson coefficient can either be positive or negative, and is usually

[2]The Darcy-Weisbach equation assumes a constant density. This is the reason behind dividing the tube into numerous sections over which this assumption is valid.

higher at lower temperatures. For air, this coefficient is only about 0.3°C/atm, therefore a pressure drop of about 8bars would only result in a difference of 2.5°C [70]. However, for CO_2, the effects of cooling by Joule-Thomson effect are considerable.
A physical limitation of these equations is that they assume a constant density over the length of the pipe [71]. To include the discrepancies, the tube has been divided into N segments, over which the density can be assumed constant. At the end of each node, the physical state points like pressure, temperature, mass flow are calculated using the Darcy-Weisbach Equation and the Peng-Robinson Equation of State. Properties like the specific heat and density are the updated for the calculated state. The updated state and the new values of the properties are then passed on as inlet conditions for the next segment. In the end, the mass flows from all the segments are summed up to give the total mass flow at the capillary tube outlet.
The validation of this model with experimental data and the following conclusions about the model will be discussed in the next Section 6.5.

6.5. Experimentation

In this section, the method of deriving the compressor map and the repeatable methods used to measure experimental data are explained. This section is not used as just validation, but more so as a supplement- especially to the empirical compressor model.

6.5.1. Motor Losses

Experiments were performed to test the amount of energy lost via the motor to estimate its influence. The temperature on top of the coil and the casing temperature were measured over the course of a compressor run. The data is plotted in Figure 6.4. From the graph it can be seen that there is not much difference between temperature inside the compressor (oil temperature) and the (motor) coil temperature. This verifies the hypothesis that the motor losses are not significant enough to be modelled, especially over the time-scale considered.

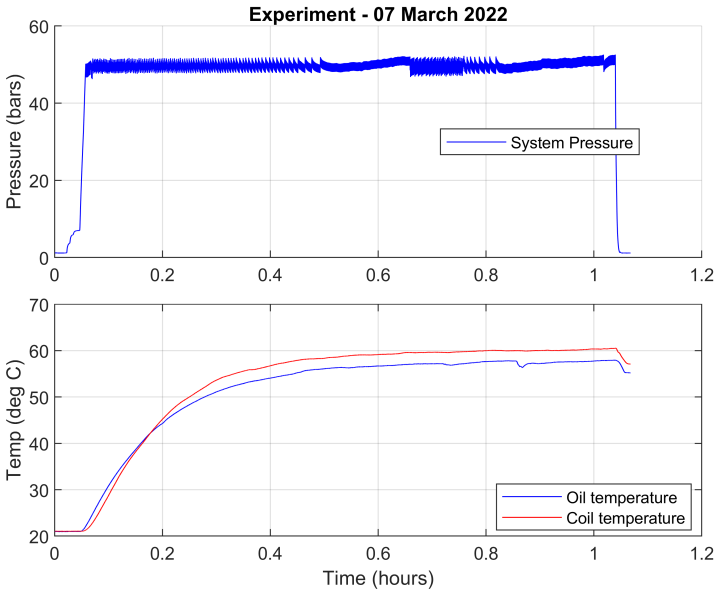

Figure 6.4: Motor coil and Oil Temperatures of the Compressor

6.5.2. Compressor Map

A compressor map is a chart that shows the relationship between compressor performance and its operating conditions. Usage of such charts has been a norm in industries, especially in the case of turbomachinery. An example of a generally used centrifugal compressor map is given in Figure 6.5. Here, the mass flow is plotted against pressure ratios, for each rpm. The contours represent efficien-

cies at these operating conditions.
However it is not yet the norm to provide positive displacement compressors with compressor maps.

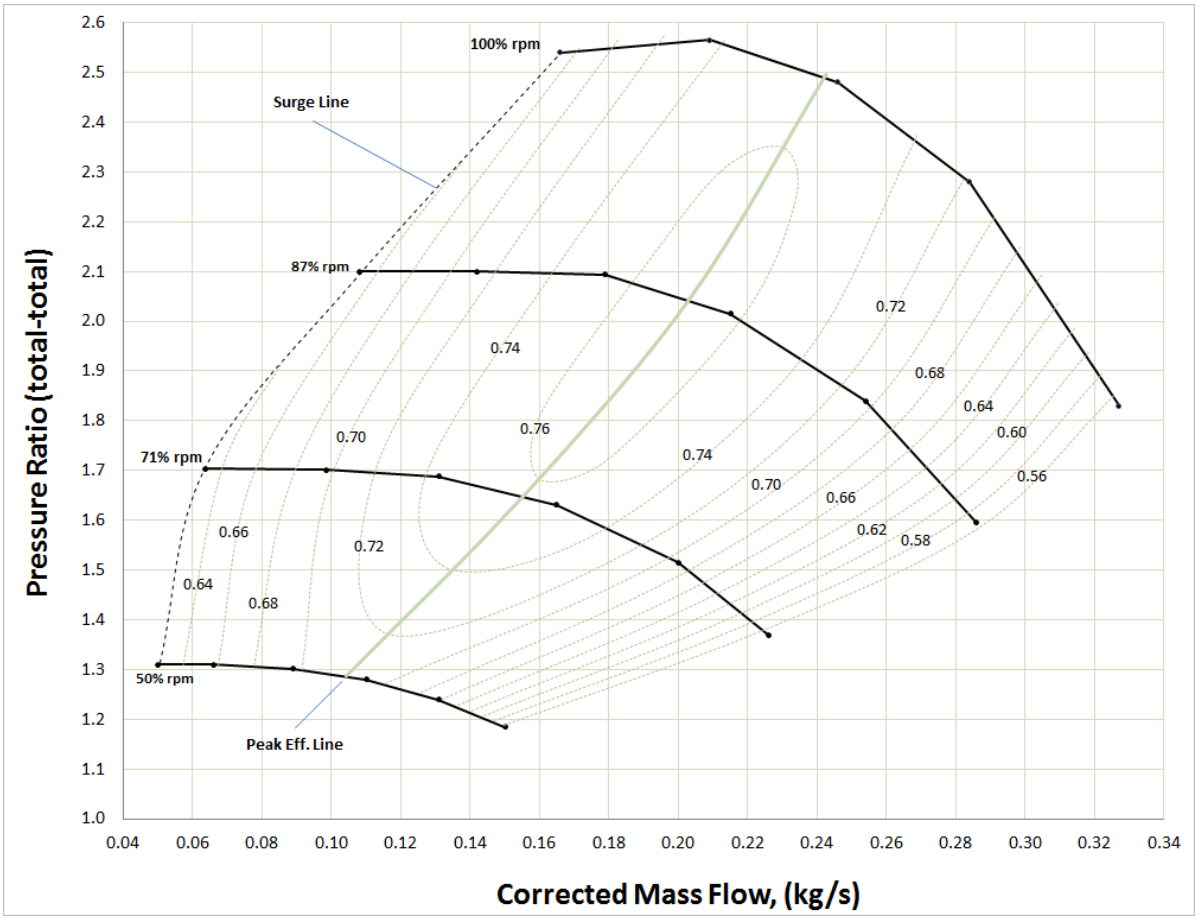

Figure 6.5: Example of a centrifugal compressor map

Such was the case with the Aspen compressors used at ZEF. Even if that was not the case, the modifications made to them also would make them deviate from a given compressor map. The only industrially standardised compressor mapping approach for this kind of compressors is given by ANSI/AHRI Standard 540, published in 2004. It recommends 10-coefficient cubic polynomial models that would require at numerous calorimeter tests to obtain least 20 data-points. This, however, is specifically targeted to KPIs in refrigeration compressors (like COP) that are irrelevant to this project [72]. However, there has been more research into making empirical models of positive displacement compressors and such maps in the recent years. But a standard procedure to be followed is yet to be agreed upon. Cheung et al. [73], discuss various approaches taken in previous works to obtain the coefficients of regressions in such empirical models. Most researches simply fit the data obtained onto this prescribed 10-coefficient polynomial regressions. The physical nature of these coefficients often remain unexplained. They conclude that, for the sake of extrapolation and future predictions, having too many coefficients that do not explain a physical phenomena would be detrimental for the model's design capabilities. Keeping this in mind, a regression fitting is done to the experimental data obtained via the methods explained below.

Experiment Design and Method

Mass Flow Rates:

The modified first stage compressor, which is integrated with the drying system, is equipped with automotive-standard pressure sensors and valves to measure and control the flow. However a means to measure mass flow using sensors is not available. The compressor is allowed to run for different pressure ratios at different rpms and the time stamp for these measures are recorded. The mass flow

rate corresponding to the rate of pressure difference in the compressor is computed in a model[3] by using the ideal gas law assuming a constant overall volume, as in equation 6.8. Note that during the course of these experiments, the fan was turned on and the system was actively cooled. Therefore the compressor casing temperature can also be assumed to be constant.

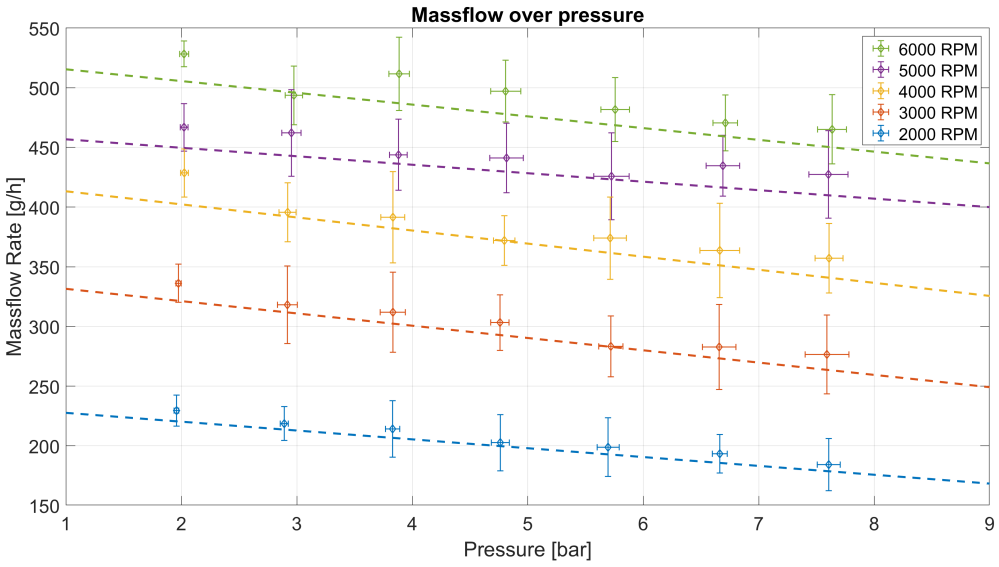

Figure 6.6: Compressor Map of the first stage compressor

$$\dot{m} = \frac{\delta P}{\delta t} \frac{VM}{R_u T} \tag{6.8}$$

where δt is the time differential [h], $\dot{m}$ is the mass flow rate [g/h], M is the molar mass of air 28.964 [g/mol], R_u is the universal gas constant 8.314 [Nm/molK], T is the ambient temperature and V is the total volume.
The experiment is run at seven different pressure steps (from 2-8 bars) with an inlet of ambient air (1bar). For each pressure ratio, the rpm is also varied in steps of 1000 ranging from 2000-6000 rpm. Due to the pressure valve control, there is an upper pressure limit to each run. The average pressure of each run and the average mass flows are plotted along with the standard deviation in each run in Figure 6.6[5].

Power Consumption:
Along with the compressor mass flow rates, the power consumption also needs to be measured to estimate the compression efficiency. Similar to the mass flow measurements, these power measurements are also done for different pressure ratios (2-8bars) running at different rpms (2000-6000). The voltage input of the compressor has a constant 12V supply. Therefore, multiple current measurements were taken using a multimeter (ST-337) at the data points. Power consumption is then calculated as a product of the voltage and current and are given in Figure 6.7.

Polytropic Coefficient:
To predict the discharge temperature of the compressor (that eventually re-loops into the drying system), and to estimate the compressor efficiency- knowledge of the polytropic coefficient is pivotal. Assumption that the compressor goes through a polytropic process is also beneficial because this would emulate all the heat transfer happening inside the system (from the refrigerant to the compressor and vice versa) as a net effect [7]. The course of the process remains unknown, but the endpoint can be calculated- as in a black-box approach.
Experiments carried out previously in ZEF by [8] indicate that the compression has a coefficient (n)

[3][4]

[5]See Appendix B for calculation of error bars.

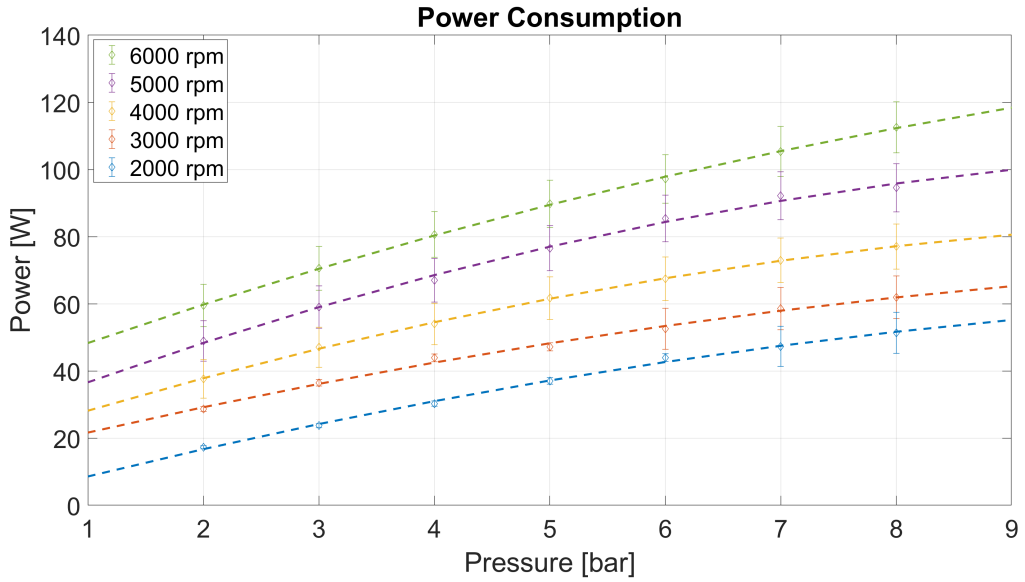

Figure 6.7: Power Consumption Map of the first stage compressor

closer to 1 (which is an isothermal compression). This was estimated by measuring the inlet and discharge temperatures at known pressure ratios and calculating the polytropic coefficient using equation 6.3. Figure 6.8 shows that a **good fit for the polytropic coefficient (n) would be 1.1.**

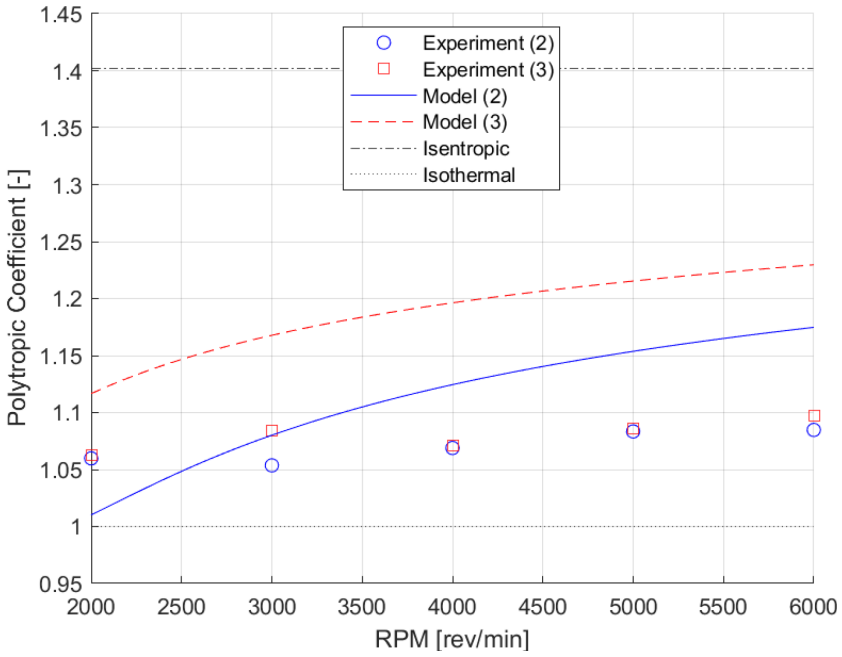

Figure 6.8: Polytropic Coefficient from Experimental Data [8]

Results and Discussion

From the mass flow rate (Figure 6.6) and power consumption graphs (Figure 6.7), a clear correlation between the parameters and the operational conditions can be seen. Moreover, in order to be consistent with the dynamic compressor model, these discrete relationships must be transformed into a continuous form. The mass flow rate data is plotted and interpolated using a linear method on matlab. The interpolated data is plotted on a 3-D graph as shown in Figure 6.9. As expected, the mass flow of the fit increases with increase in rpm and decreases with increase in pressure ratio. A curve-fit re-

gression was performed on this interpolated data to establish a mathematical relationship that can be used in the compressor model. Two types of curve-fits were found to represent the data best- linear and quadratic, and they are depicted in equations 6.9 and 6.10.

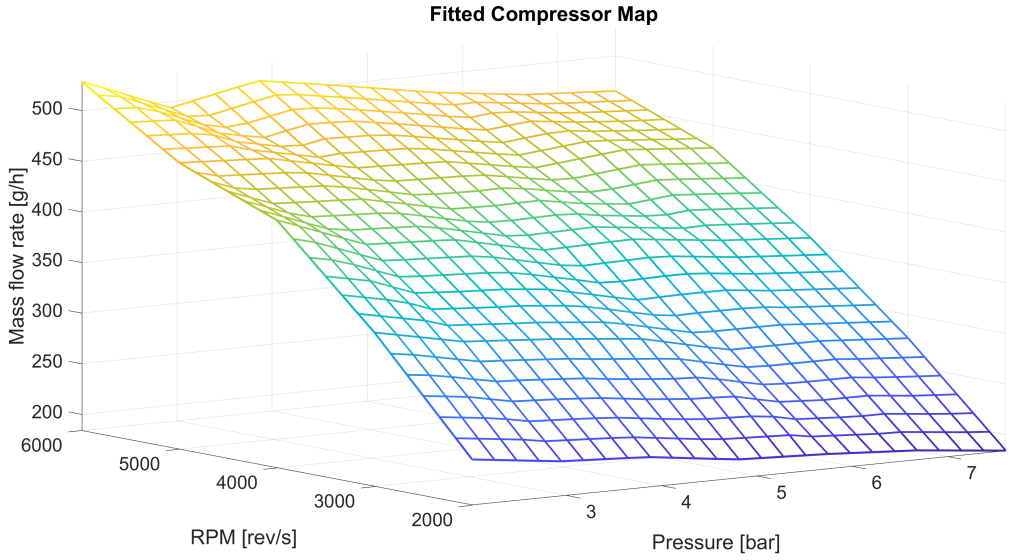

Figure 6.9: Fitted 3-D Compressor Map

$$\dot{m} = 124.5 - 9.408P + 0.0715rpm \tag{6.9}$$

$$\dot{m} = 7.059 - 8.778P + 0.1376rpm - 0.0001577P * rpm - 8.16910^{-6}rpm^2 \tag{6.10}$$

To compare the goodness of fit of mass flow rate models, a commonly used metric is the coefficient of determination (R^2) [74].The second equation which is quadratic is found to be a better fit to the data, with its coefficient of determination (R^2) being 0.9955, whereas that of the first equation (linear) is found to be 0.9781. However, looking at the experimental data in Figure 6.6 there clearly seems to be a linear relationship concerning the mass flows. The quadratic fit is assumed to give a closer fit to match some sort of noise in the measurement- this can be easily explained by the coefficients of the quadratic terms $P * rpm$ and rpm^2- they are extremely small compared to other coefficients. Moreover, the difference in R^2 of both the fits is not significant (0.02), therefore, a choice to **use the linear fit in equation 6.9 is made.** This also obeys the conclusions of [73] where the coefficients like $P * rpm$ and rpm^2, that do not explain any physical phenomena explicitly, must be removed for better prediction accuracy.

A similar approach to find a regression fit for the Power consumption is chosen and the interpolated power data is plotted in a 3-D graph given in figure 6.10.

A sensitivity analysis was performed on various polynomial regressions of varying degrees. The degree of each variable (pressure and RPM) is varied and the goodness of fit is measured in the metrics of Sum of Squared Errors (SSE), Coefficient of Determination R^2 and Root Mean Squared Error (RMSE). In table 6.1, it is easily observed that the goodness of fit factor SSE (Sum of squared errors) decreases dramatically for second degree of pressure and then continues to decrease slowly. For the rpm, the SSE value decreases for the second degree as well. This is the case for the other metrics like R^2 and RMSE as well. It should be noted that lower SSE and RMSE values are desirable and imply that the observed data is closer to the real data. Whereas for R^2, the higher the value (highest being 1) the better the fit.

Looking at the table, a well-suited fit would be a polynomial of second degree for pressure and a second degree for rpm. However, when the experimental data is more closely examined, the relationship between Power consumption and pressure appears to be quadratic although the same does not apply for rpm. To illustrate this better, the mean values of power consumed are plotted against rpm

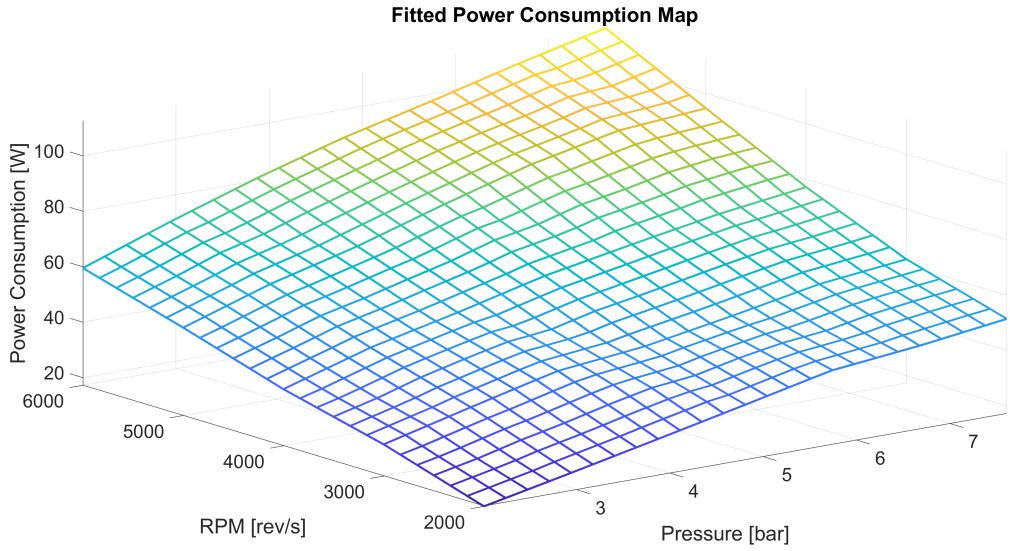

Figure 6.10: Fitted 3-D Power Consumption Map

Table 6.1: Goodness of Fit for Power Consumption Regressions of Varying Degrees

Pressure Degree	RPM Degree	SSE	R^2	RMSE
1	1	339	0.9823	3.255
2	1	77.31	0.996	1.605
3	1	75.45	0.9961	1.642
4	1	74.44	0.9961	1.692
5	1	74.36	0.9961	1.76
1	2	124.8	0.9935	2.04
2	2	57.32	0.9965	1.406
3	2	40.71	0.9979	1.251
4	2	39.12	0.998	1.304
5	2	39.04	0.998	1.397
1	3	101.8	0.9947	1.907
2	3	33.26	0.9983	1.131
3	3	32.43	0.9983	1.139
4	3	19.75	0.999	0.9699
5	3	18.06	0.9991	1.031

values at constant pressures in Figure 6.11.

Figure 6.11 verifies the assumption that the relationship is not quadratic but more so linear. The goodness of fit, again, is probably better for the quadratic one due to a better fit to the noise in the data. Therefore, the most suitable curve-fit for the power consumption is a quadratic regression given by equation 6.11.

$$Power = -17.99 + 7.77P + 0.009035rpm - 0.4009P^2 + 0.0008328P * rpm; \tag{6.11}$$

Recalling the conclusions from [73], the term of $P * rpm$ is ignored, for better predictability of the model, as it quantifies no significant physical phenomena. It is also evident that it portrays some sort of noise from the insignificant value of its coefficient (0.000832). **Therefore, the regression ultimately used for power consumption is in equation 6.12.**

$$Power = -17.99 + 7.77P + 0.009035rpm - 0.4009P^2; \tag{6.12}$$

Validation

Since the built model is statistical and therefore based on the experimental data, it is known that it predicts data for this specific modified Aspen compressor well. This fulfills the goal of the compressor model. However the goal of this project is to provide ZEF with a design tool while aspiring to provide a new, inexpensive method to build an empirical positive displacement compressor model. This requires

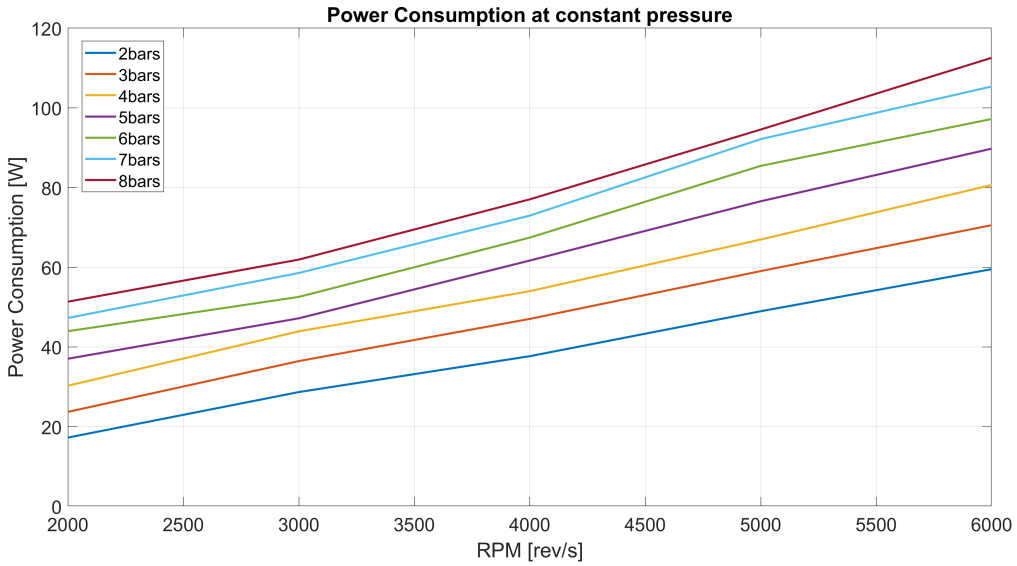

Figure 6.11: Relationship between Power Consumption and RPM at Constant Pressures

the compressor model to allow for extrapolation onto a wider range of applications, still limited to small displacement rolling piston compressors.

For this reason, the results of the model are also compared to some experimental data found in literature. In an experimental evaluation done by [9], various tests were performed on the hermetic (unmodified) Aspen 1.4 [cc] compressor, with R134a as the refrigerant. Although this is different from the compressor modelled (due to the modifications and the working fluid) a comparison is still made to check if there are any similarities. Figures 6.12a, 6.13a, 6.14a and 6.15a show the efficiency at different pressure ratios for 3000, 4000, 5000 and 6000 rpms respectively. They are compared against data from [9] for 3000, 4500 and 6000 rpms shown in Figures 6.12b, 6.13b, 6.14b and 6.15b. The efficiencies of the model calculated at all ranges of rpms and pressures is shown in Figure 6.16. Another discrepancy to keep in mind besides the refrigerant and the modifications is that the suction (inlet) pressure of the model is 1 bar and that of the published data is 3bars. The magnitude of the efficiency of the unmodified Aspen compressor is higher than that of the (modified) compressor modelled. This is not surprising and can be explained not only by differences in heat transfer with ambient between the new modular housing and the mass manufactured housing- but also mainly due to the difference in the working fluids. Another research at NIST [75] showed that R134a as a refrigerant consistently had a higher COP than CO_2, with the least difference being 21% at 32.2°C, 1000rpm. This difference in COP increased from 21% to 34% at a higher temperature for the same rpm. As the frequency increased to 3000rpm, the difference in COP increased to the range of 42-60%. This explains the higher efficiency on the right hand figures and also a decrease in the efficiency with an increase in rpm.

Besides these deviations, the trend in efficiencies at comparable frequencies predicted by the model and recorded by the paper are agreeable. It can be noticed from Figure 6.16 that efficiency decreases with increase in rpm until a certain pressure ratio, and then favours mid-range frequencies (eg: 3000 and 4000rpm). This shows that there is a 'most-efficient frequency' operation zone for a range of pressure-ratios. 2000rpm being this for 1 to 3.2 pressure ratios, followed by 3000rpm from 3.2 to 5.2 pressure ratios and then 4000rpm being the most-efficient range until pressure ratio 8. Furthermore, it increases with increase in pressure ratio, and each frequency line has a 'dip' around pressure ratio 5-6. This can be explained by the oil reaching temperatures where there is a noticeable change in viscosity- implying the compressor needs to do more work to reach the same amount of pressure output, hence lowering the efficiencies.

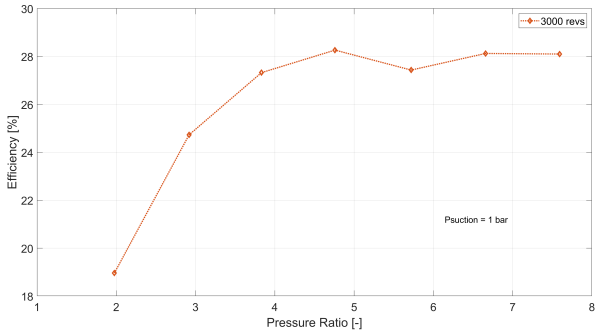

(a) Compressor Map Efficiency at 3000RPM and Psuction=1 bar

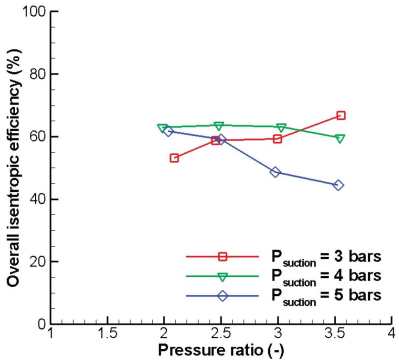

(b) Compressor Map Efficiency at 3000RPM and Psuction=3 bar

Figure 6.12: Comparison of model efficiency data vs literature [9] at 3000rpm

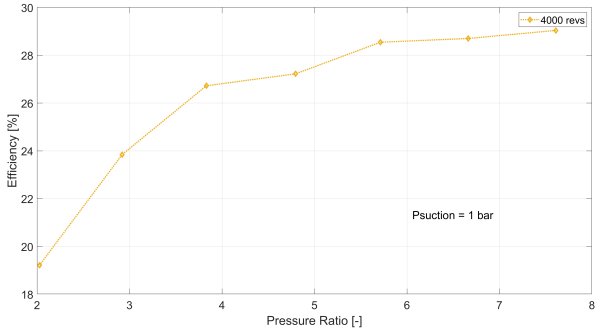

(a) Compressor Map Efficiency at 4000RPM and Psuction=1 bar

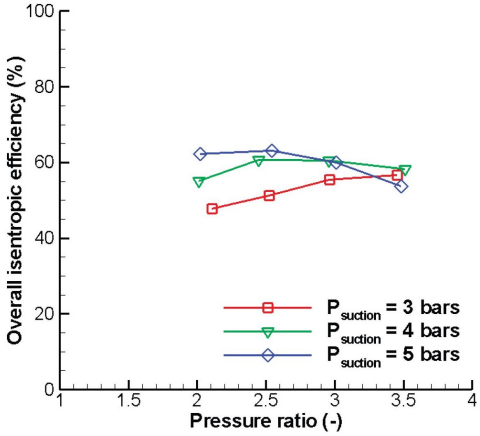

(b) Compressor Map Efficiency at 4500RPM and Psuction=3 bar

Figure 6.13: Comparison of model efficiency data vs literature [9] at 4000rpm

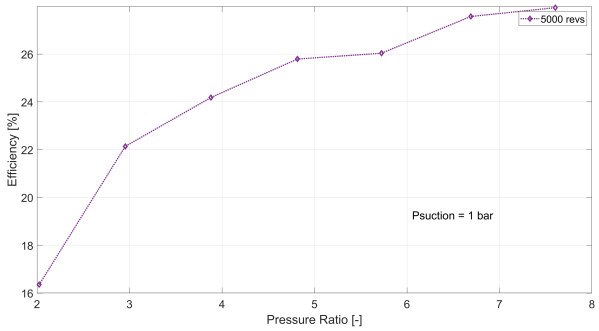

(a) Compressor Map Efficiency at 5000RPM and Psuction=1 bar

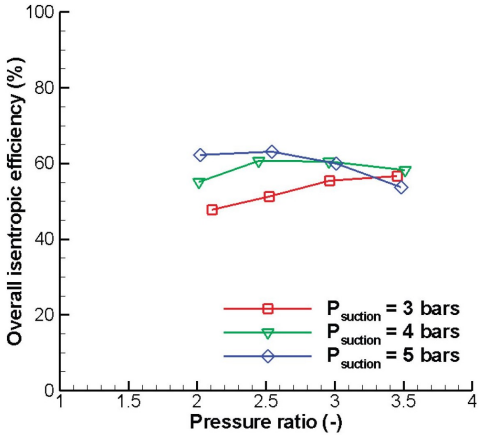

(b) Compressor Map Efficiency at 4500RPM and Psuction=3 bar

Figure 6.14: Comparison of model efficiency data vs literature [9] at 5000rpm

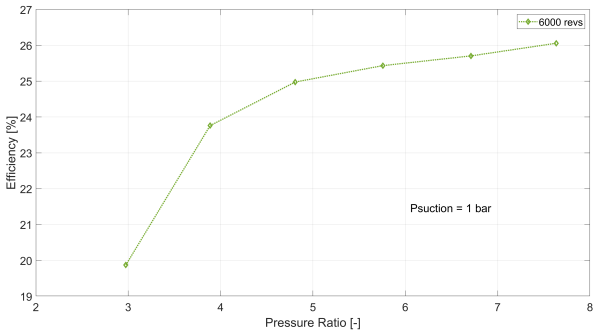

(a) Compressor Map Efficiency at 6000RPM and Psuction=1 bar

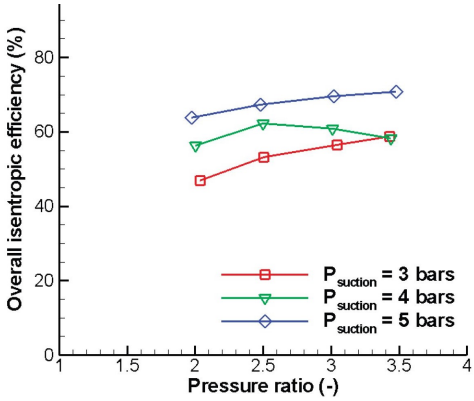

(b) Compressor Map Efficiency at 6000RPM and Psuction=3 bar

Figure 6.15: Comparison of model (isentropic) efficiency data vs literature [9] at 6000rpm

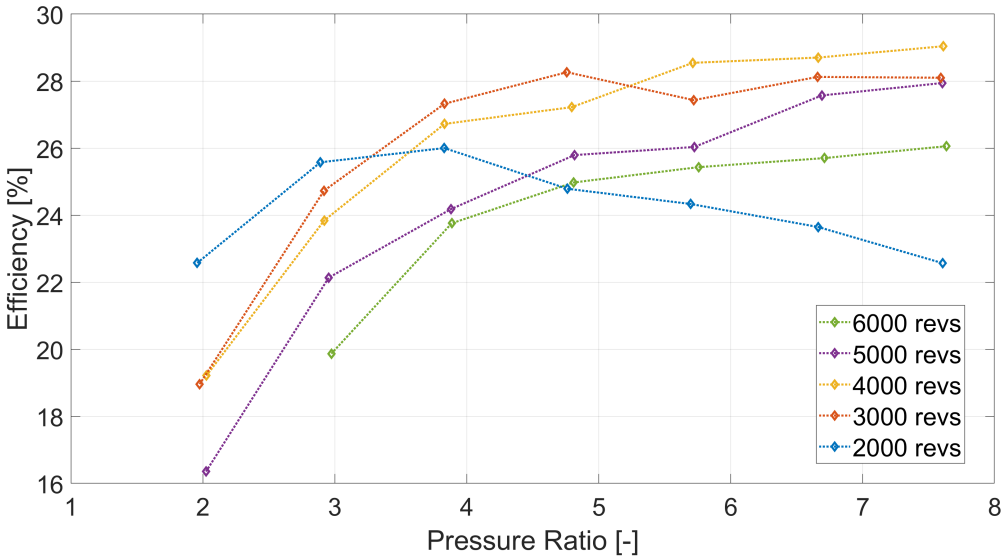

Figure 6.16: Isentropic efficiencies of the first stage compressor predicted by the model

6.5.3. Capillary Tube

The capillary tube model described in Section 6.4.1 is a slightly modified version of a model that has already been designed in ZEF for the Methanol Synthesis Reactor purposes [71]. However this adapted model is to be validated with experimental data.

Experiment Design and Method

To this end, the readings of mass flows after the capillary tube are taken at two different pressures (3 and 5 bars) over the entire frequency range (2000 to 6000 rpm). As there is no pressure sensor at the end of the capillary tube, these measurements were taken using a syringe, in an analog manner. The amount of displaced water inside the syringe due to the mass flow output at the capillary tube outlet and the time taken for it is noted down for each data point. The average mass flow rate at 2.76bars was found to be 45±3 [g/h] whereas the model predicts a value of 45.7 [g/h]. At 4.21bars, the experiments have an average of 67±10 [g/h] and the model gives 75.9 [g/h]. The model's predictions lie within a 95% confidence range of the standard deviation of the experimental data, and is therefore verified.

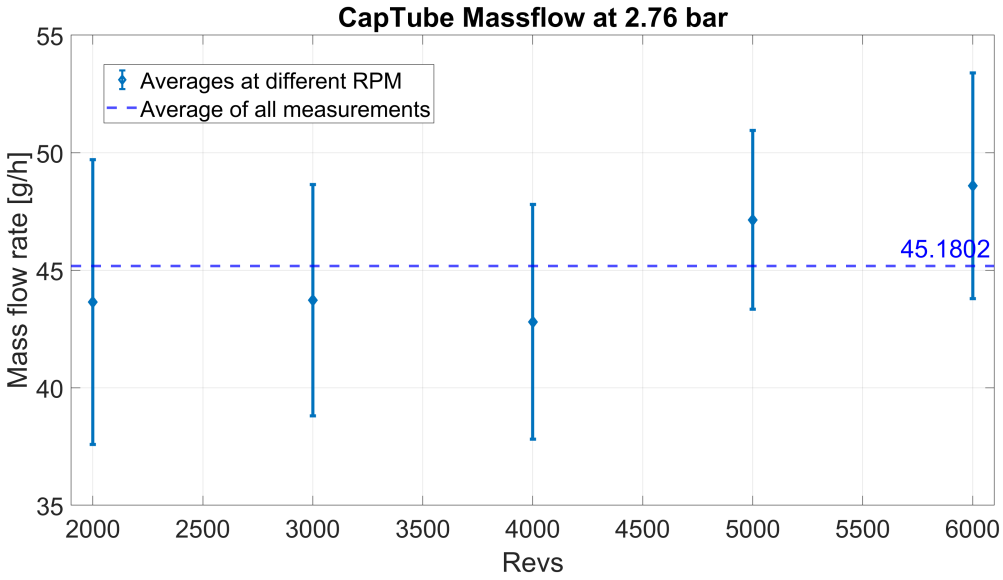

Figure 6.17: mass-flow rate after the capillary tube at 2.76 bars

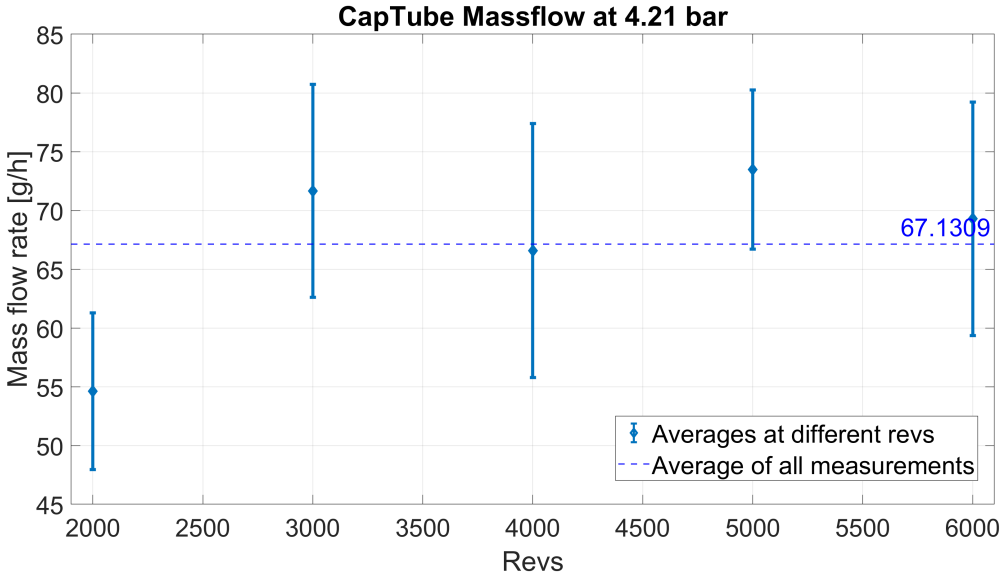

Figure 6.18: mass-flow rate after the capillary tube at 4.21 bars

Results and Discussion

Figures 6.17 and 6.18 show that there is not much variation in mass-flow rates with rpm[6]. However, as expected, the mass-flow rate does depend on the pressure differential, in accordance with the Darcy-Weisbach equation 6.4. The variation in the standard deviation might look huge, but it is important to notice that the metric used is [g/h]. When portrayed on the entire range of mass flows that would exit the capillary tube (the highest being 175 [g/h] for 8 bars), the variations are illustrated more to scale and can be concluded negligible. This is shown in Figure 6.19. From graph 6.20, it can also be noticed that the relationship between the mass-flow and pressure looks linear. Hence, it was deemed wiser to use a regression for this as an extension to the compressor model, to save computation time. **The linear fit used for the capillary tube mass flow is given by equation 6.13.**

$$\dot{m}_{cap} = 23.374P - 14.525 \tag{6.13}$$

[6]See Appendix B for calculation of error bars.

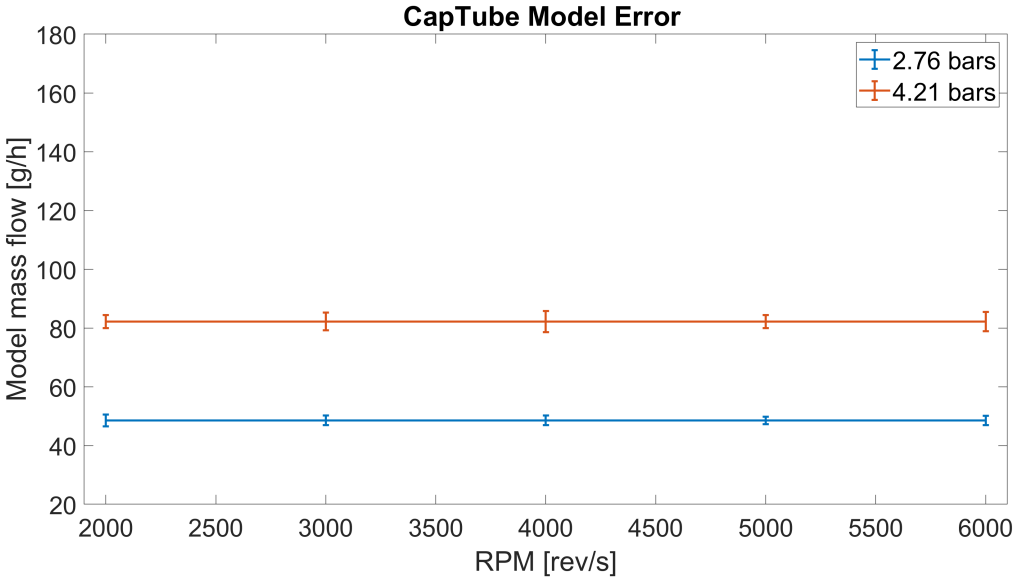

Figure 6.19: Error in mass-flows after capillary tube when illustrated over the entire range of mass-flows

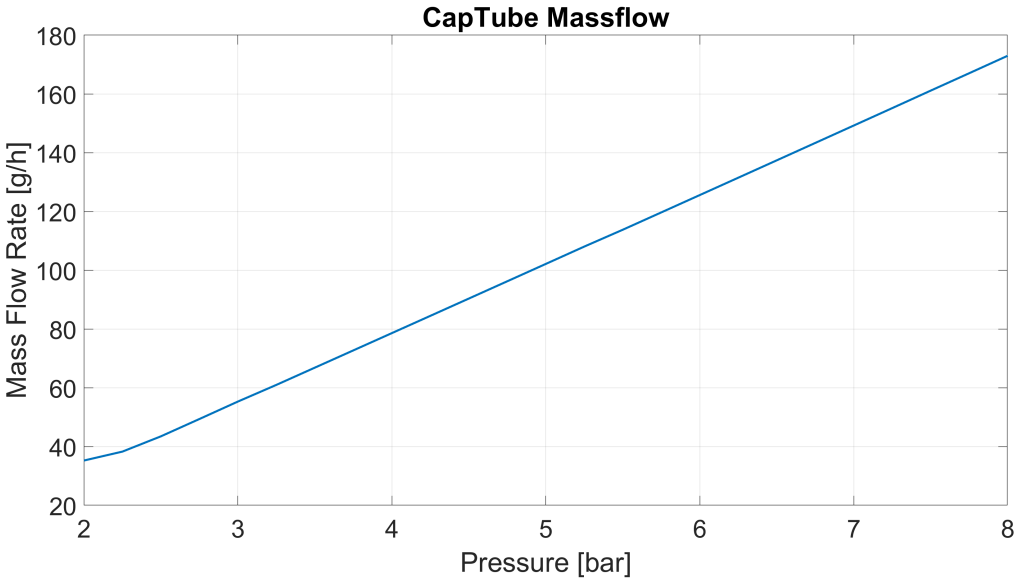

Figure 6.20: mass-flow rate after the capillary tube over different pressures

6.6. Using the Compressor Model as a design tool

The model described in this section predicts the output process parameters of the first stage compressor satisfactorily. In order to use it as a 'design tool', this model should be able to predict the behaviour of the higher stage compressor with little modifications in place.
At the time of completion of this work, the higher stage compressor was built and integrated with a modified first stage. Measured data that is used to match the mass flows of all the stages, is illustrated in table 6.2. It shows that the model can be used to extrapolate mass flows of the higher stage compressors as well.
To obtain the mass flow output of the modified first stage compressor with 2.8 [cc/rev], from the model

Table 6.2: Mass flows of higher stages- modelled and measure values

	rpm	4000	4000	2630
	cc/rev	1.9	2.8	0.57
Modelled	mol/h	18.64	27.47	27.6
Measured	mol/h	18.64	28.5	28.57

output of a compressor with 1.9 [cc/rev], equation 6.14 is used.

$$\dot{m}_2 = \dot{m}_1 \frac{V_2}{V_1}; \quad V_{new} = 2.8\ cc/rev,\ V_1 = 1.9\ cc/rev \tag{6.14}$$

$$rpm_2 = rpm_1 \frac{V_2}{V_1} = 2630 \quad rpm_1 = 4000,\ V_2 = 0.57\ cc/rev,\ V_1 = 1.9\ cc/rev \tag{6.15}$$

In order to extrapolate the mass flow of a higher stage compressor with 0.57 [cc/rev] displacement volume, not only the volume ratio but also the pressure ratios must be included in the product as given in 6.16. This is because the higher stage compressor and model compressor differ not only in their displacement volumes, but also their operational pressure and frequency ranges. As discussed in Section 6.5.2, there are different frequency ranges that give maximum efficiency at different pressure ratios. The new frequency for the higher stage that matches the mass flow of the previous stage is given by equation 6.15. However, since this was not the case for the modified first stage compressor (with 2.8 cc/rev), as they both operate until pressures of 7.5 bars, the pressure ratio was not taken into account.

$$\dot{m}_2 = \dot{m}_1 \frac{V_2}{V_1} \frac{rpm_1}{rpm_2} \frac{P_2}{P_1}; \quad V_2 = 0.57\ cc/rev,\ V_1 = 1.9\ cc/rev \quad P_2 = 55\ bar,\ P_1 = 7.5\ bar \quad rpm_1 = 4000,\ rpm_2 = 2630 \tag{6.16}$$

7

Conclusions and Recommendations

7.1. Conclusions

An integrated model of the dynamic fluid machinery system was built to be used as a design tool. It has two sub-components- the drying system of two packed bed (silica gel) columns and a compressor. In order to build the model and subsequently use it as a design tool, the following questions were answered.

What are the process parameters that are relevant for dynamic operation of the compressor train? After performing a characteristic time-scale analysis of physical phenomena that occur inside both the sub-systems, the most interesting dynamic process parameters were found to be: Variation in relative humidity and temperature due to the drying system, pressure fluctuations due to the compressor and changes in thermo-physical properties of the gas due to change in temperature.

What are the external factors that affect dynamic operation of the system? (Eg: DAC output stream, Power Fluctuations) The external factors that affect the dynamic operation are considered to be: changes in the ambient temperature and hence the variation in water content of air, and variation of solar irradiation.

What are the bottlenecks of the current compressor train, drying system and DAC buffer flash tank? It is hard to identify the bottlenecks of each component without looking at their consequences on a bigger scale.

- The bottleneck of the drying system is the cyclic capacity of each cycle. If the time taken until the adsorption cycle hits breakthrough is shorter than the time taken for regeneration, it is not possible to operate the FM system continuously.
- The bottleneck of the compressor is that its mass flow needs to be adequate to meet the production targets of ZEF, while also maintaining it at a level so that the residence time of the gas inside the drying system is reasonable. Otherwise, if the residence time is too low, a higher amount of energy would be required to heat up the same amount of gas.
- The DAC buffer flash tank not only provides the input to the FM system, but also handles the output from the drying system re-loop. The compressed gas used to purge out the water vapour and regenerate the drying column is passed back to the DAC buffer tank. The bottleneck here is that the pressure fluctuations caused by this re-loop must not be higher than 20 mbars, due to specifications of the buffer tank.

What is the effect of fluctuations in the dynamic parameters on the system performance? The variations caused by ambient temperature on gas properties are implemented using empirical relations and shown to have effects on the cyclic capacity over time of the drying system. For example, increase in temperature would lead to an increase in RH of the gas, but this would also lower the adsorption

capacity of the silica-gel, due to operation at higher temperatures. In order to avoid a quicker breakthrough caused by this increase in temperature over a day, the drying system columns need to be resized. The model built can be used as a design tool to estimate the sizing of this new setup accordingly.

What are the implications of running a discontinuous compression train including the drying system? During the integration of the subsystems, it was realised that the effect of pressure increments and thus the mass flow fluctuations caused by coupling the compressor to the drying system is not perilous. This is mostly because the time-scale of the compressor variations (300s) was found to be much smaller than that of the drying system (8hours/day). This would mean an almost constant massflow input into the drying system columns. The effect of pressure variations on the re-loop to the DAC output stream are controlled by appending a capillary tube between the compressor downstream and the desorbing column. The capillary tube controls the massflow coming out of the compressor and reduces the pressure back to 1bar. Following that, the pressure drop due to the flow inside the packed bed was investigated and concluded to be negligible (15e-5 bars).

Is it feasible to dynamically operate the system (for instance following the profile of the direct air capture system output)? If so, what is the control strategy and optimum operation envelope? The control strategy for continuous/dynamic operation of the FM system is to ensure that the time taken for adsorption is longer than that taken to regenerate the packed bed column. The strategy is therefore to switch between the adsorption and desorption cycles, just in time. This control is thus incorporated into the integrated model and can be adapted to future design iterations. The optimum operation envelope is decided by adapting the strategy in such a way the difference between these cycle times is kept to a maximum, at all RH inputs from the DAC system output stream.

Finally, the project fulfills its purpose to bridge the gaps in science pertaining to modelling multiple cycles of TSA drying systems over larger periods of time. Furthermore, it is capable of predicting the performance of miniature rolling piston compressors using a black-box model that can be extrapolated onto other compressors lying in a similar range of compression capacity.

7.2. Recommendations

To improve the validity of the model, reduce errors and use the model to its fullest potential, further work can be done in the areas mentioned hereunder.

7.2.1. Drying System Model Parameters

Some of the heat and mass transfer properties in the model vary with the column sizing and the amount of silica gel beads in the column. The approach to change these parameters to the new sizing was briefly discussed in Section 5.7. Here, suggestions are given to develop the model even further to close the gap between the experiment and model data.

- Heat of Adsorption: Modifying the (Clausius-Clayperon) equation used to obtain the heat of adsorption could make the temperature estimates by the model closer to the experimental data. A combination of more realistic and material-specific Antoine equation along with the Clausius-Clayperon equation gives a higher heat of adsorption as given by Equation 7.2 whereas Equation 7.1 gives the Antoine equation itself. Here, a, b, c are material-specific constants and the first term in 7.2, A, is the adsorption potential[1] and the second term is the latent heat of vaporization (which is already included in this model)[2].

$$\ln p^* = a - b/(T + c) \tag{7.1}$$

$$\Delta H = -A - bRT^2/(T + c)^2 \tag{7.2}$$

- Thermal Conductivity of packed beds and Axial Dispersion Coefficient: Various models in literature used to calculate the overall thermal conductivity of packed beds are tested in this work. However, assumptions like homogeneous packing fraction and a uniform size distribution amongst the

[1] Given by Equation 3.13.
[2] Given by the Clausius-Clayperon Equation 3.17

silca gel beads do not necessarily hold true- especially after a few runs of experimental cycles. The silica gel is more prone to breaking due to water exposure at high temperatures, and the size distribution is not homogeneous anymore. The effects of these need to be investigated further, for life-cycle assessments. Other models for thermal conductivity of packed beds can be found in [76] and for axial dispersion coefficient can be found in [77].

- Adsorption Isotherm Validity: The Dubinin-Raduschkevich equation is used to represent the equilibrium state of the adsorption and desorption curves in this work as it adequately describes drying by porous media like the silica gel beads. Other isotherms that describe single solute adsorption like the Langmuir isotherm and the Freundlich isotherm models are not investigated. Besides this, another version of the Dubinin-Raduschkevich equation was found, from [55], for adsorption of aqueous-solution given by Equation 7.3. This version that replaces partial pressure with solute-concentration (c_s and c_e)could be implemented for the desorption cycle, once condensation is observed.

$$A = \mathrm{RT} \ln\left(\frac{\mathrm{C_S}}{\mathrm{C_e}}\right) \tag{7.3}$$

7.2.2. Drying System Operational Strategy

- Regeneration of the column: To realise the model to its fullest potential, the best operational envelope can be found by varying the fraction of regenerating the columns. When using it to determine column sizing, the control strategy inside the model could be changed to allow only partial regeneration of the column. In that case, the water content inside the column, at the start of the next adsorption cycle, is not zero. The effects of the breakthrough cycle time then depend on how much percentage of regeneration has been done and the new length of the column. This has a significant influence on the energy intake of the system by reducing the total time for regeneration and needs to be determined for every new sizing.

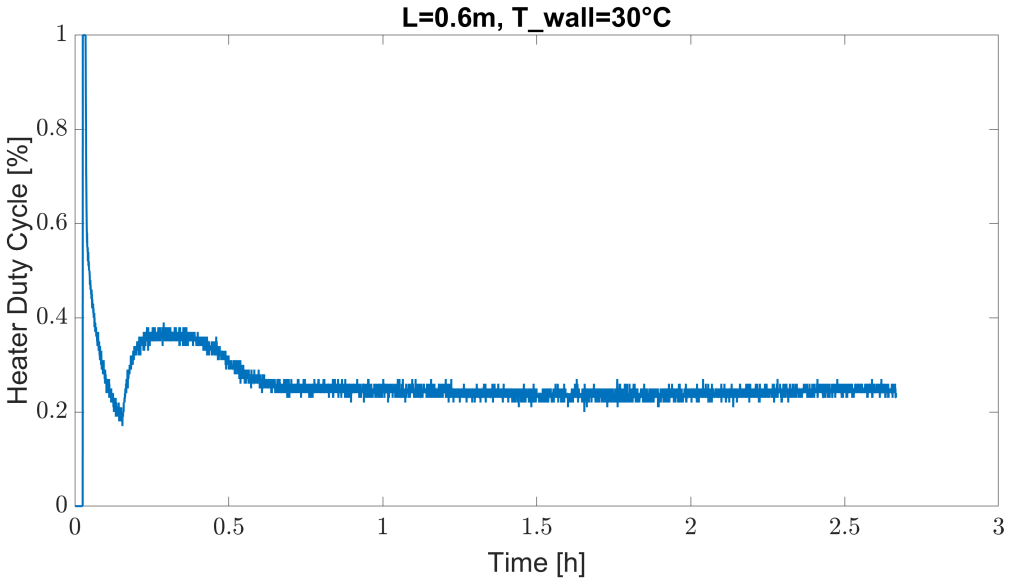

Figure 7.1: Heater Cycle Duty of an experiment where T_{wall}=30°C

- Heater Duty Cycle: Most of the energy costs of the drying system are attributed to the heater costs. The goal of heating the drying system is to bring the column to a desorption temperature and aid the endothermic reaction rate. It is not to maintain a constant wall-temperature, as done in the experimental setup. In the experiment, the NTCs located on top of the heater pads provide feedback to the (arduino) controller about the required changes to the heater power to maintain the wall temperature at a certain temperature, shown by Figure 7.1. This is simulated in the model as a pulse, that stops after half of the desorption cycle duration as shown by the bands in Figure 5.7. The heating cycle length on the model can be varied to a longer duration and a

lower temperature or vice-versa and its influence on the total energy costs can be studied while designing a new system.

7.2.3. Compressor Model as a Design Tool

Towards the end of this work, a new modified compressor train prototype was designed in ZEF. The compressors used had a similar refrigeration capacity as the one used in this work. Methods to extrapolate this model to the new compressors was discussed in Section 6.6. However, more experimental data from this new system is required to check the validity limits of this model.

7.2.4. Experimental Setup

- RH Sensors: Due to the error range of most RH-sensors available in the market, it was not possible to understand exactly when the column hit breakthrough- which was an important KPI for the system. In addition to that, desorption characteristics of the experiments were not studied, with respect to the relative humidity values, due to the malfunctioning of sensors in case of condensation. For future work, sensors with condensation filters for protection against desorption and higher precision are recommended.
- NTC location- Drying System: The temperature sensors used in the setup were the previous heater-rods. The precise location that corresponds to the temperature reading is unknown. Since the model is capable of predicting the temperatures across numerous nodes, this is not a crucial problem. However, if these heaters were to be replaced by temperature sensors, it should be noted that they should also record data of nodes that are not too far downstream. Due to the channelling effect caused by the ratio of the tube diameter to pellet diameter [38], the fit of heat and mass transfer coefficients would be erroneous if the data would be measured at the end of the inlet/outlet.
- NTC location- Compressor setup: It was realised, towards the end of this project, that the estimation of the polytropic coefficient for compression was made by measuring the temperature at the outlet of the compressor. Due to the flow at the outlet, there could be cooling effects on the sensor. This would imply higher temperatures at the outlet and an increase in the polytropic coefficient (>1.1). The implementation of this is straight-forward in the compressor model and could be consequential to the energy demands of the drying system downstream- especially when the working fluid is CO_2. Then the effect of Joule-Thomson cooling at the end of the capillary tube and eventually on the desorbing column inlet can be determined.
- Working Fluid: Experiments with CO_2 as a working fluid need to be carried on, to calibrate the model parameters to real-time scenarios of ZEF. As mentioned above, usage of CO_2 can lead to higher compression outlet temperatures- which could reduce the necessity of desorption heating energy.

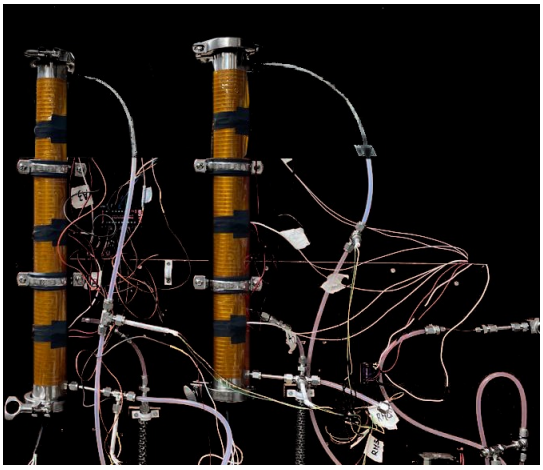

Figure 7.2: The Drying System Setup

A

Experimental Setup

In this section, a few pictures of the experimental setup are shown.

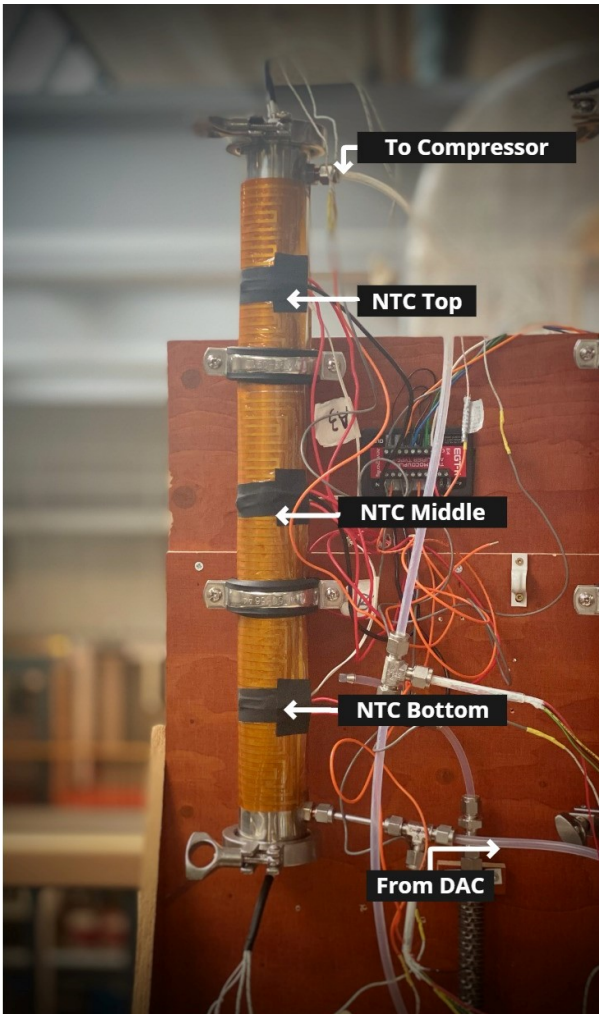

Figure A.1: Drying Column

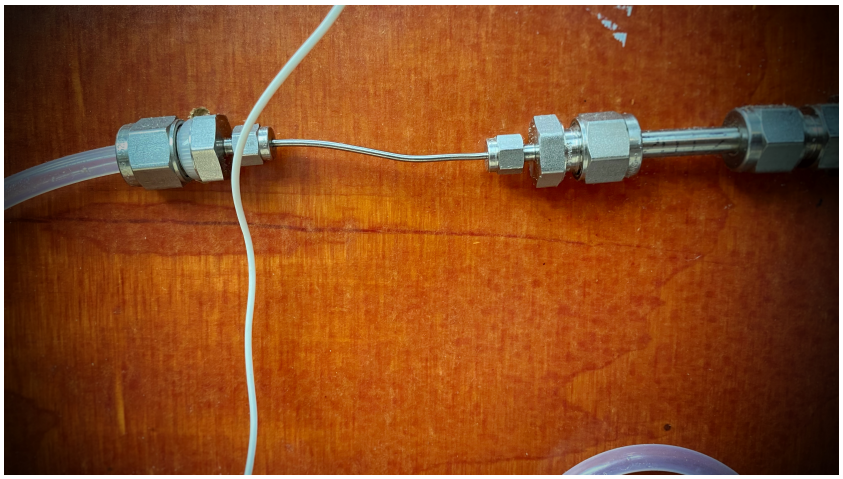

(a) Capillary Tube

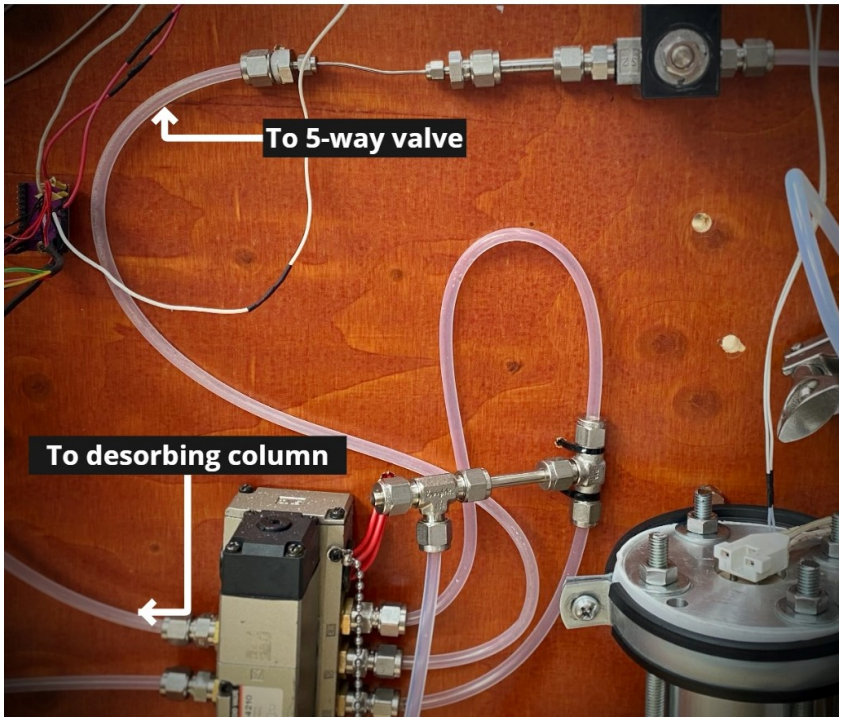

(b) Connection to the 5-way valve

Figure A.2: Capillary Tube

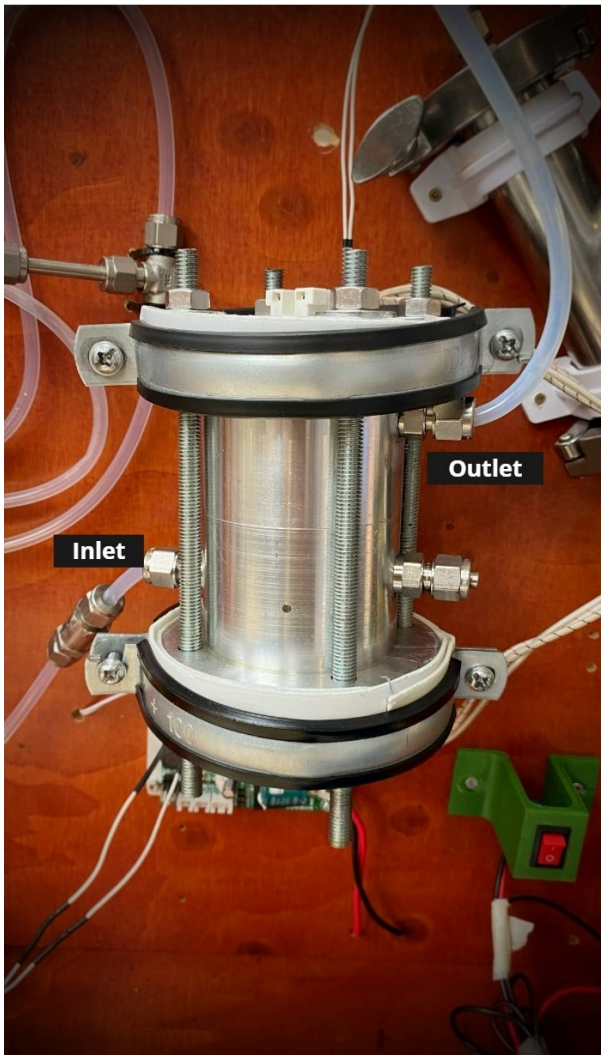

Figure A.3: Modified first stage compressor

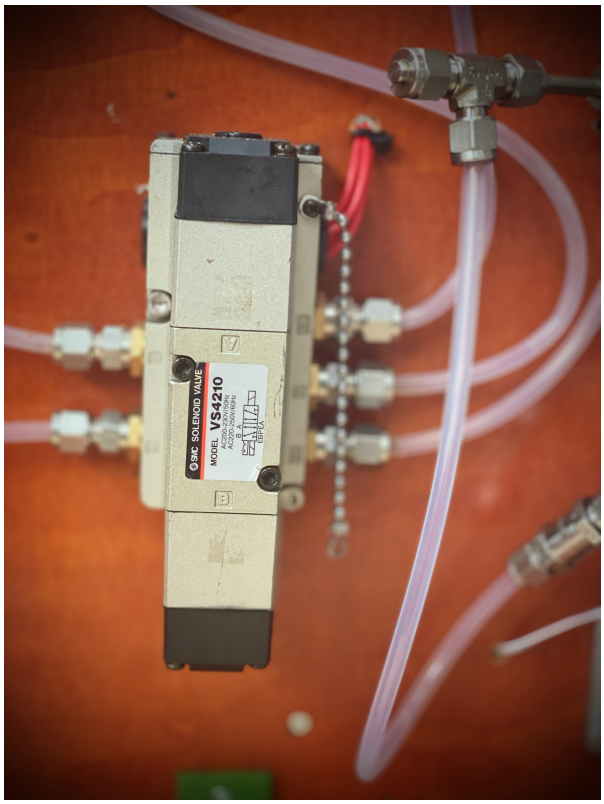

Figure A.4: 5-way solenoid valve that controls flipping

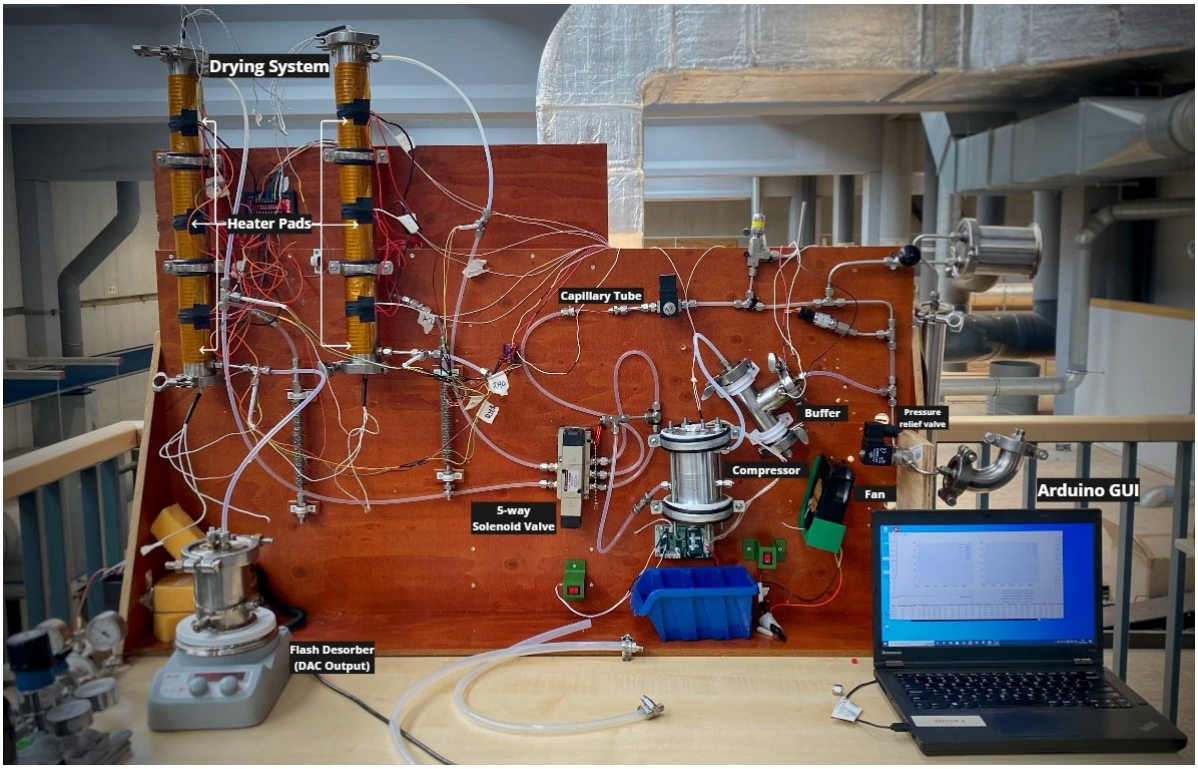

Figure A.5: The integrated setup comprising the drying system, the compressor and the arduino reader

B

Errors

While measuring experimental data, some errors are inevitable due to the precision range of the sensors used. Knowing these error ranges could help the reader gain more insight, especially when using this data for comparison.

B.1. Drying System:

In the drying system setup, it was very important to know the limitations of the relative humidity sensor, as it showed errors in the most critical zone (RH=<2%). The sensors also malfunctioned many a time, due to condensation on their capacitative film. A clipping of the data-sheet of the Honeywell HIH8121-021-001 sensors used is provided in Figure B.1. Other widely used capacitive sensors also had an uncertainty range of ±2%, so this error could not be circumvented. Besides the information provided by the manufacturer, experiments done at ZEF attested that the error in these sensors was usually higher than the prescribed 2%. This can be seen in Figure 5.13 where three different sensors were placed at the same location. The temperature data, however, was more reliable with an error range of ±0.5°C.

B.2. Compressor:

The compressor map that indicates the mass flow rate and power consumption is based solely on experimental data. The error bars in Figures 6.6, 6.7, 6.17 and 6.18 are calculated as follows:

B.2.1. Power Consumption:

The power consumed was measured by the means of a power clamp meter (Standard ST-337) which has an uncertainty range of ±2.5%+4d. It has two settings wherein the first setting that measures 0-4A, shows accuracy up to 3 decimal places and the error is ±2.5%+ 0.004A. The second setting records 4-80A and displays data with one decimal points- the error here is ±@.5% +0.4A. This is the reason why there are smaller error bars at 2000rpm and 3000rpm and larger error bars at higher frequency ranges.

B.2.2. Compressor Map- Pressure and Mass Flow Rate:

The pressure sensor used was AE-SML by AE Sensors B.V. These sensors had an inaccuracy of ±0.5%. The data-sheet cane be found here. To calculate the mass flow rate for the compressor map, the pressure derivative was required. Since the pressure sensor detected the pressure at each time stamp, the pressure increase was just calculated by subtracting pressure at two consecutive time-steps. However, the maximum pressure output was capped at different pressure values to estimate the flow rate in the range of 1-8 bars. This caused noise in the pressure readings, as the pressure dropped to zero when the maximum pressure was reached. This noise was filtered out in the code, and an error was calculated for the mean pressure derivative values and mass flow derivative values as:

$$\delta_p = 3\sigma_p/\sqrt{n}; \delta_m = 3\sigma_m/\sqrt{n}; \tag{B.1}$$

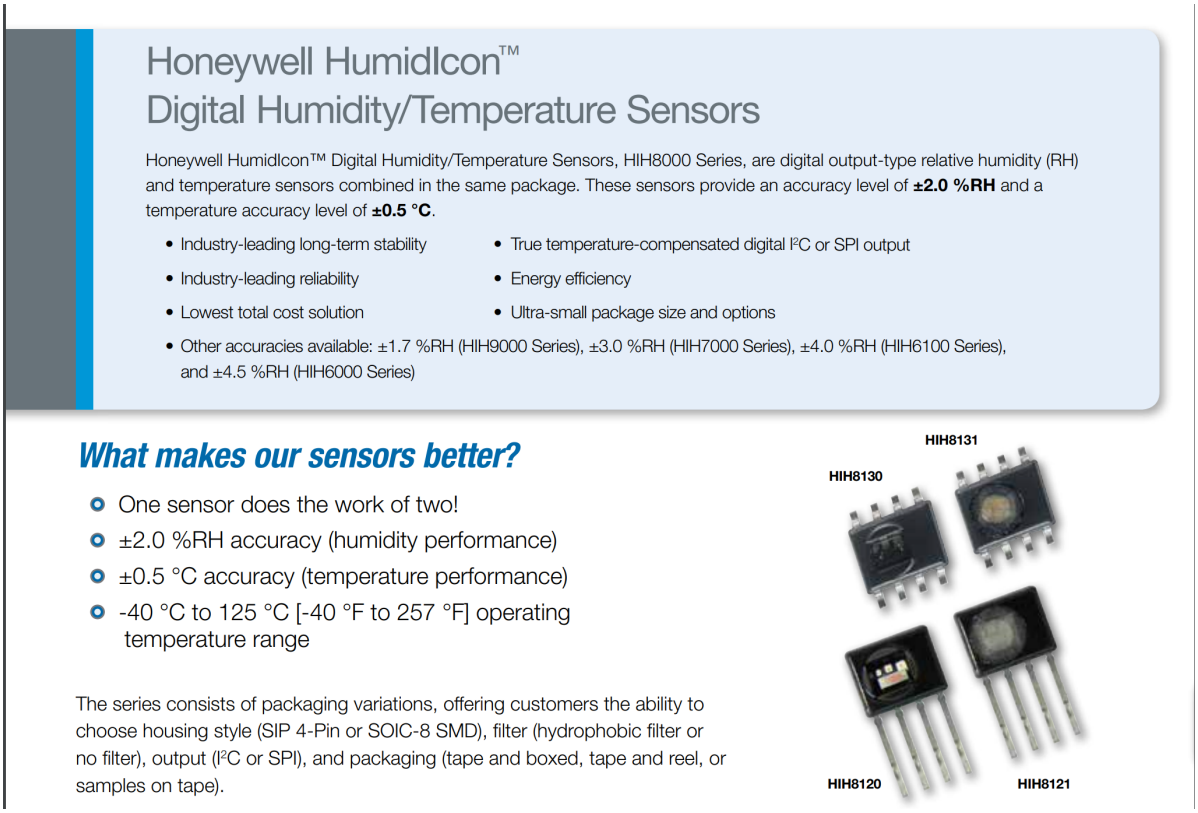

Honeywell HumidIcon™
Digital Humidity/Temperature Sensors

Honeywell HumidIcon™ Digital Humidity/Temperature Sensors, HIH8000 Series, are digital output-type relative humidity (RH) and temperature sensors combined in the same package. These sensors provide an accuracy level of **±2.0 %RH** and a temperature accuracy level of **±0.5 °C**.

- Industry-leading long-term stability
- Industry-leading reliability
- Lowest total cost solution
- True temperature-compensated digital I²C or SPI output
- Energy efficiency
- Ultra-small package size and options
- Other accuracies available: ±1.7 %RH (HIH9000 Series), ±3.0 %RH (HIH7000 Series), ±4.0 %RH (HIH6100 Series), and ±4.5 %RH (HIH6000 Series)

What makes our sensors better?

- One sensor does the work of two!
- ±2.0 %RH accuracy (humidity performance)
- ±0.5 °C accuracy (temperature performance)
- -40 °C to 125 °C [-40 °F to 257 °F] operating temperature range

The series consists of packaging variations, offering customers the ability to choose housing style (SIP 4-Pin or SOIC-8 SMD), filter (hydrophobic filter or no filter), output (I²C or SPI), and packaging (tape and boxed, tape and reel, or samples on tape).

Figure B.1: Data sheet of the RH Sensor used

where σ is the standard deviation and n is the number of samples. The error varies with the pressure values- in fact, it increases at higher pressures as seen in Figure 6.6. This is because of the increase in pressure drop after the maximum pressure is reached, without altering the valve-opening time. This results in a higher mass leakage at the pressure relief valve, for the higher pressure ranges.

B.2.3. Capillary Tube Mass Flows:

The mass flow after the capillary tube is measured using a syringe filled with water. The amount of displaced water within recorded time is taken as the volumetric flow rate of air at the outlet. It is converted to mass flow rate using:

$$\dot{m} = \frac{\delta V}{\delta t} \cdot \rho \cdot 3600 \tag{B.2}$$

Atmospheric pressure is assumed at the capillary tube outlet. The experiments were performed at 3 and 5 bars at each frequency step (2000-6000 rpm). The error in these measurements was calculated using:

$$\delta_m = \frac{\sigma}{\sqrt{n}} \tag{B.3}$$

where,

$$\sigma = \sqrt{\frac{1}{n-1}\sum_{i=1}^{n}\left(m_{\text{avg}} - m_i\right)^2} \tag{B.4}$$

C

Heater Model

At the beginning of this project, rod-heaters were used to heat up the drying columns. As they were placed at the core of the column, it would make the radial heat transfer effect significant. Therefore a simple steady-state model was made to see how the temperature distribution profile amongst the silica gel beads would look like. Figure C.2 discussed in Chapter 5 is a result of this steady state model. For the thermal circuit that is depicted in Figure C.1, the following assumptions were made:

- Steady 1-D heat flow (in radial plane)
- Silica gel is an insulation that is as long as the column.
- Homogeneous full length heat generation at the core.
- The heating element is very thin (Theat does not fade over the radius of the heater).
- There is no heat convection (from hot fluid through the pipe) while the column is being heated.
- Heat convection on the outside is only accounted for as Qloss.

The convection due to flow inside the drying column was ignored first, as the effect of the radial heating alone was intended to be measured. The conductivity of the silica gel beads used was also to be determined.

The model uses conservation of energy and a thermal analogy of the circuit depicted. It is given by

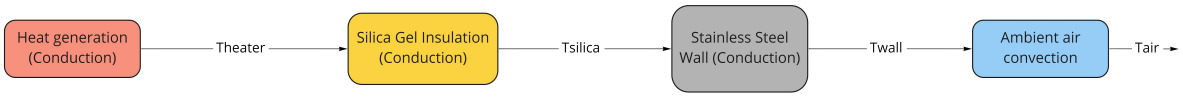

Figure C.1: Thermal circuit inside a drying column using rod heaters

the following set of equations:

$$\frac{dQ}{dt} = 0 = Q_{gen} - Q_{silica} - Q_{wall} - Q_{air} \tag{C.1}$$

where,

$$\begin{aligned} Q_{gen} &= Q_{silica} + \frac{T - T_{air}}{R_{total}} \\ Q_{silica} &= -k_s(2\pi r_s L) \\ R_{total} &= \ln\frac{r_{cyl}}{r_s} 2\pi k_{wall} + \frac{1}{2\pi r_{cyl} h_{air}} \end{aligned} \tag{C.2}$$

The ordinary differential equation to be solved, obtained from the aforementioned equations is:

$$\frac{dT}{dr} = aT - b$$
$$a = \frac{1}{2R_{total}k_s\pi r_s L}$$
$$B = \frac{-T_{air}}{R_{total}k_s\pi r_s L}$$
$$C = \frac{-Q_{heater}}{k_s\pi r_s L}$$
$$b = B + C$$

(C.3)

The solution of temperature profile is then given by Equation C.4 and shown in Figure C.2. From this

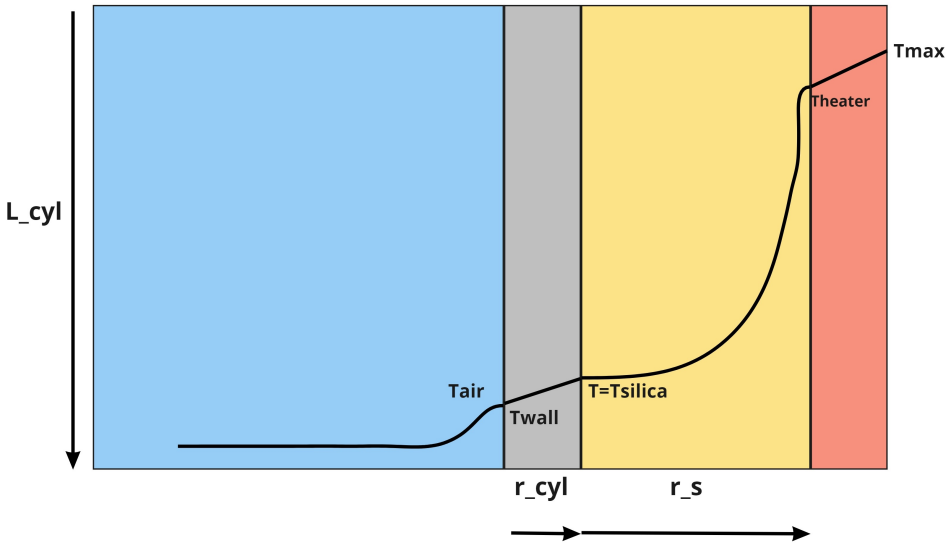

Figure C.2: Temperature profile in the radial direction using rod heaters

solution, an exponential decrease is expected in the radial profile, which was later substantiated by the experiments that showed very high warm-up times.

$$T(r) = C_1 e^{ar} + \frac{b}{a} \tag{C.4}$$

Bibliography

[1] Samir den Haan. Pre-processing of a co2 feedstream in a ccus methanol microplant. 2021. http://resolver.tudelft.nl/uuid:1d1dbf9f-8bef-4f66-aefe-71d9a70e4be9.

[2] G.F.Hundy. Refrigeration, air conditioning and heat pumps. page 60, 2016.

[3] Kuan Thai Aw, Alison Subiantoro, and Kim Tiow Ooi. Torque characteristics of the revolving vane air expander. *Machines*, 8(3), 2020. https://www.mdpi.com/2075-1702/8/3/58.

[4] T.Dwyer. Rolling-piston rotary refrigerant compressors for air conditioning applications. *CIBSE*, page module 163, 2020. https://www.cibsejournal.com/cpd/modules/2020-06-toshiba.

[5] Y. van Wijk. *Stageverslag blok 1*. De Haagse Hogeschool, February 2022. Internship Report.

[6] Illam Park and Kent S. Knaebel. Adsorption breakthrough behavior: Unusual effects and possible causes, 1992.

[7] B D Rasmussen and A Jakobsen. Review of Compressor Models and Performance Characterizing Variables. *International Compressor Engineering Conference*, 1429, 2000.

[8] Pieter Bergstein. Design of a carbon dioxide compression train. 2021. http://resolver.tudelft.nl/uuid:c3897c71-308c-4b4b-9beb-3c3cffb11d05.

[9] Abhijit Sathe, Eckhard Groll, and Suresh Garimella. Experimental Evaluation of a Miniature Rotary Compressor for Application in Electronics Cooling . *International Compressor Engineering Conference at Purdue*, (1929), 7 2008.

[10] Working Group Three to the Fifth Assessment Report of the Intergovernmental Panel on Climate Change. Ipcc: Summary for policymakers. 2014.

[11] Working Group One to the Sixth Assessment Report of the Intergovernmental Panel on Climate Change. Ipcc: Summary for policymakers. 2021.

[12] Carlos Marquez Charlie Hobson. Renewable methanol report. 2018. https://www.methanol.org/wp-content/uploads/2019/01/MethanolReport.pdf.

[13] Perttu Anttila and Antti Asikainen. The realistic potential for forest biomass supply in the european union. 2014. http://www.metla.fi/julkaisut/workingpapers/2014/mwp289.htm.

[14] Rocky C. Costello. Process intensification: Think small. *Pristine Processing*, pages 6–8, 4 2003. https://rccostello.com/publications_files/April2004chemeng.pdf.

[15] Joelle Aubin, J. Commenge, Falk Laurent, and Laurent Prat. *Process Intensification by Miniaturization*, pages 77–108. 06 2015.

[16] D A Collings, Z K Yap, and D K Haller. Compressor Mechanism Comparison For R744 Application.

[17] M. Ozu and T. Itami. Efficiency analysis of power consumption in small hermetic refrigerant rotary compressors. *International Journal of Refrigeration*, 4(5):265–270, 9 1981.

[18] Aspen LLC. Aspen vertical mini compressors. https://www.aspencompressor.com/vertical-mini-compressors.

[19] Hangzhou Purswave Technology. Bd15h dc refrigerator compressor. http://www.purswave.cn/en/pd.jsp?id=215.

[20] Saeid Mokhatab and William A. Poe. Chapter 11 - natural gas compression. In Saeid Mokhatab and William A. Poe, editors, *Handbook of Natural Gas Transmission and Processing (Second Edition)*, pages 393–423. Gulf Professional Publishing, Boston, second edition edition, 2012. https://www.sciencedirect.com/science/article/pii/B978012386914200011X.

[21] R.M.de Koning. *Research and Design of a CO2 Compressor for Implementation in a Methanol Micro-Plant*. TU Delft, 2020. MSc Thesis.

[22] Wakabayashi.H.; Yuuda.J.; Aizawa.T.; and Yamamura.M. Analysis of performance in a rotary compressor. *International Compressor Engineering Conference*, page 385. https://docs.lib.purdue.edu/icec/385, year = 1982,.

[23] Alberto R Gomes and Cesar J Deschamps. A THEORETICAL ASSESSMENT OF TWO TYPES OF POSITIVE DISPLACEMENT COMPRESSORS FOR HOUSEHOLD REFRIGERATION.

[24] R. Verhagen. *Double stage CO2 compression*. De Haagse Hogeschool, 2020. Internship Report.

[25] Diran Basmadjlan. Rapid Procedures for the Prediction of Fixed-Bed Adsorber Behavior. 1. Isothermal Sorption of Single Gases with Arbitrary Isotherms and Transport Modes: Principles and Recommended Methods. *Industrial and Engineering Chemistry Process Design and Development*, 19(1):129–137, 1 1980.

[26] Józef Nastaj and Bogdan Ambrożek. Modeling of drying of gases using solid desiccants. *Drying Technology*, 27(12):1344–1352, 2009. https://doi.org/10.1080/07373930903383679.

[27] John L. (John Lennox) Monteith and Mike Unsworth. Principles of environmental physics. page 440.

[28] S. Sircar and J. R. Hufton. Why Does the Linear Driving Force Model for Adsorption Kinetics Work? *Adsorption 2000 6:2*, 6(2):137–147, 6 2000.

[29] P.Colonna. *Modelling of Process and Energy Systems*. 2012.

[30] C Strumillo, P L Jones, and R Zylla. Energy Aspects in Drying in Handbook of Industrial Drying. In *Handbook of Industrial Drying*, pages 1101–1128. CRC Press, 4 2021.

[31] Engineering Toolbox. *Thermal Expansion of Metals*. 2005. https://www.engineeringtoolbox.com/thermal-expansion-metals-d_859.html.

[32] Majithia A, Hall S, and Harper L. Droplet breakup quantification and processes in constant and pulsed air flows . *Proceedings of the 22nd Conference on Liquid Atomisation and Spray Systems (ILASS-Europe)*, pages 8–10, 2008.

[33] Robert Brodkey. Formation of drops and bubbles. In *The phenomena of fluid motions*. Addison-Wesley, Reading Mass., 1967.

[34] Ludger O. Figura and Arthur A. Teixeira. Permeability. In *Food Physics*, pages 233–255. Springer, Berlin, Heidelberg, Berlin, Heidelberg, 2007.

[35] P C Carman. FLUID FLOW THROUGH GRANULAR BEDS. *Chemical Engineering Research and Design*, 75:S32–S48.

[36] I. F. Macdonald, M. S. El-Sayed, K. Mow, and F. A.L. Dullien. Flow through Porous Media—the Ergun Equation Revisited. *Industrial and Engineering Chemistry Fundamentals*, 18(3):199–208, 8 1979.

[37] C. W. Crawford and O. A. Plumb. The Influence of Surface Roughness on Resistance to Flow Through Packed Beds. *Journal of Fluids Engineering*, 108(3):343–347, 9 1986.

[38] James C. Knox, Armin D. Ebner, M. Douglas Levan, Robert F. Coker, and James A. Ritter. Limitations of Breakthrough Curve Analysis in Fixed-Bed Adsorption. *Industrial and Engineering Chemistry Research*, 55(16):4734–4748, 4 2016.

[39] N. Wakao and T. Funazkri. Effect of fluid dispersion coefficients on particle-to-fluid mass transfer coefficients in packed beds. Correlation of sherwood numbers. *Chemical Engineering Science*, 33(10):1375–1384, 1978.

[40] M. F. Edwards and J. F. Richardson. Gas dispersion in packed beds. *Chemical Engineering Science*, 23(2):109–123, 5 1968.

[41] Herausgegeben Von Der Gesellschaft, Deutscher Chemiker, and E Wicke. Strukturbildung und molekulare Beweglichkeit im Wasser und in wäßrigen Lösungen. *Angewandte Chemie*, 78(1):1–19, 1 1966.

[42] Douglas M. Ruthven. *Dynamics of adsorption columns: Single-transition systems*. Wiley-Interscience, 1984.

[43] Chin-Yung Wen and L. T. (Liang-tseng) Fan. *Models for flow systems and chemical reactors*. Marcel Dekker, New York, 1975.

[44] Bogdan Ambrozek. The Simulation of Cyclic Thermal Swing Adsorption (TSA) Process. *Studies in Computational Intelligence*, 180:165–178, 2009.

[45] Plumb O.A. Transport Phenomena in Porous Media: Modeling the Drying Process. In Kambiz Vafai, editor, *Handbook of POROUS MEDIA, Second Edition*. 2005.

[46] Chi Hsiung Li and B. A. Finlayson. Heat transfer in packed beds—a reevaluation. *Chemical Engineering Science*, 32(9):1055–1066, 1 1977.

[47] Mohsen Mansouri, Hamid Reza Azizi, and Naimeh Setareshenas. Modeling of Fixed-Bed Rapid Temperature Swing Adsorber for Butanol Dehydration. *Chemical Engineering and Technology*, 44(6):1141–1147, 6 2021.

[48] J. K. Gigler, W. K.P. Van Loon, M. M. Vissers, and G. P.A. Bot. Forced convective drying of willow chips. *Biomass and Bioenergy*, 19(4):259–270, 10 2000.

[49] Czesław Strumiłło and Tadeusz Kudra. *Drying : principles, applications, and design*. Gordon and Breach Science Publishers, New York, 1986.

[50] J. P. Holman. *Heat transfer*, volume 9 MB. McGraw Hill Higher Education„ Boston [Mass.] :, 2010.

[51] Suzuki M. *Adsorption engineering*. Elsevier, Tokyo; Amsterdam; New York, 1990.

[52] Joan M. Schork and James R. Fair. Parametric analysis of thermal regeneration of adsorption beds. *Industrial and Engineering Chemistry Research*, 27(3):457–469, 3 1988.

[53] Henrik Bjurström, Ernest Karawacki, and Bo Carlsson. Thermal conductivity of a microporous particulate medium: moist silica gel. *International Journal of Heat and Mass Transfer*, 27(11):2025–2036, 11 1984.

[54] José Maurício Gurgel and Rogerio P. Klüppel. Thermal conductivity of hydrated silica-gel. *The Chemical Engineering Journal and the Biochemical Engineering Journal*, 61(2):133–138, 2 1996.

[55] Qili Hu and Zhenya Zhang. Application of Dubinin–Radushkevich isotherm model at the solid/solution interface: A theoretical analysis. *Journal of Molecular Liquids*, 277:646–648, 3 2019.

[56] E. Van Den Bulck. Isotherm correlation for water vapor on regular-density silica gel. *Chemical Engineering Science*, 45(5):1425–1429, 1 1990.

[57] M. M. DUBININ and V. A. ASTAKHOV. Description of Adsorption Equilibria of Vapors on Zeolites over Wide Ranges of Temperature and Pressure. pages 69–85, 6 1971.

[58] Marie-Georges Olivier and Roger Jadot. Experimental Selectivity Curves of Gaseous Binary Mixtures of Hydrocarbons and Carbon Dioxide on Activated Carbon and Silica Gel. Technical report, 1998.

[59] Carlos A. Grande, Daniela G.B. Morence, Aud M. Bouzga, and Kari Anne Andreassen. Silica Gel as a Selective Adsorbent for Biogas Drying and Upgrading. *Industrial and Engineering Chemistry Research*, 59(21):10142–10149, 5 2020.

[60] David S. Hage. Chromatography. *Principles and Applications of Clinical Mass Spectrometry: Small Molecules, Peptides, and Pathogens*, pages 1–32, 1 2018.

[61] John Fuchs. The Effect of Temperature on Relative Humidity, 5 2013.

[62] Maxwell James Clerk. A treatise on electricity and magnetism. *A Treatise on Electricity and Magnetism*, 9781108014038:1–442, 1 2010.

[63] T. H. Bauer. A general analytical approach toward the thermal conductivity of porous media. *International Journal of Heat and Mass Transfer*, 36(17):4181–4191, 11 1993.

[64] P. Zehner and E. U. Schlünder. Wärmeleitfähigkeit von Schüttungen bei mäßigen Temperaturen. *Chemie Ingenieur Technik*, 42(14):933–941, 7 1970.

[65] O. Krischer. *Die wissenschaftlichen Grundlagen der Trocknungstechnik*. Springer Berlin Heidelberg, Berlin, 1 edition, 1956.

[66] Schwarzacher Walther. Deterministic models. In Schwarzacher Walther, editor, *Developments in Sedimentology*, volume 19, chapter 3, pages 37–59. Elsevier, 1 1975.

[67] Ajit K. Thakur. Model: Mechanistic vs Empirical. *New Trends in Pharmacokinetics*, pages 41–51, 1991.

[68] Garr M. Jones. *Pumping station design*. Butterworth-Heinemann, 3rd edition, 2006.

[69] Glenn O. Brown. The History of the Darcy-Weisbach Equation for Pipe Flow Resistance. *Proceedings of the Environmental and Water Resources History*, pages 34–43, 2002.

[70] Robert T. Balmer. Vapor and Gas Refrigeration Cycles. *Modern Engineering Thermodynamics*, pages 535–590, 1 2011.

[71] P.S.M. Vroegindewij. Modelling, experimental validation and characterization of a novel small scale methanol synthesis reactor. 2021.

[72] AHRI. *STANDARD FOR PERFORMANCE RATING OF POSITIVE DISPLACEMENT CONDENSING UNITS*. ANSI Approved American National Standard, Arlington, 2004.

[73] Howard Cheung and Shengwei Wang. A comparison of the effect of empirical and physical modeling approaches to extrapolation capability of compressor models by uncertainty analysis: A case study with common semi-empirical compressor mass flow rate models. *International Journal of Refrigeration*, 86:331–343, 2 2018.

[74] RE Walpole, RH Myers, SL Myers, and K Ye. *Probability and statistics for engineers and scientists*. Pearson, Boston, 9th edition, 1993.

[75] J Steven Brown, Samuel F Yana-Motta, and Piotr A Domanski. Comparitive analysis of an automotive air conditioning systems operating with CO 2 and R134a. *International Journal of Refrigeration*, 25:19–32, 1 2001.

[76] Matthias Neubronner, Thomas Bodmer, Christof Hübner, Paul Bernd Kempa, Evangelos Tsotsas, Axel Eschner, Günther Kasparek, Fabian Ochs, Hans Müller-Steinhagen, Hans Werner, and Martin H. Spitzner. Properties of Solids and Solid Materials. In *VDI Heat Atlas*, pages 551–614. Springer Berlin Heidelberg, 2010.

[77] Evangelos Tsotsas. Heat and Mass Transfer in Packed Beds with Fluid Flow. In *VDI Heat Atlas*. Springer Berlin Heidelberg, 2010.